UNIVERSITY OF OKLAHOMA

GRADUATE COLLEGE

EXPERIMENTAL AND THEORETICAL STUDY OF A NOVEL FREEZE DESALINATION METHOD USING AN INTERMEDIATE COOLING LIQUID

A DISSERTATION

SUBMITTED TO THE GRADUATE FACULTY

in partial fulfillment of the requirements for the

Degree Of

DOCTOR OF PHILOSOPHY

By

REZA KAVIANI

Norman, Oklahoma

2024

EXPERIMENTAL AND THEORETICAL STUDY OF A NOVEL FREEZE DESALINATION METHOD USING AN INTERMEDIATE COOLING LIQUID

A DISSERTATION APPROVED FOR THE

SCHOOL OF AEROSPACE AND MECHANICAL ENGINEERING

BY THE COMMITTEE CONSISTING OF

Dr. Hamidreza Shabgard, Chair

Dr. Ramkumar Parthasarathy

Dr. Jie Cai

Dr. Pejman Kazempoor

Dr. Dimitrios V. Papavassiliou

Acknowledgments

First and foremost, I extend my deepest gratitude to my academic supervisor, Prof. Hamidreza Shabgard, for his invaluable guidance, insightful advice, and unwavering support throughout my Ph.D. journey. His expertise and mentorship have been crucial in shaping my academic development and research skills, significantly enriching my doctoral experience. I would like to express my gratitude to Prof. Ramkumar Parthasarathy, Prof. Jie Cai, Prof. Pejman Kazempoor, and Prof. Dimitrios V. Papavassiliou for their invaluable contributions to my dissertation as members of my Ph.D. committee. Their expertise and insights have been instrumental in shaping and refining my research. I am immensely grateful to the staff members of the School of Aerospace and Mechanical Engineering for their consistent kindness, support, and assistance. A special thanks goes to Mr. Billy Mays and Mr. Greg Williams, as well as to the students working in the machine shop. Their invaluable help and contributions were crucial in this research.

I am deeply appreciative of the generous financial support provided by the University of Oklahoma's School of Aerospace and Mechanical Engineering, alongside several scholarships. These include the Conoco Phillips Scholarship, the Jim and Bee Close Scholarship, and the Tomorrow's Engineering scholarship, offered by the Gallogly College of Engineering. Their continued and gracious contributions have been instrumental in supporting my academic pursuits and research endeavors. Last but not least, I extend my deepest gratitude to my family for their support throughout my Ph.D. journey. My heartfelt thanks go to my mother, Mrs. Sima Yaghoobi, my father, Mr. Naser Kaviani, and my sister, Miss. Sepideh Kaviani, for their perpetual encouragement and blessings. Their constant support has been a cornerstone of my strength and perseverance during this challenging and rewarding academic endeavor.

Table of Contents

List of Tables

List of Figures

Abstract

Freeze desalination (FD) emerges as a promising method for treatment of high-salinity brines. In this work, experimental and theoretical studies are conducted on the design, fabrication, and testing of a novel FD system for desalinating brines with salinities up to 100,000 ppm. The system integrates a refrigeration unit with a desalination unit via an intermediate cooling liquid (ICL). The desalination unit is comprised of a freezing chamber, a slurry transport section, and separation modules. Operating at atmospheric pressure, the FD system leverages the efficient heat transfer achieved through direct contact between the brine and the ICL, thus avoiding complications like ice adhesion to cooling surfaces and the mixing of refrigerant with the treated water. A key factor in increasing the energy efficiency of the developed method is recovering the cold energy of the generated ice to cool the condenser of the refrigeration unit. This can be achieved by running an ice-water slurry through a heat exchanger to absorb heat from the condensing refrigerant. To better understand the fundamentals of ice-water slurry heat transfer, a computational model is developed to simulate the melting of a suspended solid particle in its own melt. The fabricated prototype is used to study the impacts of various operational parameters such as feed brine salinity, cooling temperatures, and centrifugation times on the recovery ratio and the purity of the treated water. It is found that lower cooling temperatures and feed brine salinities enhance the recovery ratio, while increasing the salinity of the treated water. Specifically, a feed brine with a TDS of 70,000 ppm and a cooling temperature of -17°C resulted in a recovery ratio of approximately 50% and a treated water TDS of about 2,600 ppm. This study demonstrates a novel method for desalinating high-salinity brines, which potentially offers greater energy efficiency compared to conventional evaporative methods. This method could have significant applications in industrial brine management and brine mining.

1. Introduction

This chapter aims to provide a comprehensive understanding of the necessity, and current challenges and opportunities in water treatment, establishing the foundation for a detailed exploration of freeze desalination as an effective approach to address a specific subset of these issues. The chapter begins with an overview of the water scarcity problem and the growing demand for innovative water treatment solutions. Next, desalination is introduced as a potential solution for addressing the increasing freshwater demand and a brief review of the most widely used desalination technologies is presented. Afterwards, brine management strategies, which are crucial for the treatment of high salinity water resources, are discussed. Lastly, a description of freeze desalination, the focus of this study, is provided, presenting it as a promising technique for managing high salinity brine.

1.1. Background

Water is an essential natural resource, crucial for the survival of all living organisms [1]. Often perceived as a basic and freely accessible right, water is abundant, covering about 71% of the Earth's surface. Despite its prevalence, 97% of the Earth's water is saline, leaving only 3% as fresh water, which is suitable for human, plant, and animal consumption [2]. Out of this small portion, nearly 2.5% is trapped in polar ice caps, glaciers, and the atmosphere, making it largely inaccessible, making just about 0.5% available for human use in rivers and groundwater. Freshwater, found both on the Earth’s surface and underground, has low salinity and is considered renewable due to the natural water cycle. Surface freshwater, which is found in rivers and lakes, is low in salinity and thus potable [3]. In contrast, fresh groundwater, which exists beneath the Earth's surface, has a higher salinity than surface freshwater [4]. Saline water, found in oceans, seas, and

saltwater lakes, dominates the Earth's water resources, making up most of the total water volume. This vast majority highlights the scarcity and critical importance of managing our limited freshwater resources effectively.

Escalating water demands driven by population growth, rising living standards, increased per capita water usage, and economic expansion are intensifying global water scarcity. These demands are further intensified by diminishing water supplies due to climate change and contamination [5,6]. Consequently, water sources are depleting more rapidly than their natural replenishment rate. Numerous communities worldwide are struggling with challenges such as increased demand, persistent droughts, resource depletion, and the degradation of both surface and groundwater sources. These communities are frequently reliant on a solitary water supply source, underscoring the vulnerability of their water systems [7]. Recent estimates indicate that 40% of the global population currently experiences severe water scarcity, a figure projected to increase to 60% by 2025 [8]. Approximately 30% of the global population lacks access to clean water sources necessary for basic sanitation needs [9], and 66% of the global population currently experiences severe water scarcity for at least one month each year [10]. These alarming trends highlight the insufficiency of "conventional" water sources—rainfall, snowmelt, and river runoff stored in lakes, rivers, and aquifers—to meet the demands in water-scarce regions.

Addressing water scarcity requires a fundamental reassessment of water resource planning and management. This includes harnessing a diverse array of viable, while unconventional, water resources for various uses such as supporting livelihoods, ecosystems, climate change adaptation, and sustainable development [11]. Although water demand mitigation strategies like water conservation and efficiency improvements can help narrow the gap between water demand and supply, they need to be integrated with supply enhancement strategies to effectively tackle water

scarcity [7]. Practices for conserving water resources and enhancing supply are already in place in some water-scarce areas, but there is a pressing need for wider implementation, especially in regions where water scarcity and quality deterioration are escalating [12,13]. Due to the scarcity of freshwater resources and the pressing need for enhanced water supply, desalination— the process of treating saline water to obtain freshwater—has emerged as a viable solution for many countries with limited or no access to natural freshwater supplies. This technology taps into the abundant supplies of saline water, including seawater and brackish water, offering a crucial alternative for regions struggling with water scarcity.

1.2. Desalination

Desalination is a process of extracting freshwater from saline sources such as seawater or brackish water, producing water that meets the quality standards required for various human activities [14]. Developed as an alternative to conventional water sources, desalination leverages the vast availability of saline water to address the critical issue of freshwater scarcity [15]. Over time, desalination has proven to be a dependable method for securing water supplies, with significant advancements in both technical and economic viability [1]. As of 2018, the global annual desalination capacity reached 38 billion cubic meters per year (BCM/yr), or 95 million cubic meters per day (MCM/d), nearly doubling from 44.1 MCM/d in 2006 [16,17]. Forecasts predict this capacity will increase by another 42%, reaching 54 BCM/yr by 2030 [18].

The process of converting brackish water or seawater into fresh drinking water through heating is the oldest desalination technique, primarily due to the historically low cost of fossil fuels [19]. This method mimics the natural hydrological cycle, which naturally purifies seawater and brackish water. The desalination process can be categorized based on feedwater type, separation

technique, or the energy source driving the process. Types of feedwaters include seawater, brackish water, river water, and wastewater. Separation techniques comprise thermal desalination, membrane desalination, crystallization, and other emerging methods. Energy sources utilized in these processes are primarily thermal, mechanical, or electrical. Thermal desalination involves converting seawater from liquid to vapor phase through boiling, then condensing the vapors back to liquid form to produce potable water. Membrane desalination employs chemical, electrical, or mechanical energy to filter salts from seawater through semi-permeable membranes, separating the potable water. Crystallization separates pure water from saline solutions through a freeze-melt process [19].

In terms of global capacity and distribution, seawater desalination dominates, comprising about 61% of desalination capacity and representing 37% of the total number of desalination plants. Brackish water desalination accounts for 21% of capacity and 41% of the total plant count, with the remainder attributed to river water and wastewater desalination [17]. Membrane desalination leads in technology usage, constituting approximately 69% of global desalination capacity and about 85% of all desalination plants. Thermal desalination, while less prevalent, contributes about 25% of the global capacity and 8% of the plant count [17].

Before exploring the various desalination methods, it is essential to clearly define the different types of saline water. Water sources can be classified based on their total dissolved solids (TDS), as shown in Table 1-1 [20]. Salinity refers to the total salt concentration, quantified as the amount of dry solids per kilogram or liter of seawater, and can also be expressed as parts per million (ppm). The chemical makeup of ocean and sea water varies by location, affecting both the composition and temperature of different seawater samples. Sodium and chloride are the most prevalent ions, but seawater also contains other dissolved salts beyond sodium chloride. In the

desalination process, saline water, whether seawater or brackish water, is divided into two separate streams. The desalinated stream yields the desired product, freshwater, which meets specific salinity requirements. The other stream, known as the "brine" stream, is highly concentrated and must be properly disposed of as waste or treated using appropriate methods to mitigate environmental impact.

Table 1-1 Categorization of water sources based on dissolved solids content

Water classification	Total dissolved solids (TDS)
High-quality drinkable water	<200 ppm
Drinkable water	200 - 500 ppm
Freshwater	500 - 1,000 ppm
Mildly brackish water	1,000 - 5,000 ppm
Moderately brackish water	5,000 - 15,000 ppm
Heavily brackish water	15,000 - 32,000 ppm
Low salinity seawater	32,000 - 37,000 ppm
High salinity seawater	>37,000 ppm

The applicability of various desalination methods for different ranges of input feed brine TDS and their specific energy consumption are illustrated in Fig. 1-1. The membrane-based methods shown include reverse osmosis (RO), forward osmosis (FO), and electrodialysis (ED). The thermal-based desalination technologies presented are multi-effect desalination (MED), freeze desalination (FD), and brine concentrator (BC). The following sections will discuss the most widely used desalination technologies for both membrane-based and thermal-based methods.

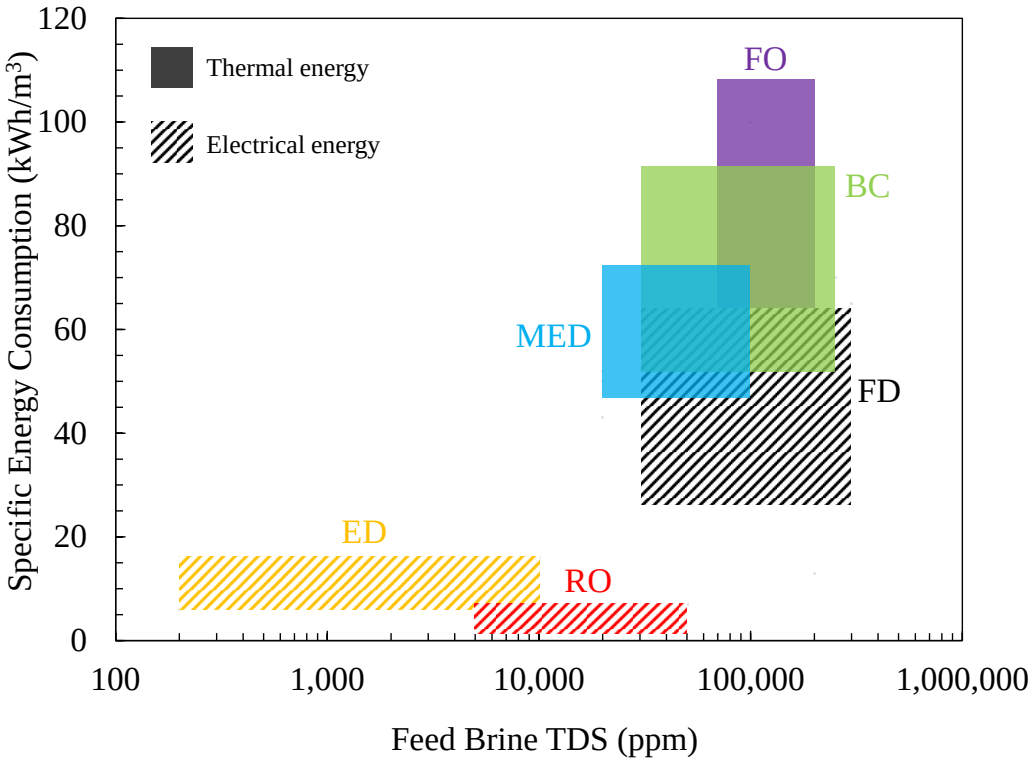

Fig. 1-1 Comparison of the specific energy consumption across various desalination technologies within their respective feed brine TDS ranges

1.2.1. Membrane Desalination

Membrane processes for desalination evolved during the 1960s and 1970s, driven by rising energy costs and stricter environmental regulations [21]. These technologies have become more popular than thermal methods because they are more energy-efficient and compact. Membrane-based desalination processes typically use mechanical pressure, electrical potential, or a concentration gradient as the driving force across a semi-permeable membrane to achieve physical separation. Some of the pressure-driven membrane desalination processes are Microfiltration (MF), Ultrafiltration (UF), Nanofiltration (NF), and Reverse Osmosis (RO) [22]. Microfiltration and ultrafiltration processes require low-pressure membranes to accomplish the filtration, whereas

nanofiltration and reverse osmosis processes necessitate high-pressure membranes. Reverse osmosis is the most prominent membrane process, followed by nanofiltration. Figure 1-2 depicts the comparison between different pressure-driven membrane-based desalination processes.

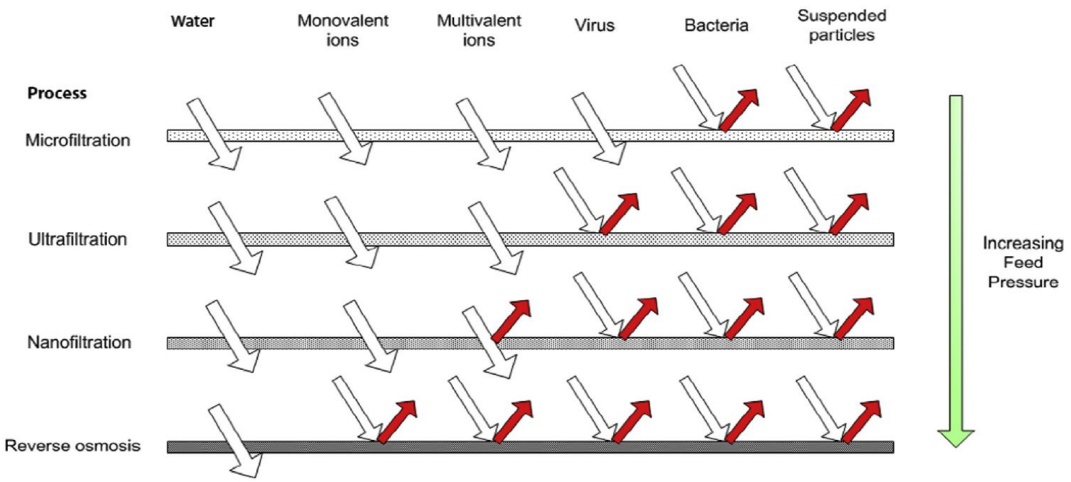

Fig. 1-2 Different pressure-driven membrane processes [22]

Electrodialysis (ED) process is a membrane-based desalination method in which ions migrate under the influence of an applied electric field, allowing for the removal of salt ions through ion-permeable membranes. Positive ions (cations) travel in one direction, while negative ions (anions) travel in the opposite direction. The cation-permeable membrane selectively permits the passage of cations, whereas the anion-permeable membrane facilitates the movement of anions out of the solution [23]. The Forward osmosis (FO) desalination process leverages the natural osmotic pressure gradient across a membrane to facilitate the movement of water molecules, unlike Reverse osmosis (RO) which requires external pressure to counteract the feed's osmotic pressure. In the FO process, a highly concentrated salt solution is used. This solution has a low water chemical potential (high osmotic pressure) and serves to attract water molecules from a feed solution (such as brackish water or seawater) that has a higher water chemical potential (lower

osmotic pressure) relative to the draw solution. In the subsequent sections, two of the most widely used membrane-based desalination methods, namely RO and FO, are described in further detail.

Reverse Osmosis (RO)

Reverse osmosis (RO) desalination was first applied to brackish groundwater in the late 1960s and later to seawater desalination by the 1980s [24]. Osmosis is the natural flow of a solvent (e.g., water) through a semipermeable membrane from a solution with a low concentration of solutes (e.g., salts) to a more concentrated solution. The driving force for this solvent transport is known as osmotic pressure, which depends on the difference in solute concentrations between the two solutions. This transport process continues until osmotic equilibrium is reached between the solutions [25]. Conversely, RO is a pressure-driven membrane separation process in which a membrane allows the diffusion of the solvent and solutes. When pressure higher than the osmotic pressure is applied to the concentrated solution, the flow of the solvent through the membrane is reversed. The solvent then flows from the concentrated solution side through the membrane to the diluted solution side, while the solutes are rejected by the membrane [21]. The osmosis process is presented in Fig. 1-3.

RO membranes are typically composed of two distinct layers. The active or selective layer is made of polymeric materials thin-film composite of polyamide, which are responsible for the semi-permeability characteristics [26]. The second layer is a thick support layer that provides mechanical strength to withstand high hydraulic pressures, which can reach up to 70 bars [21,27]. The driving force for the RO process is the hydraulic pressure applied to overcome osmotic pressure. This pressure varies considerably according to the feedwater salinity, ranging from 15–25 bar for brackish water desalination to 60–70 bar for seawater desalination [28]. Energy

requirements differ depending on the feedwater source, with higher energy requirements for seawater RO and lower for brackish water RO, due to the lower pressures involved. Pretreatment, including filtration and chemical addition, is a necessary step in RO systems to prevent biofouling of the membranes [28,29].

Large-scale RO desalination units currently operate with a water flux of up to 400,000 m^3/day [30]. As with other membrane-based filtration methods, the most critical challenge for RO is membrane fouling [27]. Fouling occurs when insoluble rejected matter accumulates on the membrane surface, leading to a decline in permeation production [31]. This issue obstructs long-term performance and escalates operational and maintenance costs.

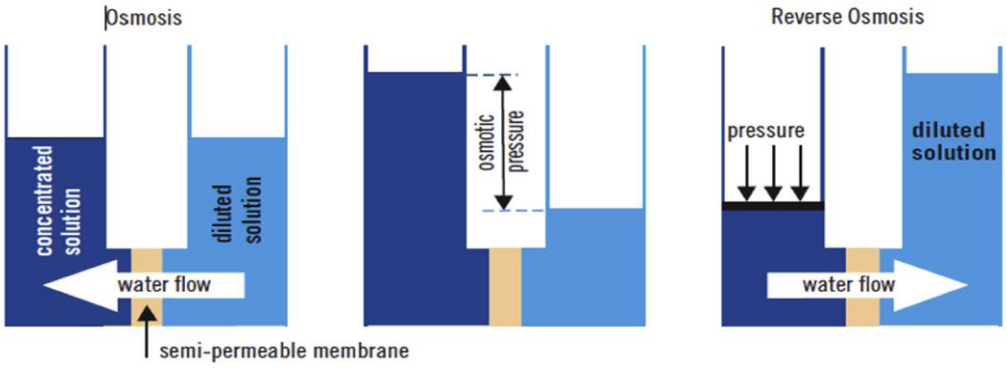

Fig. 1-3 Osmosis process representation [32].

Forward Osmosis (FO)

Forward osmosis (FO) stands out as a membrane-based technology that employs osmotic pressure differentials rather than hydraulic pressure [33]. In this process, a highly concentrated solution, known as the 'draw solution' is employed to create an osmotic pressure gradient across a semi-permeable membrane. This gradient prompts the movement of water molecules from a less concentrated feed brine solution towards the more concentrated draw solution, thereby effecting

the separation of freshwater from the draw solution [34–36]. FO exhibits greater energy efficiency compared to RO, as it operates without the need for external pressure. However, recent studies conducted at commercially viable flow rates have identified fouling as a significant challenge in FO systems [37]. The draw solution plays a crucial role in establishing osmotic pressure gradients, thereby impacting the performance of FO technology [38]. An ideal draw solution should be cost-effective, readily available, promote high water flux, exhibit low fouling potential and reverse solute diffusion, possess minimal toxicity to microorganisms, and facilitate easy recovery [39]. Presently, only a limited number of FO units suitable for high TDS brine are commercially accessible. A schematic representation of the FO system is shown in Fig. 1-4.

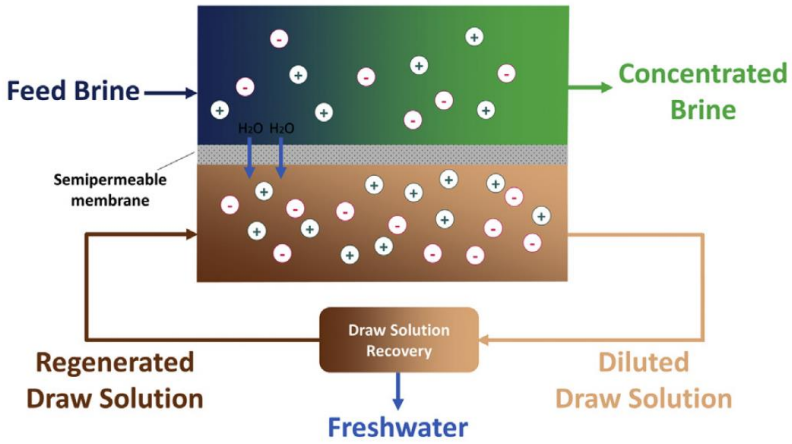

Fig. 1-4 A schematic diagram of FO [40].

1.2.2. Thermal Desalination

Thermal desalination, mirroring the natural hydrological cycle, is a prevalent method used to produce fresh water. In the natural hydrological cycle, sunlight heats water on Earth's surface, causing it to evaporate into the atmosphere. The vapor then rises, condenses into clouds, and eventually precipitates as rain when it encounters cold air. Similarly, thermal desalination employs

the principles of evaporation and condensation. In this process, an energy source heats saline feed water in an evaporator. As the water evaporates, the resulting vapors, driven by density differences, rise towards a condenser where they cool and condense back into liquid form. The distilled water, now with significantly reduced salt concentrations collected as potable water. The thermal desalination process is capable of producing water with extremely low salt concentrations, achieving TDS levels of 10 ppm or less from sources with very high salt concentrations, ranging from 60,000 to 70,000 ppm TDS [41]. Thermal desalination processes have long dominated the world's desalination capacity, until recent advancements in membrane desalination technologies began to shift the landscape [21]. However, despite its effectiveness in producing high-quality water, the considerable energy consumption associated with thermal desalination results in high operating costs. This factor makes it less economically attractive compared to membrane desalination methods, which are generally more energy-efficient.

The primary methods in thermal desalination include multistage flash desalination (MSF), multiple effect distillation (MED), single effect evaporation (SEE), humidification-dehumidification (HDH), and solar stills (SS) [42]. Among these, MSF and MED are the mainstays in commercial applications, holding market shares of approximately 87% and 12% respectively in commercial desalination plants. Conversely, other thermal desalination methods like SS and HDH are not commercially utilized, remaining largely within the realms of experimental prototypes or conceptual designs [43]. In the sections that follow, MSF and MED technologies are introduced and their processes are described in detail due to their predominant roles in commercial desalination.

Multi-Effect Desalination (MED)

The MED process was the first thermal method implemented for seawater desalination intended for consumption. The MED process produces freshwater by condensing vapor from boiling saline water through a series of stages, or effects, each maintained at progressively lower temperatures than the previous one [44]. A heat source, usually coming from a boiler, is used to increase the temperature of the input water up to 110°C for the first effect. In the first effect, steam is generated and transferred through a tube to subsequent effects, where it continues to boil the saline water [30]. The amount of vapor produced in each effect is slightly lower than in the previous one due to the increase in latent heat of vaporization as the evaporation temperature decreases. The heat of condensation from each effect supplies the heat needed for the next effect to vaporize part of the brine. Consequently, the only external heat source required is to heat the feed saline water for the first effect. As the primary steam does not come into direct contact with the saline water, the condensate inside the evaporator is typically recycled to the boiler for reuse [45]. A schematic of the MED desalination process is shown in Fig. 1-5.

Industrial MED systems can include up to 12 evaporation effects, resulting in water production capacities ranging from 600 to 30,000 m^3/day. Among thermal desalination processes, the MED thermal process is particularly promising due to its low electrical energy consumption, low operating costs, and high thermal efficiency [46,47]. To further enhance energy efficiency, MED systems can be coupled with either thermal or mechanical vapor compression units [48]. Hybrid configurations, which integrate other thermal or membrane technologies, are increasingly seen as more efficient and effective than traditional thermal desalination methods.

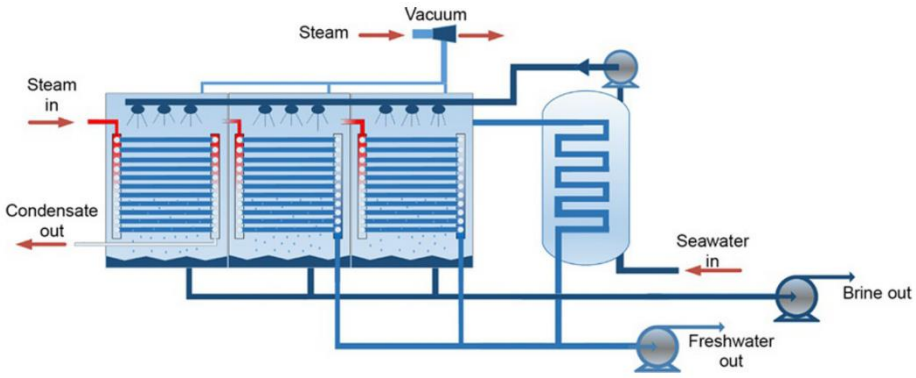

Fig. 1-5 Schematic of the MED desalination [30].

Multi-Stage Flash Desalination (MSF)

The MSF process shares some similarities with the previously described MED process. Both require an initial heat supply, often utilizing steam from a power plant, and rely on decreasing pressure to promote vapor production [49]. The basic principle of MSF desalination is flash evaporation. In the MSF process, saline water input is pressurized and heated to the maximum allowable temperature. When this heated liquid is discharged into a chamber held slightly below the saturation vapor pressure of water, a portion of its water content converts to steam. This flash vapor is then separated from suspended brine droplets as it passes through a mist eliminator and condenses on the outer surface of heat transfer pipes. The condensed liquid drips into trays, producing hot freshwater [50]. To maximize output and maintain economic efficiency, regenerative heating is typically performed. Therefore, this process involves distinct stages, with the temperature of incoming saline water gradually increasing at each stage. Modern MSF plants use multi-stage evaporators with 19 to 28 stages [51], enabling production volumes of 10,000 to 40,000 m^3/day [48]. The advantages of the MSF system for desalination include its reliability for large-scale desalinated water production, tolerance to varying saline water quality, and the high

quality of the desalinated water. However, this technology also has disadvantages, such as high energy consumption and the considerable expense of the plant [52]. [45]. A schematic of the MSF desalination process is shown in Fig. 1-6.

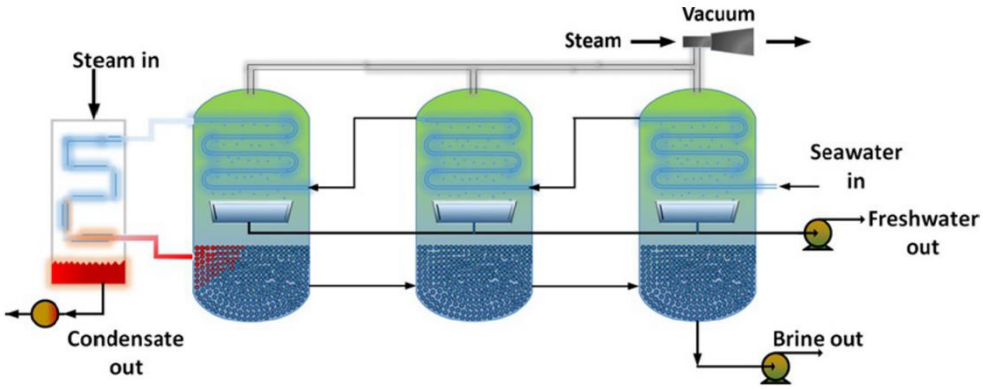

Fig. 1-6 Schematic of the MSF desalination [30]

1.3. Brine Management

In desalination, feedwater is separated into two streams: the product stream (freshwater) and the by-product stream (brine). Although desalination produces freshwater, a critical environmental issue is the coproduction of brine. Brine also originates from other industries, including oil and gas production, textiles, and dairy [53]. Currently, global brine production is approximately 141.5 million m^3/day, or 51.7 billion m^3/year [17]. This brine contains high concentrations of dissolved salts (up to 400,000 mg/L), along with minor amounts of organic matter, metals, nutrients, and pathogenic substances [54,55]. The characteristics of brine depend on the quality of the feedwater, the industry, recovery rate, purity of the produced freshwater, pre-treatment units, and chemical additives used [40]. Brine is commonly disposed of through various methods, such as surface water discharge, sewer discharge, deep-well injection, evaporation ponds, and land application [56].

Despite the widespread use of traditional disposal methods, concerns about the long-term impact on the environment and human health necessitate a different approach to brine management [40]. Potential adverse effects of rejected brine on the environment include pollution, pH fluctuations, and the accumulation of heavy metals in receiving ecosystems [57,58]. To select a suitable and sustainable brine management method, several factors must be considered. These include the volume of rejected brine, the chemical characteristics of the concentrate, geographical location, availability of disposal sites, feasibility of treatment technology in terms of legal and public acceptance, capital and operational costs, and the facility's capacity for storage and transportation of brine to treatment locations [57]. Approaches to eliminate the demand for brine disposal and allow for the recovery of both freshwater and salt are membrane-based and thermal-based brine treatment technologies. However, these technologies currently have very high capital and operating costs, limiting their adoption [59]. Some of the thermal processes are MSF, MED, and brine concentrators, which have been utilized in full-scale plants for many years [60]. However, these thermal processes are often not cost-efficient due to their high capital investment and significant energy requirements. To reduce the costs, membrane-based processes such as RO and FO can be used to further concentrate the brine before thermal treatment. Additionally, various pre-treatment methods can be applied before the membrane processes to address the primary challenge of membrane fouling [61].

Many desalination technologies, including MSF, MED, RO, and FO, are viable for treating high-salinity brine, but each has its own set of challenges that need addressing. Thermal-based methods such as MED and MSF are effective at handling high-salinity brine; however, they require extensive pretreatment to prevent fouling and scaling. Additionally, their capital costs can be significant due to the need for corrosion-resistant materials. Membrane-based methods such as RO

offer a more cost-effective solution for producing fresh water, but they face limitations with brine salinity levels exceeding 70,000 ppm, beyond which energy consumption increases significantly and water recovery rates drop [40]. FO represents an innovative approach within membrane-based methods, capable of treating high-salinity brine at relatively low costs. Another promising and emerging method is freeze desalination (FD), which offers potential advantages for high-salinity brine treatment. The subsequent sections will explore conventional brine disposal methods and introduce freeze desalination as an emerging technique in the field.

1.3.1. Disposal Methods

The desalination industry has developed various methods for brine disposal, including surface water discharge, sewer discharge, deep-well injection, evaporation ponds, and land application. Brine disposal expenses can range from 5% to 33% of the total process costs, influenced by the characteristics and volume of the brine, the level of pretreatment required, the means of disposal, and the nature of the disposal environment [62]. In the following, three of the most employed brine disposal approaches are described.

Surface Water Discharge

Surface water discharge, a prevalent brine disposal method, involves directly releasing brine into oceans, rivers, bays, lakes, and other open water bodies. The process entails transferring the brine to the disposal site, where it is discharged into the receiving water body. This method is widely utilized by the majority of seawater desalination plants. However, its feasibility depends on whether the brine's composition aligns with that of the receiving water body to avoid harmful effects on the marine environment [63,64]. Brine can pose risks due to its elevated salinity or the

presence of pollutants not naturally occurring in the receiving water. For instance, before discharge, the brine can be diluted with regular seawater or municipal wastewater to reduce its salinity level [65]. Research indicates that careful dilution and rapid mixing can mitigate adverse impacts [66]. The cost of this disposal method typically ranges from US$0.05/m³ to US$0.30/m³ of rejected brine [65,67].

Sewer Discharge

Sewer discharge is a brine disposal method that involves releasing brine into the wastewater collection system. This approach is commonly favored by small-scale brackish water desalination plants, primarily due to concerns about the adverse effects of the brine's high TDS content on the receiving wastewater treatment plant [68]. The high salinity of brine can impede the biological treatment process in a wastewater treatment plant, particularly when the TDS concentration of the influent exceeds 3000 mg/L [69]. As a result, sewer discharge is predominantly utilized by brackish water desalination plants and is seldom employed for seawater desalination purposes. The cost of this disposal method typically ranges from US$0.32/m³ to US$0.66/m³ of rejected brine [65,67].

Deep-Well Injection

Deep-Well Injection, a technique for disposing of brine, involves the careful injection of brine into deep underground aquifers that are sufficiently isolated from the water aquifers above. This method is commonly employed by brackish water desalination plants. The process entails injecting the brine into a well-equipped with multiple layers of casing. Porous rocks are utilized to confine the brine, while impermeable formations such as clay serve to prevent contamination of the water

aquifers [70,71]. The receiving aquifer must have the capacity to accommodate the brine generated over the plant's operational lifespan, which typically spans 25 to 30 years [72,73]. A primary environmental concern associated with deep-well injection is the potential contamination of nearby water aquifers that may serve as sources of drinking water [74]. The cost of employing this disposal method typically falls within the range of US$0.54/m3 to US$2.65/m3 of brine discharged [65,67].

1.3.2. Freeze Desalination (FD)

Freeze desalination (FD) technology presents a promising solution to circumvent common challenges encountered in traditional desalination methods. Unlike thermal-based methods, which often face issues such as high energy consumption and corrosion, or membrane-based methods, which contend with fouling and demanding pretreatment requirements, FD offers an alternative approach. In FD, the process involves the partial or complete freezing of the solution, wherein newly formed ice crystals gradually enlarge, displacing impurities, including salts, into the remaining brine solution. Freshwater is then obtained in the form of ice blocks or ice crystals [75]. The produced ice is subsequently separated from the highly saline brine, washed, and finally melted to yield pure water.

Freeze desalination has several attributes that address the limitations of major desalination technologies, namely thermal-based desalination, and membrane-based desalination. Unlike membrane-based processes, FD is insensitive to fouling issues, a common challenge in membrane desalination, where cleaning fouled membranes can be exceedingly challenging [76,77]. Additionally, unlike RO, which necessitates extensive pretreatment and chemical additives, FD operates without such requirements. RO typically generates concentrated brine, posing environmental concerns, whereas FD shows promise in treating this concentrated brine toward

achieving close to zero liquid discharge [78]. Moreover, FD encounters minimal scaling and corrosion problems due to its lower operating temperatures compared to thermal desalination processes. From an energy perspective, the latent heat of ice fusion in FD is significantly lower at 333 kJ/kg compared to the 2500 kJ/kg required for water evaporation in thermal desalination processes [79]. Consequently, FD demands approximately one-seventh of the energy needed for thermal desalination. Furthermore, FD exhibits versatility in handling highly concentrated brines, offering flexibility in treatment options [80].

Freeze desalination involves a phase change, transitioning from liquid to solid, with saline water or brine transforming into ice. The freezing process results in the formation of ice crystals, predominantly composed of pure water [81]. Consequently, fresh water is extracted in the form of ice, leaving behind a more concentrated liquid. FD relies heavily on refrigerants to achieve the lower temperatures required for operation [82]. Typically, based on freezing conditions and processes, freeze desalination configurations can be categorized into four main types: Direct, Indirect, Eutectic, and Vacuum freezing, each defined by specific operational parameters [83]. In direct FD, the refrigerant comes into direct contact with the saline solution. Conversely, in indirect FD, a thermally conducting solid surface separates the refrigerant from the solution, with heat transferred from the solution through the conducting surface cooled by circulating refrigerant. Both direct and indirect FD operate with cooling temperatures below the freezing point of the solution. If the operational cooling temperature is further reduced to reach the eutectic point, eutectic freezing (EF) occurs [84]. The eutectic point is the lowest temperature at which the liquid phase is stable. Below the eutectic point, only solid phases exist. In EF, salt crystals and ice form simultaneously. Additionally, vacuum freezing operates under high vacuum pressure to rapidly vaporize a portion of the water, extracting significant heat from the solution (refrigeration effect)

and facilitating the freezing of the remaining portion into fresher ice [85]. In the subsequent sections, two of the most prevalent FD systems, the indirect and direct methods, are explored in great detail.

Indirect Freeze Desalination

In indirect freeze desalination, the saline solution and refrigerant are kept separate by a solid barrier, with heat from the solution transferred through this barrier to the refrigerant [86]. There are two primary categories of indirect FD: suspension crystallization and progressive freezing on a cold surface [79]. In suspension crystallization, the pre-cooled saline solution is circulated through a scraped-surface heat exchanger operating at low sub-cooling temperatures to facilitate the nucleation of small crystals. The resulting slurries are then returned to the main vessel for ice growth, with the ice subsequently separated from the slurry using a filter [76]. However, suspension crystallization typically falls short of reaching freshwater standards due to the small size of the ice crystals and the contamination of their surfaces by salt [87]. Furthermore, the costs and complexities associated with achieving freshwater standards through suspension crystallization are considerably higher compared to those required for progressive freezing [88,89]. In progressive freezing, a single ice layer is initially formed on the cooled surface, gradually increasing in thickness as the remaining brine comes into close contact with the ice for further crystallization. The primary advantage of freezing desalination on a cold plate lies in the higher quality of the produced ice. The ice forms layer by layer in a one-dimensional direction, minimizing impurities entrapped between ice crystals and simplifying the separation of ice and saline water.

Direct Freeze Desalination

Direct contact freezing desalination employs refrigerant directly in contact with the solution to be frozen [79]. Pressurized liquid refrigerant is injected into the brine solution, causing expansion and vaporization within the solution at low pressure. This process results in the absorption of a substantial amount of heat from the solution, enhancing cooling and lowering it to its freezing point to form ice crystals [90]. One advantage of direct FD is its exceptionally high surface area and heat transfer coefficient due to the direct interaction between the brine solution and the refrigerant. It is widely regarded as the most efficient FD mode, utilizing insoluble refrigerants such as butane and Freon, which evaporate upon contact with seawater, drawing latent heat from the brine and facilitating ice crystal formation [91]. Critical to the success of direct FD is the careful selection of refrigerant. It should possess a boiling point lower than -4°C, exhibit low vapor pressure at room temperature, be non-toxic, immiscible, chemically stable in seawater, and resistant to hydrate formation during expansion [92]. Additionally, the refrigerant should be readily available from commercial suppliers at an affordable price [93]. Despite its high cooling efficiency, direct FD has notable drawbacks. One concern is the potential contamination of the produced ice by the refrigerant, rendering it unsuitable for potable water [94]. Moreover, the use of explosive refrigerants like butane raises safety concerns [94]. Current research in direct FD is increasingly exploring the utilization of waste cold energy released from LNG regasification processes [87,95]. A typical direct contact freeze desalination system comprises ice crystallization components and ice separator units [96].

Ice Crystallization Unit

Refrigerant, maintained in a pressurized liquid state, is expanded into the brine solution, where it undergoes vaporization at low pressure. This vaporization induces a refrigeration effect, leading to the formation of ice crystals within the brine [83]. The quality of these ice crystals depends on the circulation of the immiscible refrigerant [97]. Optimal mixing methods include utilizing fine spray nozzles to introduce liquid refrigerant in the brine, pumping vapor from the vapor space through a spurge system for reintroduction in the brine, rapidly circulating the entire liquid content of the freezer, and employing conventional mechanical agitators [98]. Alternatively, a spray freezer approach involves spraying refrigerants and brine into a low-pressure space, resulting in instantaneous slurry formation.

Ice Separation Unit

Ice crystals must undergo separation from the brine, which adheres to them due to interfacial tension. Ice crystals formed within the crystallization unit are gathered and transferred to an ice separator to rid them of adhered brine. Separation devices fall into several categories: presses, gravity drainage systems, hydrocyclone separators, centrifuges, filters, and wash columns [99,100]. Filtration has proven less effective for crystal separation, posing challenges in removing adhered brine. Frequently, screens or filters experience freezing issues, with brine freezing in the openings. Wash columns emerge as the preferred choice for ice washing and brine rejection [101]. Efficient removal of adhered brine presents one of the most challenging unit operations.

Among the most prevalent methods is the wash column, which can take the form of either a flooded or drained column [102]. Wash columns come in two types: pressurized and gravity-based. In a pressurized wash column, crystals ascend to the top while hydraulic pressure compels

a wash liquid, derived from melted pure crystals, to descend. This liquid, as it flows down the column, purges impurities from the crystal surfaces. At the interface between washed and unwashed crystals, known as the wash front, the wash liquid encounters colder crystals, enhancing crystallization. Consequently, the wash liquid remains separate from the concentrated liquid [83]. The gravity wash column, though simpler in design, requires larger dimensions than its pressurized counterpart. Its increased height generates the necessary pressure to compress the ice bed. Functioning similarly to the pressurized column but at lower pressures, it still facilitates the hydraulic movement of an ice pack up the column. To overcome challenges posed by surface tension forces, clean fresh water can act as a displacing liquid. Enhanced separation via drainage occurs when, in addition to draining brine from the bottom of ice crystals, pure water is introduced at the top of the batch, filtering through the ice bed interstices to displace the brine. The effectiveness of wash columns hinges on factors such as crystal size, shape, and the viscosity of concentrated brine. Ensuring uniformity in crystal size and shape is crucial to prevent wash water from unevenly permeating through the crystals, potentially following paths of least resistance.

Centrifuges have been employed for separating ice crystals from concentrated brine as well. Filtering centrifuge leverages the disparity in specific gravity between ice crystals and brine concentrate, with centrifugal force propelling the brine through the filter basket. Typically, water rinsing is necessary to ensure there is no salt carryover. Additionally, ice particles from brine can be separated using a filter.

2. Design and Fabrication of a Novel Freeze Desalination System[1]

In this chapter, the innovative freeze desalination system is introduced, providing a comprehensive and detailed explanation of its mechanism. The section starts with an overview of freeze desalination, exploring its applications across various industries, examining different methodologies, and comparing these approaches. A thorough literature review of direct contact freeze desalination systems is also included to contextualize the current advancements and identify gaps in existing technologies. Subsequently, a detailed presentation of the experimental setup is provided, and each component used in the system is described in detail.

2.1. Literature Review & State of the Art

The freeze desalination method involves cooling saline water until it partially freezes, resulting in the extraction of freshwater in the form of ice while the remaining unfrozen brine becomes more concentrated. [81]. This method experiences fewer issues related to scaling, fouling, and corrosion due to its operation at low temperatures [103]. Additionally, from an energy perspective, the freezing process is inherently less energy-intensive than evaporation, with the latent heat of fusion of water being almost one-seventh of its latent heat of evaporation [103]. Hence, freeze desalination is a viable option for treating rejected brine from reverse osmosis processes, thereby moving towards zero liquid discharge. Moreover, freeze desalination systems require minimal pretreatment of the feed brine, resulting in significantly fewer chemicals discharged into the environment [104]. Researchers have explored the application of freeze desalination in various fields, including the treatment of oil and gas produced water [105], the concentration of fruit juice

[1] The content of this chapter is an extension of a published paper by the author. The paper contains results of research which was solely conducted as partial fulfillment for the PhD requirement. Materials presented in the paper have not been submitted for a course or extra credit.

and glucose solutions [106,107], dairy products [108], pharmaceutical applications [109], and wastewater treatment [110].

Freeze desalination can be classified into direct and indirect contact methods based on the interaction between the brine and refrigerant. [76,111]. In the direct FD method, a refrigerant directly contacts the saline solution, whereas the indirect FD method utilizes a thermally conducting solid surface to separate the refrigerant from the saline water. In both direct and indirect FD processes, the cooling temperature is maintained below the freezing point of the solution [112]. Various experimental and numerical investigations [113–116] have explored both direct and indirect contact FD methods. Indirect FD can be broadly categorized into two types: suspension freeze crystallization and layer freeze crystallization [112]. Suspension freeze crystallization involves the creation of numerous small suspended ice crystals within a cooled scraped-surface heat exchanger, which then grows in a stirred growth vessel before undergoing separation [103]. On the other hand, layer freeze crystallization results in the formation of an ice crystal layer on the cooling surface. Studies on indirect FD systems have indicated that as the salinity of the feed brine increases, both the recovery ratio (the mass ratio of produced ice to feed brine) and the desalination rate (the ratio of salt mass in the unfrozen concentrated brine to that in the feed brine) decrease [104,117,118]. Additionally, reducing the cooling temperature increases the recovery ratio [119] while decreasing the desalination rate [104]. Various techniques such as ice pressing [120,121], sweating [122], washing [89], and centrifugation [118,123] are employed to improve the quality of the produced ice and lower its salinity. Desalination rates of up to 99% have been reported for indirect FD methods in certain experiments [120,123,124]. However, these high desalination rates often coincide with low recovery ratios. Multi-stage FD, where treated water is reintroduced into

the system multiple times to further reduce the salinity of the final product, has also been investigated [125].

One of the pioneering studies on direct freeze desalination was conducted by Landau and Martindale [126], who explored the influence of various operational parameters on ice quality. Their research demonstrated that reducing the salinity of the feed brine and the flow rate of the refrigerant significantly enhanced the quality of the ice produced. Gibson et al. [127] investigated the spray freezing of seawater, employing a technique in which Freon-114 and saltwater feed were atomized through nozzles. To extract the residual Freon from the ice crystals, they utilized a pressurized wash column and emphasized the necessity of maintaining adequate turbulence to prevent the formation of an ice-cake layer near the spray nozzles. Further exploration of continuous brine crystallization was conducted by Wiegandt et al. [97], who utilized butane as the refrigerant. Their findings indicated that atomizing the liquid refrigerant significantly increased the heat transfer area and promoted vigorous turbulent flows, thus enhancing the efficiency of the heat transfer process. More recent advancements by Xie et al. [87] introduced an innovative freeze desalination setup leveraging cold energy from liquefied natural gas (LNG) to cool a secondary fluid, which was then mixed with seawater. In their experiments, HFE-7100 was used as the intermediate cooling liquid and injected into a cylinder containing seawater to facilitate ice formation. Their results showed an increase in the ice generation rate with a reduction in the refrigerant temperature, although this also led to a decrease in the desalination rate. However, the use of HFE-7100 presented challenges due to its high vapor pressure at room temperature (26.9 kPa), which could lead to significant losses of the cooling liquid through evaporation. Additionally, the cost of HFE-7100 is relatively high, and it has a modest specific heat, which may limit its practical application in large-scale systems [128,129].

The literature suggests that the main advantage of indirect FD lies in producing refrigerant-free treated water of potentially higher quality, a result of the slower and more controlled freezing process that minimizes brine entrapment within the ice crystals [112]. Conversely, direct FD methods are favored for their higher ice production rates, due to the improved heat transfer between the refrigerant and saline water [86], and lower specific power consumption compared to indirect FD methods [112]. However, indirect FD suffers from higher energy demands due to less efficient heat transfer between the refrigerant and feed brine and increased complexity in system design, notably in the removal of ice from cooling surfaces [76]. Direct FD methods, while efficient, often have issues such as contamination from the residual refrigerant in the treated water and challenges in precisely controlling the freezing process, both of which can adversely affect water quality [130]. Additionally, a common challenge across both direct and indirect FD approaches is the effective separation of residual brine from the ice before melting. Failure to adequately remove this brine leads to its dissolution in the melted ice, thereby elevating the salinity of the final treated water [103].

Given the research on FD technologies and designs detailed in existing literature, there is a notable deficiency in systems that effectively integrate the advantages of both direct and indirect FD methods while mitigating their respective drawbacks. A hybrid FD system could potentially offer more effective solutions for desalinating high-concentration brines and facilitate their widespread application. This study aims to bridge this research gap by introducing an FD system that merges aspects of both direct and indirect methods. In this design, the cooling fluid and the brine are mixed directly; however, unlike traditional direct FD systems that mix the refrigerant fluid from the refrigeration cycle with the brine, this system uses an intermediate cooling liquid—specifically silicone oil, which circulates between the refrigeration and desalination units. Silicone

oil is selected for its notable benefits, including its non-volatility at room temperature, higher specific heat, and significantly lower cost compared to other fluids [129,131,132]. Furthermore, this FD system incorporates an innovative ice-crushing technique that minimizes brine entrapment and improves the desalination rate. The primary aim of this research is to demonstrate the viability of a novel FD system that utilizes an intermediate cooling liquid to overcome the limitations traditionally associated with FD systems. The novelty of the current study lies in combining the advantages of both direct and indirect contact freezing desalination methods. It operates at atmospheric pressure, similar to indirect contact methods, while achieving a high heat transfer rate due to the direct contact between the brine and the cold medium (ICL), similar to direct contact methods. Additionally, the ICL used in this study does not bond with the water and can be easily separated from the water.

2.2. Experimental Setup

The experimental freeze desalination study began with the fabrication of a small-scale experimental setup designed to evaluate the feasibility of the desalination process [133]. This initial setup included all the essential components for crystallization and brine desalination, except for the ice separation unit. The refrigeration system in this setup was a chiller, which provided the necessary cooling for the brine freezing process. The small-scale setup yielded promising results, demonstrating the possibility of ice crystallization with low-salinity feed brine. Building on these successful initial findings, the researchers moved to the next stage: the development and testing of a large-scale setup. This larger system was designed to increase the ice production rate and extend the application of freeze desalination to high-salinity feed brine by utilizing a more powerful refrigeration system.

The large-scale experimental setup is fabricated and tested to evaluate the performance and effectiveness of the proposed novel freeze desalination system. This setup utilizes an intermediate cooling liquid (ICL) as the cooling medium, facilitating heat transfer between the desalination unit and the refrigeration unit [134]. The ICL circulates between the refrigeration system and desalination unit supplying the necessary cold medium for the freeze desalination process. The specifics of this process will be detailed in the subsequent sections. Figure 2-1 presents both the actual and schematic views of the fabricated desalination system. The setup consists of two main components: the desalination unit and the refrigeration unit, interconnected by the ICL via an evaporator. The ice separation and ice melting processes are handled by distinct units, which will be explained in greater detail in the following sections. The primary function of the refrigeration unit is to supply a cold environment for the ICL, which then comes into contact with the feed brine. The main role of the desalination unit is to generate ice crystals. The ICL, a silicone fluid, continuously circulates between the evaporator section of the refrigeration unit and the desalination unit, ensuring efficient and effective cooling throughout the process.

(a)

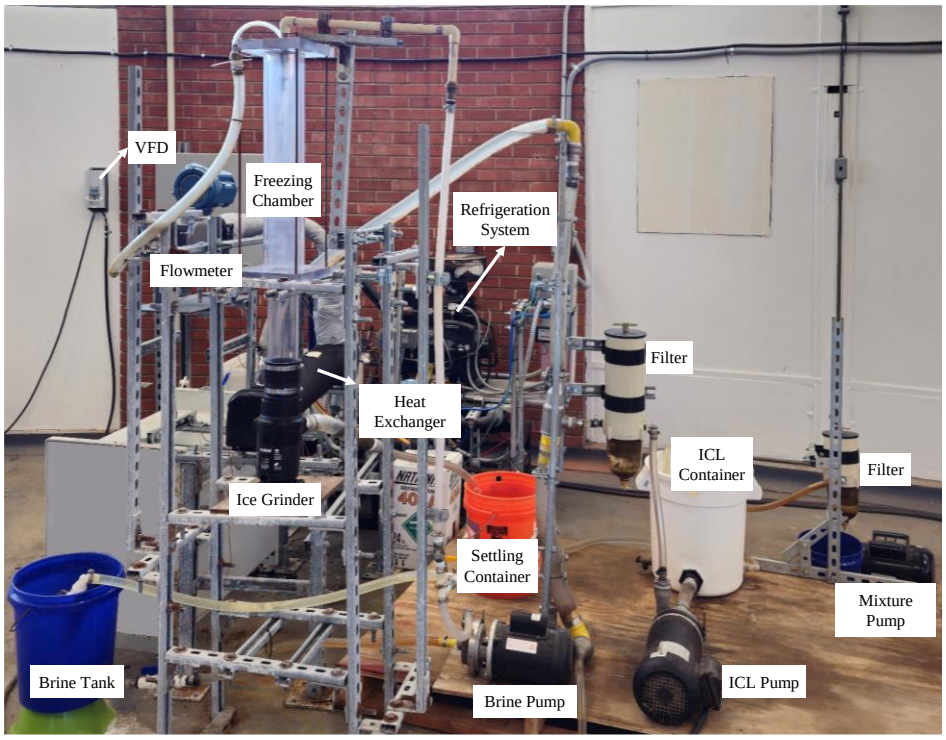

(b)

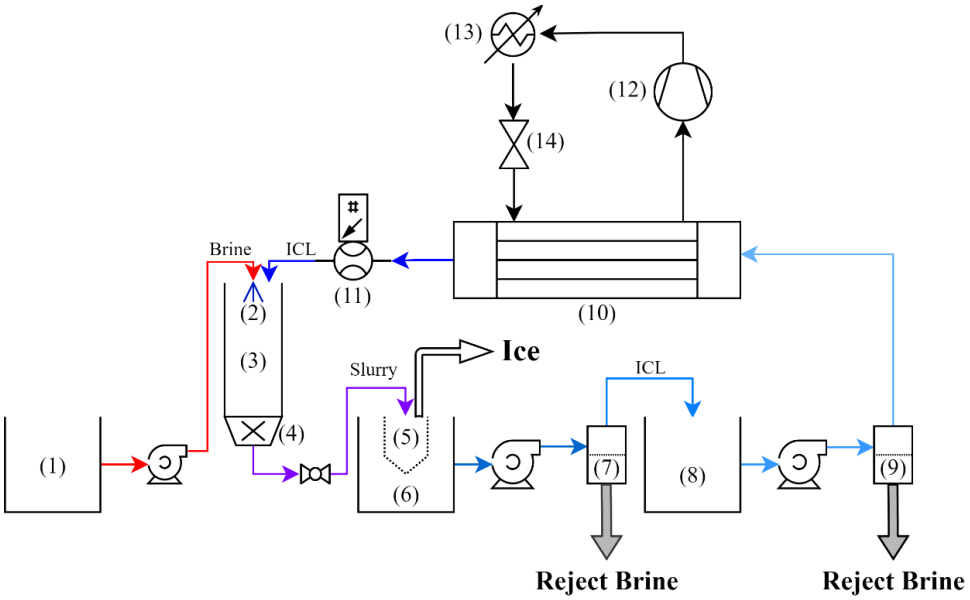

Fig. 2-1 (a) Experimental setup and (b) schematic view of it. The components in the schematic view: (1) brine tank, (2) brine spray nozzle, (3) freezing chamber, (4) ice grinder, (5) ice-liquid separation filter bag, (6) settling tank, (7) first brine-ICL separation filter, (8) ICL tank, (9) second brine-ICL separation filter, (10) heat exchanger, (11) flowmeter, (12) compressor, (13) condenser, (14) expansion valve.

The desalination unit comprises several sections, including brine preparation, brine injection, crystallization, slurry separation, a filter separator, and ICL cooling. The process begins in the brine preparation section, where the brine is prepared and then injected into the freezing chamber. Within the freezing chamber, the injected brine is partially frozen and mixed with the cold ICL. This creates a slurry composed of ICL, ice, and unfrozen concentrated brine. The slurry is then transferred to the slurry separation section, where the solid ice crystals are separated from the liquid components (ICL and concentrated brine). The collected ice is moved to the ice separation section, while the remaining ICL and concentrated brine proceed to the filter separator. In the filter separator, the ICL is separated from the concentrated brine. The concentrated brine is rejected from the system and the separated ICL is then pumped to the evaporator of the refrigeration system to be cooled before being circulated back to the freezing chamber, thus completing the cycle. Further details of each section in the desalination unit, along with the ice separation and ice melting processes, will be provided in the subsequent sections. The component numbers mentioned in the following sections correspond to those shown in Fig. 2-1(b).

2.2.1. Intermediate Cooling Liquid (ICL)

Before exploring the various components of the freeze desalination setup, it is crucial to first introduce the ICL and discuss its properties. Choosing the appropriate ICL is a crucial step in this experimental study. The selected liquid must possess several key characteristics: non-toxicity, immiscibility with water, low viscosity, low freezing temperature, availability, and affordability. After careful evaluation of these criteria and reviewing previous research, two fluids emerged as suitable candidates for the study: HFE-7100 and PSF-1.5 cSt Silicone Fluid. HFE-7100 fluid is a hydrofluoroether (HFE) fluid, characterized by its very low toxicity and immiscibility with water. It has an extremely low freezing

temperature of -135°C and a kinematic viscosity of 0.38 cSt at room temperature, making it highly effective for this application. Similarly, PSF-1.5 cSt Silicone Fluid also has low toxicity and is immiscible with water. It features a freezing temperature of -70°C and a low kinematic viscosity of 1.5 cSt at room temperature.

When comparing PSF-1.5 cSt Silicone Fluid with HFE-7100, silicone oil offers several important advantages. Firstly, silicone oil has a vapor pressure of 0.13 kPa at 25°C, making it non-volatile at room temperature. In contrast, HFE-7100 has a much higher vapor pressure of 26.9 kPa at 25°C, indicating greater volatility under the same conditions. Additionally, silicone fluid has a higher specific heat than HFE-7100. Specifically, the specific heat of PSF-1.5 cSt silicone fluid is 1715 J/kg·K at 25°C, compared to 1183 J/kg·K for HFE-7100 [128]. Furthermore, the cost per kilogram of silicone fluid is significantly lower than that of HFE-7100, making it a more economical choice for large-scale applications [129,132,135]. Finally, in this experimental setup, the produced ice must sink so that it can be effectively transported through the system. This downward movement of ice requires the ICL to have a lower density than ice. The HFE-7100 fluid has a density of 1520 kg/m³, which is higher than the density of ice. This higher density makes it difficult, if not impossible, for the ice to descend into the freezing chamber. Conversely, the PSF-1.5 cSt Silicone Fluid has a density of 851 kg/m³, which is lower than that of ice. This lower density facilitates the practical and efficient descent of ice within the freezing chamber. Given these advantages, silicone fluid was selected for this experimental study. The PSF-1.5 cSt Silicone Fluid, a type of Polydimethylsiloxane (PDMS) silicone fluid, is marketed under various names by different companies. For this study, the silicone fluid was purchased from Clearco Products company. The thermophysical properties of the ICL are detailed in Table 2-1 [131].

Table 2-1 Thermophysical properties of silicone liquid (ICL) [131]

Freezing point	-70°C
Specific gravity at 25°C	0.851
Specific heat capacity at 25°C	1,715 J/kg·K
Viscosity at 25°C	1.5 cSt
Viscosity at -25°C	3 cSt
Vapor pressure 25°C	0.13 kPa

2.2.2. Refrigeration Unit

The role of the refrigeration unit is to cool the ICL to the desired temperature. This unit is composed of several components: a compressor, a condenser, an expansion valve, and an evaporator. The refrigerant used in this system is R404-A. The compressor is a two-stage low-temperature compressor, specifically the Copelametic 2DL3F20KE-TFC model. It operates within an evaporating temperature range of -18°C to -40°C and a condensing temperature range of 4°C to 60°C [136]. In the current experimental study, the evaporating temperature is maintained between -20°C to -30°C, depending on the required temperature of the ICL. The condensing temperature varies from 30°C to 40°C, influenced by the ambient temperature and the condenser's cooling efficiency. The nominal power of the compressor under these working conditions ranges from 3.7 kW to 4.8 kW.

The evaporator compartment of the refrigeration unit is a Westermeyer DX5-1 horizontal shell-and-tube heat exchanger, shown in Fig. 2-2. The shell is constructed from steel and the tubes are made of copper. To enhance the cooling effect, the evaporator is equipped with baffles. In the

heat exchanger, the refrigerant R-404A flows through the tube side, while the ICL flows through the shell side, arranged in a counterflow configuration. The entire outer surface is wrapped in 2 cm of insulation to ensure maximum temperature retention. Additionally, the surface is powder-coated to provide enhanced corrosion resistance [137]. This heat exchanger measures 0.9 m in length and has an internal diameter of 0.1 m. The evaporator has a nominal cooling capacity of 6.1 tons, which is equivalent to 21 kW. The cooling capacity of the refrigeration system was regulated by adjusting the electronic expansion valve opening via a LabVIEW graphical user interface, allowing precise control to achieve the desired cooling temperature. During operation, the refrigerant flow rate and temperatures at both the inlet and outlet of the evaporator and condenser were continuously monitored and recorded.

The condenser of the refrigeration system is constructed from a 4.5 m copper tube with an inner diameter of 1 cm. This tube is coiled into a length of 0.5 m, forming nine loops, and is submerged in a water tank. To dissipate the excess heat, cold water is introduced into the tank, and heated water is expelled. While the flow rate and temperature of the incoming water were not measured during the condenser cooling process, the temperatures at the inlet and outlet of the condenser were continuously monitored. This monitoring ensured that the temperatures remained within the operational range of the compressor.

Fig. 2-2 The shell-and-tube heat exchanger and the ICL and refrigerant (R404-A) inlets and outlets.

2.2.3. Brine Preparation

The first step in the desalination unit involves preparing the brine with the desired salinity. For this experimental study, brine was prepared by gradually adding regular table salt to tap water, which initially had a TDS level of approximately 250 ppm. The salt was added incrementally, with thorough mixing to ensure uniformity. The TDS of the resulting feed brine was measured using a Hanna Instruments HI2300 TDS meter. This device measures electrical conductivity (EC), TDS, sodium chloride (NaCl), and temperature. The HI2300 can measure TDS levels ranging from 0 g/L to 400 g/L, with a resolution that varies from 0.001 ppm to 100 ppm depending on the solution's TDS. The accuracy of the device is within 1% of the reading. Additionally, it measures temperature within a range of -20°C to 120°C, with a resolution of 0.1°C and an accuracy of 0.4°C. Salt was continuously added and mixed until the desired TDS level was achieved, as confirmed by the HI2300 instrument.

The elemental composition of table salt was thoroughly analyzed using Scanning Electron Microscopy (SEM) for high-resolution imaging and Energy Dispersive X-ray Spectroscopy (EDX) for detailed elemental analysis. The SEM analysis was conducted with the Thermo Quattro S field-

emission environmental Scanning Electron Microscope (FE-ESEM) at the Samuel Roberts Noble Microscopy Laboratory (SRNML) at the University of Oklahoma. A detailed and colorful image of the solid salt obtained from this microscope is displayed in Fig. 2-3. The EDX analysis provided a comprehensive assessment of the average elemental composition across the five regions highlighted in Fig. 2-3, with the results summarized in Table 2-1. The data indicates that while trace amounts of various elements such as Carbon (C), Oxygen (O), and Molybdenum (Mo) are present in the salt sample, sodium chloride (NaCl) constitutes the majority, accounting for nearly 96% of the total mass. This high concentration of NaCl is consistent with the expected composition of table salt, showing the accuracy and reliability of the SEM-EDX analytical methods used in this study.

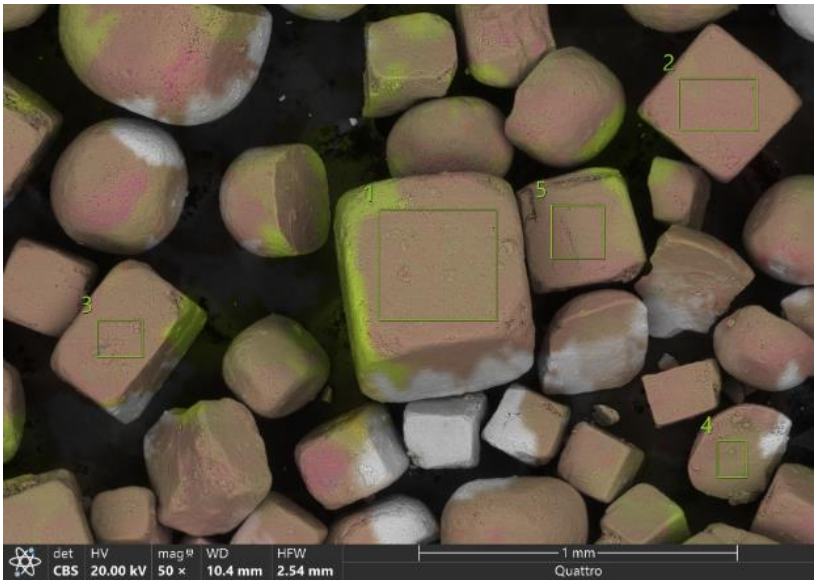

Fig. 2-3 Scanning electron microscopy image of salt crystals.

Table 2-2 The EDX analysis of the salt.

Component	Weight percentage
C	2.6 %
O	1.4 %
Na	37.4 %
Cl	58.5 %
Mo	0.1 %

2.2.4. Brine Injection

After preparing the brine, the solution is transferred to the brine tank (1) for subsequent injection into the freezing chamber (3). Throughout all tests, the feed brine was maintained at room temperature (approximately 20°C), and the flow rate was kept constant at 0.13 kg/min. The brine was pumped from the brine tank and injected into the cold ICL in the freezing chamber via a nozzle (2). This process utilized a stainless-steel, corrosion-resistant centrifugal pump from Utilitech, rated at 60 W. The nozzle tip was positioned above the ICL level in the freezing chamber, producing droplets ranging in size from 50 to 100 micrometers. The small size of these brine droplets enhances heat transfer by increasing the contact surface area between the brine and the cold ICL. However, during the injection process, droplet coalescence can occur before crystallization, leading to the formation of larger ice particles.

2.2.5. Crystallization

The brine is injected into the freezing chamber, which is filled with cold ICL. The ICL is pumped from the ICL tank (8) to the shell and tube heat exchanger (10) and then enters the freezing chamber (3). The flow rate of the ICL is regulated by a pump equipped with a variable frequency drive (VFD). This pump is a three-phase, low-temperature, stainless-steel, corrosion-resistant model from Weg, rated at 2.2 kW. To ensure precise control of the ICL flow rate, an Emerson Micro Motion Coriolis mass flow meter (11) is installed downstream of the heat exchanger. This flow meter, with an accuracy of ±0.1% of the reading, measures the mass flow rate of the ICL. Additionally, the flow meter continuously monitors the temperature of the ICL, ensuring minimal variation in the ICL inlet temperature.

The freezing chamber was constructed from a 1-meter-long polycarbonate cylindrical tube with an inner diameter of 10 cm and a wall thickness of 0.5 cm. Surrounding the upper section of this inner cylinder, a second polycarbonate cylindrical tube with a height of 70 cm and an inner diameter of 12 cm was placed, creating an annular space between the two cylinders. This annular space was evacuated to form a vacuum. The double-wall design around the upper section of the freezing chamber served multiple purposes. Firstly, it prevented condensation on the outer surface of the freezing chamber, thereby enhancing visual access to the freezing process. Secondly, it reduced heat gain, contributing to the thermal efficiency of the system.

As previously mentioned, feed brine is injected from the top of the freezing chamber, where ice crystals begin to form. Due to their higher density compared to the ICL, the ice crystals descend within the freezing chamber. During the crystallization process, the coalescence of brine droplets or ice crystals can occur. To prevent ice agglomeration and clogging, a rotary ice grinder device (4) is

positioned at the bottom of the freezing chamber. This device is essential for crushing larger chunks of ice that may form. Additionally, the ice grinder enhances the mixing and heat transfer between the brine droplets and the ICL by creating a swirling motion within the freezing chamber. This improved circulation not only prevents blockages but also ensures a smoother transition of the slurry, a more uniform temperature distribution, and a more efficient crystallization process.

2.2.6. Slurry Separation

The mixture of ice crystals, unfrozen concentrated brine, and ICL exits the ice grinder and requires ice separation. Several methods were tested for this purpose, including a simple metal filter separator, a rotary separation device, and filter bag separation. The metal mesh filter separator consists of a rectangular metal surface that prevents ice particles from passing through while allowing the liquid to flow freely. Although this method is straightforward, it has several drawbacks. The proximity of the produced ice to ambient temperatures reduces the ice production rate due to ice melting. Additionally, collecting ice from the flat surface of the metal filter can be challenging, often leading to significant ice waste.

The continuously operative rotary separator is designed to efficiently separate ice from the liquid ICL and unfrozen concentrated brine. It features an inner filter tube with a mesh wall that rotates within an outer housing. The mesh wall, made from mesh fabric, allows liquids to pass through while retaining solid particles. As the slurry is fed into the inlet of the inner filter tube, the rotating action facilitates the separation process. The liquid, including ICL and unfrozen concentrated brine, drains through the mesh wall and is collected by the outer housing, which directs it into a settling tank. The solid ice particles, which are larger than the mesh size, are retained within the inner filter tube and transported to an ice tank. The entire separator is mounted

on an inclined setup to aid the efficient movement of ice through the system. Additionally, a DC motor rotates the outer filter tube, with adjustable rotational speed to optimize the separation process. The schematic and actual setup of the rotary separator are shown in Fig. 2-4. While this method can operate continuously, it faces challenges due to ice melting caused by the proximity of the ice to ambient temperatures. To mitigate this issue, combining the continuous rotary separator with a continuous ice washing or ice separation process in a controlled cold environment could enhance its efficiency, providing a continuous ice production unit. However, implementing such an integrated solution was beyond the scope of the current experimental study.

(a)

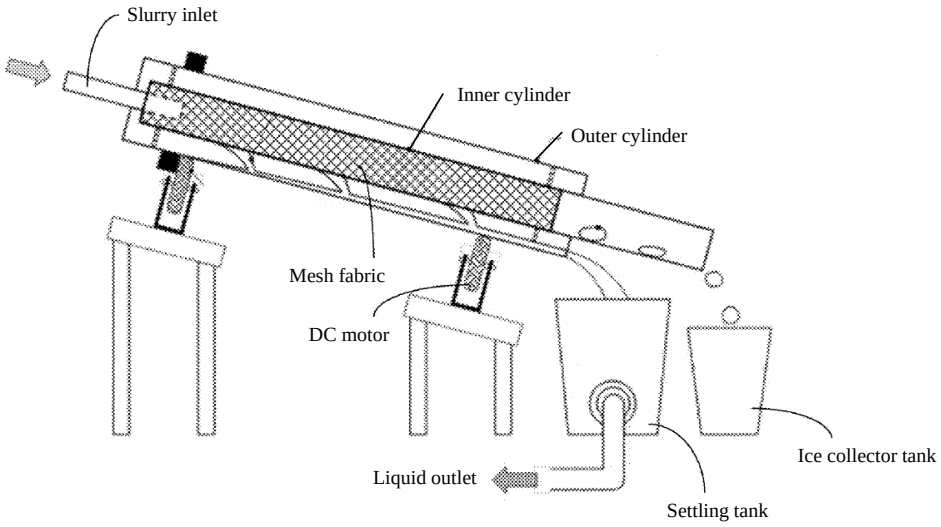

(b)

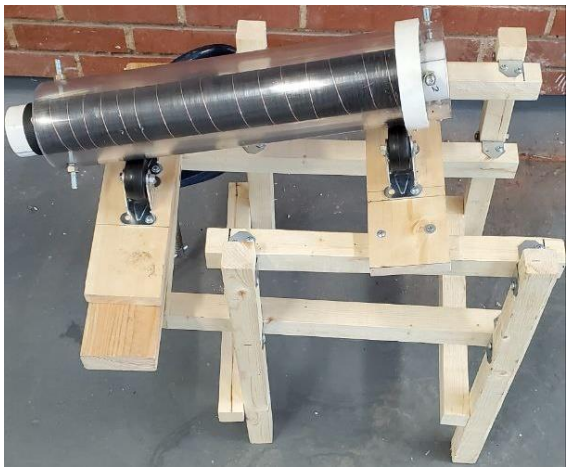

Fig. 2-4 The (a) schematic [138] and (b) actual rotary separator.

The third method for separating ice from the slurry involves using a filter bag separator (5). In this approach, a filter bag is placed inside a settling tank (6), and the slurry exiting the ice grinder is directed into the filter bag through a hose. The filter bag, made of nylon plastic with a very fine mesh, allows the liquid to pass through while trapping the ice particles. As the liquid passes through the bag, it enters the settling tank, while the ice particles accumulate within the filter bag. Because the filter bag is submerged in the cold ICL within the settling tank, ice melting is minimized. Consequently, this method proves to be highly effective for slurry separation and employed in this experimental study.

The liquid mixture passing through the filter bag is pumped to the first ICL-brine separation filter (7). This filter relies on the density difference between the concentrated brine and the ICL to achieve separation. The concentrated brine, being denser, settles at the bottom of the filter, while the dewatered ICL passes through to the main ICL tank. The separated brine is collected at the bottom of the filter and is gradually discharged through a discharge valve. The pump used in this process is a single-phase, low-temperature, stainless-steel, corrosion-resistant model from Weg, rated at 0.7 kW. The flow rate of the liquid out of the settling tank is controlled by adjusting the pump speed with a variable voltage transformer. To ensure complete separation of ICL and brine, a second ICL-brine separation filter (9) is placed after the main ICL tank and before the heat exchanger. This additional filter provides an extra layer of separation, ensuring that any remaining brine is effectively removed before the ICL is recirculated back into the system.

It is important to note that in this experimental study, the hoses, connections, and valves are intentionally left uninsulated to allow for visual monitoring of the ICL and slurry transitions. This design choice enables rapid detection of any potential ICL leaks, facilitates easy observation of ice formation and crystal growth, and allows for the visual tracking of any unfrozen concentrated

brine mixing with the ICL. However, this lack of insulation does have its drawbacks. The uninsulated components are prone to condensation on their outer surfaces, which increases the energy consumption of the desalination setup.

2.2.7. Ice Separation & Melting

During the partial freezing of the feed brine inside the freezing chamber, the concentration of the unfrozen brine increases as the salt is repelled from the forming ice crystals. Some of this brine adheres to the surface of the ice crystals or becomes trapped within them. Additionally, although the collected ice is predominantly solid, some amount of ICL can also attach to the ice crystals. Thus, the ice separation step is crucial in the freeze desalination process to achieve low-salinity treated water. As mentioned in the slurry separation section, the produced ice is collected in a filter bag submerged inside the settling tank. The separated ice, which contains residual concentrated brine and ICL, is referred to as “wet ice” in subsequent discussions. To achieve effective brine rejection while maintaining high ice production, various liquid rejection and ice-washing methods were tested, including wash columns, ice pressing, and centrifugal separation. After evaluating these methods, centrifugal separation was chosen as the most effective technique for separating brine and ICL from the wet ice. This method demonstrated significant performance in brine rejection without requiring additional external washing water.

The collected wet ice is placed inside a centrifugal device known as a spin dryer. The spin dryer is a cylindrical container with a metal inner surface and small holes on its walls. Once the wet ice is loaded, the spin dryer rotates at a high speed of 3200 rpm, effectively expelling the remaining liquid from the ice through centrifugal force. The duration of the spinning process determines the amount of liquid removed, resulting in drained ice with significantly reduced liquid content. The

expelled liquid, which consists of both ICL and unfrozen concentrated brine, can be efficiently separated through gravitational separation due to the density difference between the two. The density of the unfrozen brine is 30% to 35% greater than that of the ICL. This separation process is further facilitated by the immiscibility of the ICL and brine, as well as the low viscosity of the ICL. To ensure the ice remains below its melting point during centrifugation, the spin dryer is placed inside a freezer maintained at around -10°C. After the centrifugation process, the drained ice is retrieved from the spin dryer. Its mass and TDS are then measured after melting the ice at room temperature.

3. Theoretical Analysis of the Developed Freeze Desalination System[2]

To effectively correlate the experimental results with a theoretical framework, this chapter provides an analysis of the feed brine crystallization and ice production processes. This chapter begins by providing a detailed description of the brine crystallization process. Subsequently, the established theoretical model is introduced and explained, which is based on an energy balance analysis conducted specifically within the freezing chamber of the experimental setup. The developed model incorporates a set of assumptions and integrates some findings from the experimental findings to effectively predict the rate of ice production under various operating conditions.

3.1. Brine Freezing Process

Before studying the theoretical analysis of the energy balance during crystallization, it is essential to understand the brine freezing process. When the feed brine is sprayed into the cold ICL, the temperature of the brine droplets decreases until it reaches the freezing temperature corresponding to the TDS of the feed brine. The phase diagram of a basic binary salt-water solution, as shown in Fig. 3-1, illustrates this process. Starting at point "A," which represents the initial condition of the feed brine with a certain salinity, the cooling process does not affect the brine's salinity until the temperature reaches the ice line at point "B" (also known as the liquidus line). Upon further cooling, water is partially removed from the solution in the form of ice, increasing the salinity of the remaining unfrozen brine along the ice line. As the temperature continues to decrease, both the quantity of ice and the salinity of the remaining brine increase. Eventually, further cooling brings

[2] The content of this chapter is an extension of a published paper by the author. The paper contains results of research which was solely conducted as partial fulfillment for the PhD requirement. Materials presented in the paper have not been submitted for a course or extra credit.

the solution to the eutectic point "C" [139]. At temperatures lower than the eutectic point, the solution reaches a state where salt-hydrate and ice form simultaneously, leaving no liquid phase remaining [112].

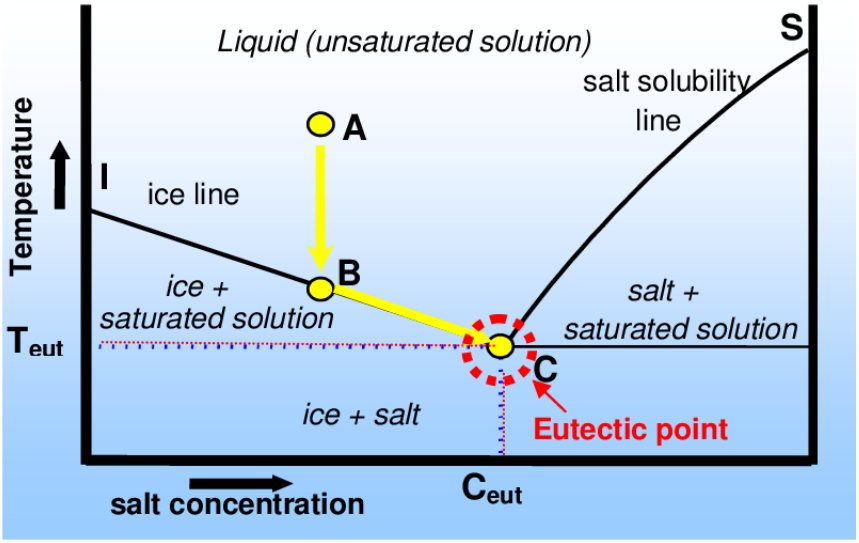

Fig. 3-1 Phase diagram of a binary salt-water solution [140].

3.2. Energy Balance Study

The objective of the theoretical study is to determine the recovery ratio based on the thermophysical properties of the feed brine and ICL, as well as their respective flow rates and temperatures. To achieve this, the energy balance within the freezing chamber during the crystallization process must be solved. Figure 3-2 illustrates the inlet and outlet streams of the freezing chamber. The inputs include the feed brine and cold ICL, while the outputs consist of ice, unfrozen concentrated brine, and ICL. In addition to the input and output streams, heat transfer with the ambient environment also affects the freezing chamber and must be accounted for in the energy balance.

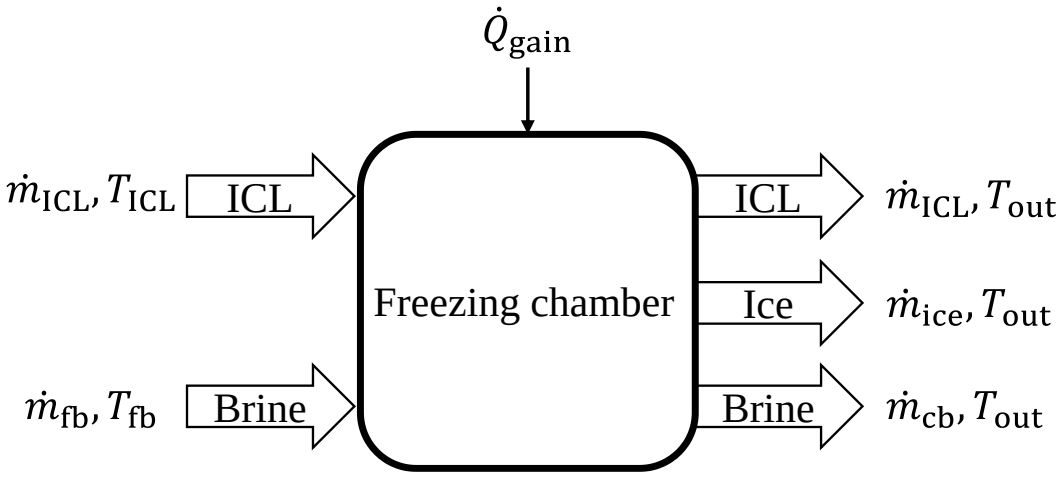

Fig. 3-2 Freezing chamber inlet and outlet streams.

To solve the energy balance during the crystallization process, several assumptions need to be made:

1. The mixture in the freezing chamber is well mixed and all components, namely, ice, unfrozen concentrated brine, and ICL leave the freezing chamber at the same temperature.
2. The specific heat and density of the ICL are constant.
3. The salt is pure sodium chloride.

Among these assumptions, the first one is the most crucial and simplifying assumption. It asserts that the outlet mixture has sufficient time to reach a steady state, maintaining a constant temperature for all exiting components. Although the energy balance is focused on the freezing chamber, the mixture at the chamber outlet can be extended to the outlet mixture immediately before the slurry separation without introducing any additional assumptions or modifications. This extension can further support the constant temperature assumption at the exiting stream. This assumption also implies that the outlet mixture temperature is equal to the freezing temperature of the concentrated brine, as depicted in Fig. 3-1.

By applying the conservation of energy, the energy entering the chamber through the feed brine and ICL must equal the energy leaving through the ice, unfrozen brine, and ICL, plus any heat gained from the ambient. The energy balance for the freezing chamber is as follows:

$$\dot{m}_{\mathrm{ICL}} c_{\mathrm{ICL}} (T_{\mathrm{out}} - T_{\mathrm{ICL}}) = \dot{m}_{\mathrm{fb}}\, c_{\mathrm{avg}} (T_{\mathrm{fb}} - T_{\mathrm{out}}) + \dot{m}_{\mathrm{ice}} h_{\mathrm{sl}} + \dot{Q}_{\mathrm{gain}} \qquad 3\text{-}1$$

where $\dot{m}_{\mathrm{ICL}}$, $\dot{m}_{\mathrm{fb}}$, and $\dot{m}_{\mathrm{ice}}$ are the mass flow rates of ICL, feed brine, and generated ice, respectively, c_{ICL} and c_{avg} are the specific heat of the ICL, and the mass-averaged specific heat of the ice-brine mixture, respectively, and h_{sl} is the latent heat of fusion of ice. Also, in Eq. 3-1, T_{ICL}, T_{fb}, and T_{out} are the temperature of the inlet ICL, the feed brine, and the outlet mixture, respectively, and $\dot{Q}_{\mathrm{gain}}$ is the heat gain from the ambient to the freezing chamber due to imperfect insulation. The mass-averaged specific heat of the ice-brine mixture is defined as:

$$c_{\mathrm{avg}} = \frac{\dot{m}_{\mathrm{fb}}\, c_{\mathrm{fb}} + \dot{m}_{\mathrm{ice}}\, c_{\mathrm{ice}} + (\dot{m}_{\mathrm{fb}} - \dot{m}_{\mathrm{ice}}) c_{\mathrm{cb}}}{2\, \dot{m}_{\mathrm{fb}}} \qquad 3\text{-}2$$

where c_{fb}, c_{ice}, and c_{cb} are the specific heat of the feed brine, produced ice, and concentrated brine, respectively. The recovery ratio is defined as the mass flow rate of the produced ice to that of the feed brine:

$$R = \frac{\dot{m}_{\mathrm{ice}}}{\dot{m}_{\mathrm{fb}}} \qquad 3\text{-}3$$

Equations 3-1 and 3-2 can be rewritten using the recovery ratio as:

$$\dot{m}_{\mathrm{ICL}} c_{\mathrm{ICL}} (T_{\mathrm{out}} - T_{\mathrm{ICL}}) = \dot{m}_{\mathrm{fb}} \left[c_{\mathrm{avg}} (T_{\mathrm{fb}} - T_{\mathrm{out}}) + R h_{\mathrm{sl}} \right] + \dot{Q}_{\mathrm{gain}} \quad 3\text{-}4$$

$$c_{\mathrm{avg}} = \frac{1}{2} \left[c_{\mathrm{fb}} + R\, c_{\mathrm{ice}} + (1 - R) c_{\mathrm{cb}} \right] \quad 3\text{-}5$$

Based on the second assumption, the thermophysical properties of the ICL, such as density and specific heat, are considered constant. The mass flow rates of both the injected brine and the flowing ICL are measured and known in this study. In contrast, the thermophysical properties of the exiting concentrated brine, including density and specific heat, vary according to its concentration. As crystallization occurs, the concentration of the unfrozen brine increases gradually, leading to continuous variation in the latent heat of fusion of the remaining brine. This increase in concentration also results in a continuous decrease in the brine's freezing point. Therefore, it is necessary to define these properties as functions of brine salinity. The variations in these properties as functions of brine salinity are described by the equations presented in Table 2-3, where S denotes the salinity in grams of salts per kilogram of brine $S = m_s/m_b$ (g/kg). Although these properties are derived for aqueous sodium chloride, they can be applied with acceptable accuracy to this study since sodium chloride constitutes about 96% of the salt used.

Table 3-1 Thermophysical properties of aqueous sodium chloride as a function of salinity S (g/kg) [141–143]

Property	Equation
Density (kg/m^3)	$\rho_b = S + 997$
Specific heat capacity ($kJ/kg \cdot K$)	$c_b = -0.0007232\,S + 4.178$
Latent heat of fusion (kJ/kg)	$h_{sl} = -0.0003\,S^2 - 0.074\,S + 333$
Freezing temperature (°C)	$T_{frz} = -0.0002\,S^2 - 0.043\,S$

To solve Eq. 3-4, all parameters are known except for the recovery ratio and the outlet temperature. According to the second assumption, the outlet temperature of the slurry solution is equal to the freezing temperature of the unfrozen concentrated brine. The freezing temperature of the brine is provided by the fourth equation in Table 3-1, which depends on the salinity of the concentrated brine. Therefore, it is necessary to calculate the salinity of the concentrated brine based on the known parameters. The salinity of the exiting unfrozen concentrated brine can be expressed as a function of the feed brine salinity, the recovery ratio, and the efficiency of the desalination process. In freeze desalination, efficiency is typically measured using a metric known as the desalination rate [87,116,144,145]. This rate is defined as the ratio of the mass of salt present in the rejected unfrozen concentrated brine to the mass of salt in the feed brine. The desalination rate reflects the system's ability to minimize salt carryover into the produced ice.

$$\eta = \frac{m_{s,\mathrm{cb}}}{m_{s,\mathrm{fb}}} = 1 - R\left(\frac{S_{\mathrm{ice}}}{S_{\mathrm{fb}}}\right) \qquad 3\text{-}6$$

where $m_{s,\mathrm{cb}}$ and $m_{s,\mathrm{fb}}$ are the mass of salt in the concentrated brine and feed brine, and S_{ice} and S_{fb} are the salinities of the melted produced ice and feed brine, respectively.

In this experimental study, the salinity of various solutions, including feed brine, concentrated brine, and produced ice, is measured using a TDS meter. Therefore, the salinity of a solution (S), defined as the mass of dissolved salts over the mass of the solution, needs to be converted to TDS. For solutions where all dissolved solids are salts, the relationship between salinity and TDS is given by $S_{\mathrm{b}} = \mathrm{TDS}_b/\rho_b$. Given that salts make up approximately 96% of the dissolved mass in this study, the same conversion can be applied. Consequently, the desalination rate in terms of TDS can be expressed as follows:

$$\eta = 1 - R\left(\frac{\rho_{\mathrm{fb}}}{\rho_{\mathrm{ice}}}\right)\left(\frac{\mathrm{TDS}_{\mathrm{ice}}}{\mathrm{TDS}_{\mathrm{fb}}}\right) \tag{3-7}$$

Using the first equation listed in Table 2-3, the density of the brine can be formulated based on its TDS.

$$\rho_b = 498.5 + \sqrt{498.5^2 + \mathrm{TDS}_{\mathrm{b}}} \tag{3-8}$$

The outlet temperature of the freezing chamber corresponds to the freezing temperature of the concentrated brine at the outlet, which depends on the salinity of the concentrated brine, denoted as S_{cb}. This salinity can be calculated based on the salinity of the feed brine, the desalination rate, and the recovery ratio, as follows:

$$S_{\mathrm{cb}} = \eta \frac{S_{\mathrm{fb}}}{1 - R} \tag{3-9}$$

The outlet temperature of the freezing chamber, (in °C), is determined by the salinity of the concentrated brine (expressed in grams of salt per kilogram of brine) using Eq. 3-9 and the fourth equation listed in Table 3-1. By incorporating the outlet temperature as a function of the inlet brine salinity (S_{cb}), along with the recovery ratio (R) and the desalination rate (η) into Eq. 3-4, the resulting formula contains two unknown variables: the recovery ratio and the desalination rate. The desalination rate in the freeze desalination process is largely influenced by the effectiveness of brine rejection during the centrifugal separation process. Experimental results indicate that the desalination rate typically ranges from 0.9 to 0.99. Consequently, for this theoretical analysis, an average desalination rate of 0.95 is assumed. It should be noted that further analysis of variations in the desalination rate, from 0.9 to 0.99, reveals that these changes have a negligible impact on the recovery ratio.

The heat gain during the freezing process was measured through experimental methods. To accomplish this, the ICL was circulated through the system at the same flow rate and temperature as it would be with brine injection, but without injecting any brine. Once a steady state was achieved, the temperature differential of the ICL across the freezing chamber was recorded. This temperature difference was then utilized to calculate the heat gain:

$$\dot{Q}_{\mathrm{gain}} = \dot{m}_{\mathrm{ICL}} c_{\mathrm{ICL}} \left(T_{\mathrm{ICL,out}} - T_{\mathrm{ICL}}\right) \tag{3-10}$$

where $T_{\mathrm{ICL,out}}$ represents the temperature of the ICL as it exits the freezing chamber without brine injection. After conducting multiple measurements, it was determined that the average temperature increase of the ICL was approximately 1°C at an ICL flow rate of 5 kg/min. Using the measured ICL temperature rise, the heat gain was calculated to be between 140 W to 160 W. Once the heat gain is calculated, for any specified values of T_{ICL}, $\dot{m}_{\mathrm{ICL}}$, T_{fb}, $\dot{m}_{\mathrm{fb}}$, and S_{fb}, the recovery ratio (R), the outlet temperature, T_{out}, and the salinity of the concentrated brine, S_{cb}, can be calculated using Eqs. 3-4, 3-5, 3-9, and those outlined in Table 3-1.

4. Freeze Desalination Experimental and Theoretical Results[3]

The primary objective of freeze desalination is to produce a low-salinity water stream from high-salinity feed brine while achieving a reasonable recovery ratio. The achievement of this process is influenced by several key parameters, including the cooling temperature, the salinity of the feed brine, and the effectiveness of the ice-brine separation. This chapter explores how these factors impact the desalination process, starting with an analysis of cooling temperature effects on the recovery ratio and the quality of the ice produced. Subsequently, the impact of feed brine salinity on the process is examined, followed by an investigation into the role of centrifugation time in enhancing separation efficiency. It is important to note that throughout the experiments, the outlet temperature of the freezing chamber consistently remained above the critical temperature necessary for salt-hydrate formation. As a result, no salt-hydrates were produced, and ice was the only solid substance in the system.

4.1. Effect of Cooling Temperature

One critical determining factor for both the recovery ratio and the quality of the treated water in freeze desalination is the cooling temperature. The cooling temperature refers to the steady-state temperature of the freezing chamber. More specifically, it represents the steady-state temperature of the mixture (ICL, concentrated brine, and ice) at the outlet of the freezing chamber. This section explores how various cooling temperatures influence the recovery ratio and produced ice salinity, using a consistent feed brine TDS of 70,000 ppm and an ICL mass flow rate of 5 kg/min. Both the feed brine flow rate and its temperature were maintained at 0.13 kg/min and 20°C, respectively.

[3] The content of this chapter is an extension of a published paper by the author. The paper contains results of research which was solely conducted as partial fulfillment for the PhD requirement. Materials presented in the paper have not been submitted for a course or extra credit.

Four distinct cooling temperatures were evaluated: -10°C, -14°C, -17°C, and -20°C. These temperatures were precisely controlled by adjusting the inlet ICL temperatures, which in turn were regulated by modifying the refrigeration unit's cooling power. To ensure consistent conditions, the ICL flow and brine injections were kept steady, and the cooling power was fine-tuned until the target temperature at the freezing chamber outlet was reached. After the freezing process, the collected ice underwent a 12-minute centrifugation process in a spin-dryer to remove entrapped unfrozen concentrated brine. To prevent melting during this process, the spin-dryer was housed within a freezer set at approximately -10°C. Following centrifugation, the ice was extracted, melted, and analyzed for mass and TDS. A representative sample of the drained ice is displayed in Fig. 4-1.

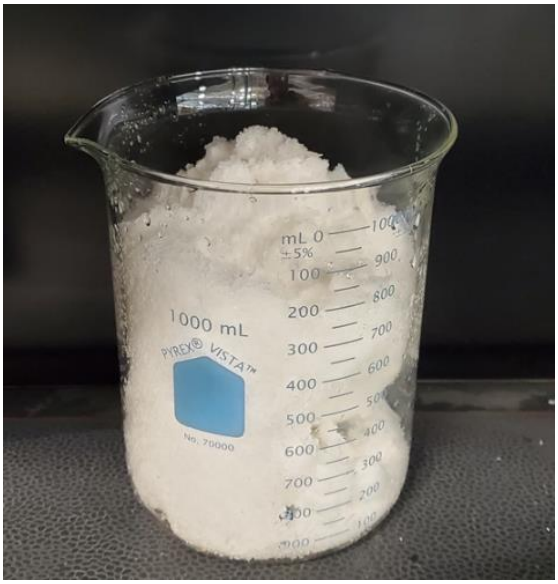

Fig. 4-1 Produced ice after centrifugal brine draining.

Figure 4-2 illustrates the impact of cooling temperature on the recovery ratio and TDS of the melted ice (treated water) following a centrifugation time of 12 minutes. As anticipated, lower cooling temperatures lead to higher recovery ratios. Specifically, the TDS of the treated water (TDS_{tw})

measured 3300, 2700, 2200, and 1800 ppm at cooling temperatures of -20°C, -17°C, -14°C, and -10°C, respectively. The reduction in TDS at relatively higher cooling temperatures is linked to slower ice crystallization rates, which allow more time for the ice crystals to expel the brine, resulting in purer ice. In contrast, at lower cooling temperatures, the crystallization process accelerates, capturing more brine within the ice structure. This inverse relationship between the TDS of treated water in freeze desalination systems and the temperature of the freezing process is a well-documented phenomenon, reported by several studies [95,118,120,146]. Another factor contributing to lower TDS at higher cooling temperatures could be the reduced mass ratio of ice to unfrozen brine. Less ice formation at higher temperatures means a smaller increase in the concentration of the remaining brine, leading to less saline unfrozen brine being trapped within the ice. This observation implies a tradeoff in freeze desalination systems: while lower temperatures improve recovery ratios, they can also lead to higher TDS levels in the treated water due to increased brine entrapment.

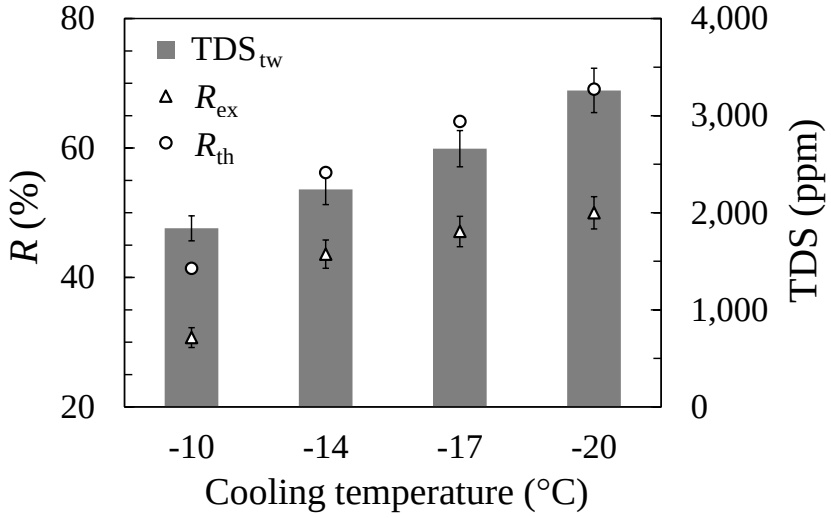

Fig. 4-2 Theoretical (R_{th}) and experimental (R_{ex}) recovery ratios, along with the corresponding TDS of the treated water (TDS_{tw}), for feed brine with a TDS of 70,000 ppm and various cooling temperatures. The error bars are the overall measurement uncertainty.

Figure 4-2 also displays the recovery ratios determined through theoretical calculations at various cooling temperatures. It is apparent from the data that the theoretical predictions overestimate the recovery ratios when compared to the experimental outcomes. This discrepancy may arise from factors such as partial melting of ice within the filter bag, as well as ice loss that occurs during transport to the spin-dryer device and throughout the centrifugation separation process.

4.2. Effect of Brine Salinity

The feed brine salinity is another critical factor that can significantly impact both the recovery ratio and the salinity of the treated water. It is generally anticipated that lower brine salinities will result in produced ice with reduced salinity. However, as will be demonstrated, the cooling temperature and recovery ratio can also significantly affect the salinity of the produced ice, often independent of the feed salinity. This section presents and compares the experimentally determined recovery ratios and treated water TDS for four different feed brine salinities: 15,000 ppm, 35,000 ppm, 70,000 ppm, and 100,000 ppm, all at a cooling temperature of -17°C. The flow rates for the ICL and feed brine were maintained at 5 kg/min and 0.13 kg/min, respectively, with the feed brine inlet temperature set at 20°C. The produced ice was separated from the concentrated brine through 12 minutes of centrifugation.

Figure 4-3 presents both experimental and theoretical results of recovery ratios and the TDS of treated water across various feed brine salinities. As anticipated, an increase in feed brine TDS led to a decrease in the recovery ratio. Interestingly, however, the salinity of the ice produced was lower at higher feed brine TDS levels. This initially paradoxical outcome can be explained by differences in the freezing rate. With a constant cooling temperature and feed brine flow rate, a lower salinity in the feed brine tends to produce more ice in the same period, resulting in a faster ice crystallization

rate. This rapid crystallization tends to trap more concentrated brine within the ice crystals. These micro pockets of brine are difficult to eliminate through centrifugal draining and can significantly elevate the TDS of the treated water when the ice melts. The correlation between rapid freezing rates and higher salinity in treated water has been documented in prior research [87,104,145], supporting these observations.

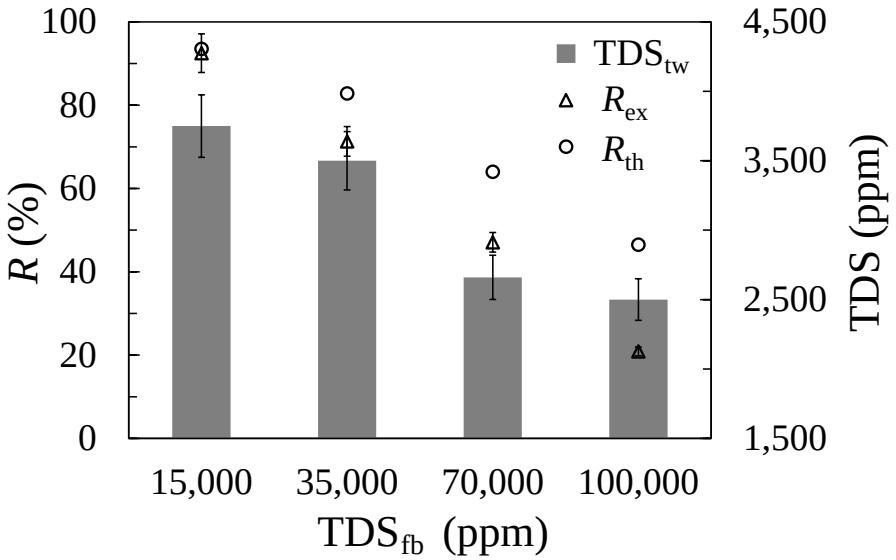

Fig. 4-3 Theoretical (R_{th}) and experimental (R_{ex}) recovery ratios, along with the corresponding TDS of the treated water (TDS_{tw}), for a cooling temperature of -17°C across a range of feed brine salinities (TDS_{fb}). The error bars indicate the overall uncertainty of the measurements.

Both experimental and theoretical recovery ratios are found to decrease with an increase in feed brine TDS. As shown in Fig. 4-3, at lower feed TDS levels, the experimental recovery ratios align more closely with the theoretical predictions. However, as the feed salinity increases, the divergence between experimental and theoretical results becomes more pronounced. This discrepancy at higher feed brine TDS levels can be explained by the increased likelihood of unintended ice melting

during the transport and centrifugation processes. Additionally, with higher brine TDS, the brine trapped within the ice contains higher concentrations of dissolved solids. Consequently, ice near these high-salinity brine pockets is more prone to melting during centrifugation, further impacting the recovery ratios. Furthermore, the prolonged freezing process for feed brine with higher salinity could be another contributing factor. When brine is injected into the cold ICL, the freezing process begins almost instantly. However, the freezing continues as the brine moves through the freezing chamber. As more ice is created, the salinity of the remaining brine increases, and lower temperatures are needed to maintain the freezing process. Consequently, higher salinity brine takes longer to achieve the freezing limit, reducing the likelihood of reaching steady-state at the outlet of the freezing chamber. Therefore, the assumption of equal temperatures for all components at the outlet is not met, resulting in the ice having a higher temperature than the ICL in experiments. This leads to a lower recovery ratio in the experimental tests at higher feed brine salinities.

Table 4-2 presents the estimated values for the sensible and latent heat components of the brine freezing, the heat gain during the freezing process, and their corresponding percentages for various feed brine salinities and cooling temperature of -17°C.

Table 4-1 The estimated values of sensible and latent heat components of the brine freezing and the heat gain during the freezing process for multiple feed brine salinities

Feed brine TDS (ppm)	**Sensible heat component (W)**	**Latent heat component (W)**	**Heat gain component (W)**	**Total cooling energy (W)**
15,000	258 (24%)	667 (62%)	~150 (14%)	1075
35,000	267 (27%)	572 (58%)	~150 (15%)	989
70,000	277 (31%)	460 (52%)	~150 (17%)	887
100,000	290 (39%)	305 (41%)	~150 (20%)	745

Figure 4-4 presents the experimentally determined desalination rate, η, and corresponding recovery ratios (R_{ex}) across a range of feed salinities at a constant cooling temperature of -17°C. The data indicate that at this fixed cooling temperature, an increase in feed brine salinity enhances the desalination rate while simultaneously reducing the recovery ratio.

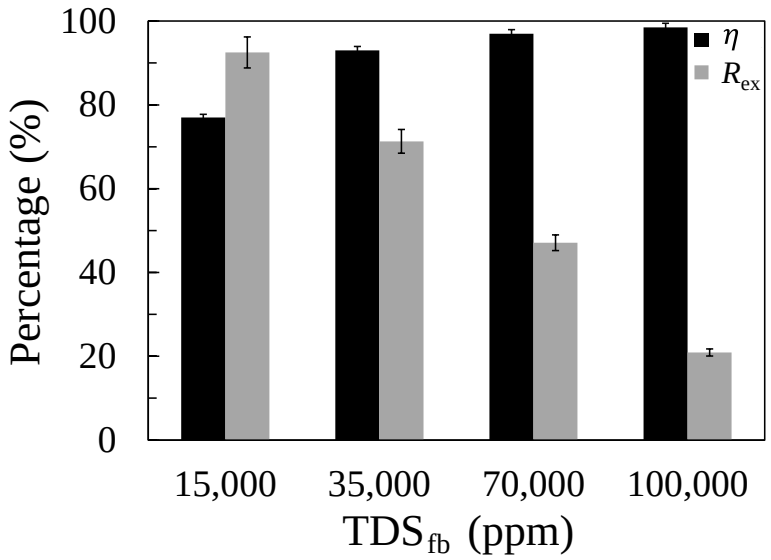

Fig. 4-4 Experimentally measured desalination rate (η) and recovery ratio (R_{ex}) across various feed brine salinities (TDS_{fb}) at a cooling temperature of -17°C. Error bars illustrate the overall measurement uncertainty.

4.3. Effect of Centrifugal Brine Removal Duration

As previously mentioned, the collected ice incorporates brine that must be efficiently extracted before melting. Some of this unfrozen brine adheres to the surface of the ice crystals, while the rest remains entrapped within them. To facilitate brine removal, a centrifugal method was utilized, with varying durations of centrifugation (t_{cent}) ranging from 4 to 16 minutes explored to assess their impact on the recovery ratio and the quality of the treated water. Table 4-3 details the outcomes in terms of recovery ratio, TDS of the treated water, and the desalination rate for these various centrifugation times, using a feed brine TDS of 70,000 ppm at a cooling temperature of -17°C. The data suggest a high initial presence of brine within the ice, as indicated by the substantial desalination rate. Extending the centrifugation time beyond a certain point, however, did not significantly alter the TDS. It is noted that the effectiveness of the centrifugal separation process

could be enhanced by employing devices with higher rotational speeds, which not only shortens the separation duration but may also reduce the energy consumption of the process.

Table 4-2 The experimental recovery ratio (R_{ex}), TDS of the treated water (TDS_{tw}), and desalination rate (η) for a feed brine TDS of 70,000 ppm and cooling temperature of -17°C for various centrifugation durations (t_{cent}).

t_{cent} (minutes)	R_{ex} (%)	TDS_{tw}(ppm)	η (%)
4	53.1	7,370	93.4
8	48.5	4,650	96.3
12	47.1	2,660	97.9
16	45.8	2,100	98.6

Figure 4-5 illustrates how the recovery ratio and TDS of the treated water change with varying centrifugation durations. It is clear from the data that longer centrifugation periods lead to lower TDS in the treated water and smaller recovery ratios. Extending the centrifugation time enhances brine removal from the ice, which has dual effects: it reduces the amount of unfrozen brine within the ice, thereby decreasing the total mass of ice recovered from the spin-dryer and resulting in a lower recovery ratio. Simultaneously, it improves the TDS of the treated water as there is less unfrozen brine remaining in the ice. The desalination rates for centrifugation durations of 4, 8, 12, and 16 minutes are approximately 93%, 96%, 98%, and 99%, respectively. Notably, the desalination rate increases by about 3% when extending centrifugation from 4 to 8 minutes, but only by about 1% when extending it from 12 to 16 minutes. This diminishing return is attributed to the increasing difficulty of expelling brine from "drier" ice. As a result, for centrifugation times exceeding roughly 16 minutes, further

brine rejection is negligible, and only minor changes in the recovery ratio and TDS of the treated water are observed.

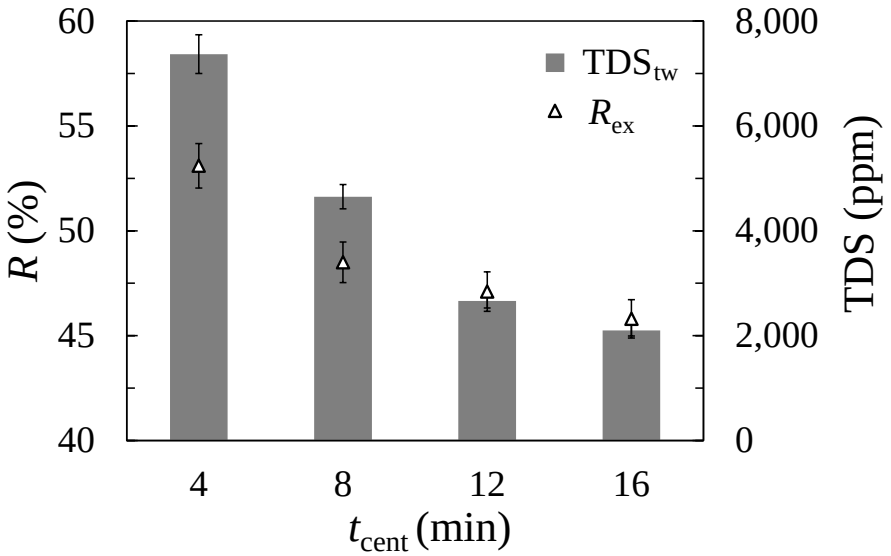

Fig. 4-5 Experimental recovery ratio (R_{ex}) and the corresponding TDS of the treated water (TDS_{tw}) for a feed brine with TDS_{fb} of 70,000 ppm at a cooling temperature of -17°C. Error bars indicate the overall measurement uncertainty.

4.4. Concluding Remarks

In this research, a novel freeze desalination system utilizing an intermediate cooling liquid was developed and evaluated for processing high-salinity brine. Various experiments were carried out to determine the recovery ratio and the total dissolved solids of the treated water across a range of cooling temperatures, feed brine salinities, and centrifugation separation durations. The key findings from these experiments are summarized as follows:

- The experimental findings indicate that with a fixed feed brine salinity, lowering the cooling temperature led to an increase in the recovery ratio. Conversely, the TDS of the

treated water was higher at these lower cooling temperatures. This phenomenon is attributed to the faster crystallization rates at reduced temperatures, which results in less time for salt to be expelled, consequently trapping more salt within the ice crystals.

- The experimental results revealed that at a constant cooling temperature, ice production increased with lower salinity levels in the feed brine. Conversely, the salinity of the treated water decreased when the feed brine had higher salinity levels. This observation can also be explained by the more rapid crystallization occurring at lower TDS in the feed brine.
- Extended centrifugation durations enhanced the removal of unfrozen concentrated brine from the ice, thereby reducing the TDS of the treated water. However, this also led to a reduction in the recovery ratio due to the decreased mass of ice recovered. Beyond approximately 16 minutes, further increases in centrifugation time had minimal impact on both the recovery ratio and the salinity of the treated water.

Nomenclature

c	Specific heat capacity ($\mathrm{kJ/kg \cdot K}$)
EDX	Energy dispersive X-ray
FD	Freeze desalination
h_{sl}	Latent heat of fusion ($\mathrm{kJ/kg}$)
ICL	Intermediate cooling liquid
LNG	Liquid natural gas
MED	Multi-effect desalination
MSF	Multi-stage flash
$\dot{m}$	Mass flow rate ($\mathrm{kg/s}$)
PDMS	Polydimethylsiloxane
$\dot{Q}$	Heat transfer rate ($\mathrm{kJ/s}$)
R	Recovery ratio, $R = \frac{\dot{m}_{\mathrm{ice}}}{\dot{m}_{\mathrm{fb}}}$
RO	Reverse osmosis
S	Salinity ($\mathrm{g/kg}$), $S = \frac{m_s}{m_b}$
T	Temperature (℃)
TDS	Total dissolved solids (ppm)
t	Time (minutes)

VFD	Variable frequency drive
ρ	Density ($\mathrm{kg/m^3}$)
η	Desalination rate, $\eta = \frac{m_{s,\mathrm{cb}}}{m_{s,\mathrm{fb}}}$

Subscripts

avg	Average
b	Brine
cb	Concentrated brine
cent	Centrifugation
ex	Experimental
fb	Feed brine
frz	Freezing
s	Salt
th	Theoretical
tw	Treated water

5. Migration and Melting of Suspended Solid Particle in Poiseuille Flow[4]

In the preceding chapters, the experimental study of a novel freeze destination setup along with the theoretical modeling for predicting the ice production rate are explored in detail. As previously discussed, the freezing process in desalination consumes significantly less energy compared to evaporative thermal-based methods. However, it is still more energy-intensive than membrane-based methods such as reverse osmosis and forward osmosis, particularly for desalination of lower salinity brine. One strategy to improve the energy efficiency of freeze desalination systems involves recovering cooling energy of the generated ice. A significant amount of energy in the freeze desalination setup is dedicated to ice production through the latent heat of fusion. In the current study, the collected ice is melted at room temperature and the TDS and mass are measured. The cold energy recovery can be accomplished by circulating an ice-water slurry through a heat exchanger in order to absorb heat from the condensing refrigerant. Although this experimental study does not implement cold energy recovery from the produced ice, a computational simulation of the melting process is conducted. This simulation focuses on modeling the melting process itself, rather than exploring potential enhancements in cold energy recovery, which would require a detailed investigation in future studies.

In this chapter, the ice melting process is studied, using certain simplifying assumptions which will be detailed in the subsequent sections. The chapter begins by establishing the relevance of this study through a review of previous research on particle melting, both in ice melting simulations and other applicable fields. Following this, various solid-liquid simulation methods

[4] The content of this chapter is an extension of a published paper by the author. The paper contains results of research which was solely conducted as partial fulfillment for the PhD requirement. Materials presented in the paper have not been submitted for a course or extra credit.

are discussed, highlighting the specific approach utilized in this research. A comprehensive description of the problem under investigation is set to follow in the subsequent section. Finally, the mathematical model is presented, covering the governing equations, the numerical procedure, the independence studies, and the validation simulation.

5.1. Literature Review & State of the Art

The utilization of cold energy from the produced ice in the freeze desalination setup for cooling the condenser can be implemented in various configurations. One method involves pumping an ice slurry through a tube submerged in the water where the condenser is located. This slurry, containing both ice and water, facilitates easier pumping. One fundamental study involves investigating the melting of a single particle, which can later be expanded to include multiple particles and slurry solutions. Consequently, this simulation study focuses on examining the movement and melting of a single ice particle, modeled as a cylindrical particle undergoing melting. Beyond its use in ice melting simulations, this study offers fundamental insights into the dynamics of particle melting, extending its relevance to a variety of problems and configurations across different fields.

Previous studies on ice melting, covering both individual particles and slurry scenarios, have employed some simplifications, which are used in the current study. These include modeling the process in a two-dimensional space, using cylindrical ice particles, and assuming a constant temperature in the particle. The particle melting simulation problem also has broader applications in addressing similar phenomena across different contexts, which will be discussed in the following. This section presents simulations related to ice melting, followed by discussions of particle melting simulations applied to other applications.

Dierich et al. [147] investigated a single cylindrical ice particle melting as it is subjected to fluid flow employing an implicit fictitious boundary method. They studied the rising and melting of multiple ice particles, focusing on how the Reynolds number influences the particle's melting time. A finding from these simulations is that particle rotation induced by viscous torques can substantially reduce melting times, enhancing heat transfer efficiency. Additionally, three distinct flow regimes are identified during the particle's ascent: an acceleration regime due to gravity, a transitional phase, and a passive regime where the particles follow the flow without influencing it.

The study on the flow and heat transfer characteristics of ice slurry, specifically analyzing the melting dynamics of a spherical ice particle as it ascends in stationary water, is conducted by Guo et al. [148]. They utilized momentum equations to describe the particle's motion and developed an enthalpy-porosity model for flow and heat transfer. Their research focused on examining the effects of the supercool degree (the temperature difference between the ice's melting temperature and its initial temperature) and the superheat degree of water (the temperature difference between the water and the ice's melting temperature) on the behavior of a melting ice particle in a stationary liquid pool. The results indicate that the ice particle initially accelerates due to buoyancy, achieving a peak velocity before decelerating as it melts. They also discovered that a higher degree of water superheat significantly increases the melting rate and influences the particle's morphological transition from spherical to ellipsoid, and eventually to oval, while the supercool degree has a negligible impact on the particle’s motion and melting rate.

Suzuki et al. [149] employ the thermal immersed boundary–lattice Boltzmann method to model solid-liquid and solid-solid interactions in ice slurry flows using a simplified two-dimensional model. Their research demonstrates that smaller ice particles enhance cooling efficiency by elevating the Nusselt number along the channel walls. This enhancement is attributed

to the increased dispersion of smaller particles and proximity to the channel walls. Additionally, the findings show that an increase in flow velocity leads to a decrease in the Nusselt number, suggesting that higher flow rates cause particles to gather away from the channel walls, reducing cooling effectiveness. They expanded their research to a three-dimensional model and evaluated how the Reynolds number and the density ratio between the ice particles and the carrier fluid affect the cooling performance of ice slurry flows [150]. The results reveal an increase in the Nusselt number along the duct walls with higher Reynolds numbers, a finding that is in contrast with those obtained in two-dimensional simulations. Additionally, the study investigates the impact of varying density ratios, analyzing scenarios in which ice particles are either neutrally buoyant or slightly less dense than the carrier fluid. The findings demonstrate that lower density ratios cause the ice particles to migrate towards the top wall of the duct due to buoyancy forces, resulting in a heterogeneous flow that slightly enhances the Nusselt number, offering an improvement over the homogeneous flow condition.

As previously mentioned, particle melting holds relevance across numerous applications. A major example is the simulation of phase change material (PCM) particles melting within their own melt. PCMs are widely utilized in thermal energy storage [151,152] and temperature regulation systems [153,154] due to their high energy density and ability to transfer heat at nearly constant temperatures. They are incorporated into PCM slurries both as encapsulated and shell-less particles. Practical applications of PCM slurries span several industries and technologies, including impinging jet cooling [155], mini-channel heat sinks [156], battery thermal management [157], enhancement of heat exchanger efficiency [158], direct absorption solar collectors [159], thermal energy storage [160], and various metallurgical processes [161].

One of the earliest direct numerical simulations for analyzing the behavior of melting particles suspended in a liquid was conducted by Gan et al. [162] using a two-dimensional finite element method. This study focused on the sedimentation and melting of single and dual cylindrical particles within a vertical channel where there was no induced flow and the surrounding liquid remained stationary. The research calculated local deformation rates of the particles based on localized heat fluxes at the particle surface and predicted particle trajectories and melting rates across various initial positions. The findings highlighted that the sedimentation of melting particles is significantly affected by buoyancy-driven convection (natural convection) within the melt. The study characterized two distinct regimes of particle migration based on the Grashof number (Gr): in conditions where Gr is less than 900, particles descend along the channel centerline, whereas at Gr values greater than 900, particles tend to deviate towards the channel walls. Additionally, the study observed that higher Gr numbers generally result in slower melting rates, because the downward convection brings colder fluid into greater contact with the particle surface.

Shabgard et al. [163] developed an Arbitrary-Lagrangian-Eulerian (ALE) model to explore the sedimentation and melting of multiple cylindrical-shaped PCM particles within a vertical channel with heated walls. The model featured a deforming grid to accurately capture the motion and deformation of the PCM particles. To simplify the hydrodynamic calculations, the model assumed that the particle motion did not involve rotation. Their findings indicated that the wall Nusselt number, defined as the product of the wall heat flux and the hydraulic diameter of the channel, divided by the temperature difference between the wall and the fluid, exhibited an almost linear increase as the solid PCM volume fraction increased. Kaviani et al. [164] employed a two-dimensional ALE model to study the migration and melting of a single cylindrical particle in a pressure-driven flow between two vertical parallel plates. The findings indicate that as Gr

increases, the melting time decreases due to enhanced natural convection. Moreover, an increase in Gr triggers a transition in particle migration from monotonic to oscillatory regimes.

Although flows with suspended melting particles have a broad range of applications, the hydrodynamic and thermal interactions between a pressure-driven flow and a suspended melting particle remain largely unexplored. This study aims to conduct a direct numerical simulation to analyze the motion and melting of a neutrally buoyant particle suspended in its own melt within a plane Poiseuille flow. As previously noted, this setup is relevant not only to the melting of ice particles but also to other substances that melt in similar conditions. To keep the analysis applicable to a wide variety of scenarios, the density difference between the particle and the melt is disregarded, ensuring the particle's neutral buoyancy. Furthermore, the liquid phase is defined as the melt of the particle itself; for instance, in the case of an ice particle, the melt would be pure water instead of ICL. These simplifications enhance the model's versatility for application across numerous other settings and configurations.

A particle-resolved ALE model has been developed to analyze the flow and temperature fields within the fluid. This model uses the Navier-Stokes and energy equations to characterize the Eulerian phase of the fluid domain, while the motion of the particle is described using Newton's second law of motion, representing the Lagrangian phase. The dynamics of the fluid and the particle are interconnected through interfacial forces at the fluid-particle boundary. These forces are calculated by integrating the local shear and normal stresses at the interface, which are derived from the distributions of velocity gradients, pressure, and temperature gradients at the solid-liquid interface. This method of directly calculating interfacial forces and heat transfer rates distinguishes this particle-resolved approach apart from non-particle-resolved methods, which typically rely on empirical correlations for these calculations. The particle motion and deformation at each timestep

are determined from Newton's second law of motion and the interfacial energy balance, respectively. To manage the displacement of these grid nodes, the ALE method is utilized, allowing for the necessary deformation of control volumes and displacement of grid nodes.

The subsequent portions of this section are organized as follows. First, various interface tracking methods are introduced, with a focus on the ALE method utilized in this research. In the next section, the physical problem addressed by the study is outlined accompanied by the computational approach explanation, detailing the governing equations, boundary and initial conditions, and the numerical techniques implemented to solve these equations. Additionally, this section discusses the validation of the computational model.

5.2. Interface Tracking Methods

Interfaces or internal boundaries are prevalent in various applications, such as multiphase flows, solidification, and melting phenomena. Simulating fluid flow problems, particularly those involving fluid-fluid and fluid-solid interfaces, presents several challenges. One major difficulty is the time-dependent nature of the position and shape of the interfaces, which may involve heat and mass transfer during phase change processes. Additionally, these interfaces can undergo significant deformations, impacting the surrounding flow and thermal fields. Another challenge lies in modeling discontinuities in thermophysical properties across the interface, especially large density variations. These moving boundaries play a critical role in the system, and their precise representation significantly affects the solution of the problem. Addressing the computational treatment of a moving and deforming interface involves several key aspects, such as representing the interface on a finite grid, tracking the time evolution of the interface, and specifying boundary conditions at the interface. Numerical solutions for interfaces can generally be achieved using

Eulerian (fixed) or Lagrangian (moving) grids, each with its own set of advantages and disadvantages. In the following sections, various interface capturing (tracking) techniques are described briefly and a detailed explanation of the method selected for the present work is explained.

5.2.1. Lagrangian Method

The Lagrangian method is a numerical approach that excels in tracking the movement of fluid particles and interfaces by directly following the trajectory of individual fluid elements over time. In this method, the computational mesh moves and deforms with the fluid, providing a detailed and accurate prediction of the interface evolution. By continuously updating the positions of individual fluid particles, the Lagrangian method ensures a precise representation of the interface's shape and position at all times. Despite its accuracy in predicting interface evolution, the Lagrangian method faces challenges when dealing with large deformations. As particles move and the mesh deforms, highly skewed meshes can arise, complicating the maintenance of numerical accuracy and stability. Additionally, tracking a large number of particles can be computationally intensive, especially in three-dimensional simulations or when high resolution is required, leading to increased computational costs and longer simulation times [165].

5.2.2. Volume of Fluid (VOF) Method

The VOF method is a widely used Eulerian technique for predicting multiphase fluid flow problems. This method solves the Navier-Stokes equations on a fixed grid, combined with a transient advection equation that governs the evolution of the interface function, marking the position of the interface between different phases. In the VOF method, it is assumed that the phases

do not interpenetrate. For each phase, a phase indicator function is introduced, which represents the volume fraction of that phase within a computational cell. The sum of the volume fractions of all phases in any given computational cell is always unity. In practice, when the volume fraction of a particular phase lies between 0 and 1 within a computational cell, that cell is considered an interfacial cell, containing the boundary between different phases. One of the challenges in the VOF method is maintaining sharp interface resolution, as numerical diffusion can lead to distorted interfaces and inaccurate solutions. Moreover, the VOF method may require specialized interpolation schemes and advanced numerical techniques to minimize diffusion and improve accuracy, which can increase the complexity of the simulation [166].

5.2.3. Level-Set Method

In the level-set method, the interface is represented implicitly by a higher-dimensional function, typically referred to as the level-set function. The interface is defined as the zero-level-set of this continuous function, which allows for a smooth and flexible representation of complex shapes and topological changes, such as merging and splitting of interfaces, without requiring explicit parameterization. One of the key advantages of the level-set method is its ability to handle complex interface dynamics. The method evolves the level-set function according to a partial differential equation, which governs the motion of the interface based on the underlying physical forces. This implicit representation is highly advantageous in simulations involving significant deformations. Additionally, the level-set method can incorporate effects such as surface tension, curvature, and contact lines. However, maintaining a precise and accurate interface representation requires careful numerical treatment, especially to prevent issues like numerical diffusion, which can cause the interface to become diffused or blurred over time. Furthermore, the method can be computationally

intensive, as it involves solving partial differential equations on a fixed grid with high resolution [167].

5.2.4. Arbitrary Lagrangian-Eulerian (ALE) Method

Due to limitations inherent in using either the Lagrangian or Eulerian methods, the Arbitrary Lagrangian-Eulerian (ALE) method was developed, combining the strengths of both approaches. This method is particularly popular for handling fluid flows with moving boundaries and interfaces. The ALE technique dynamically adjusts the computational grid to track and adapt to changes in the fluid domain's shape, caused by the movement or deformation of interfaces. This adjustment is managed through a mesh update process that involves moving the grid nodes as needed and remeshing to preserve the quality of computational elements while minimizing the frequency of remeshing. A significant advantage of the ALE method is its ability to precisely impose boundary conditions, as the moving boundary aligns exactly with a control surface of the computational mesh. The ALE approach offers flexibility in how the computational nodes are moved—similar to the Lagrangian method—or fixed, similar to the Eulerian grid. Additionally, nodes can move arbitrarily to continuously adjust the zoning, which is crucial for handling severe mesh deformations while preserving a consistent and effective mesh topology at the interface. The schematic of the mesh motion in Lagrangian, Eulerian, and ALE frameworks are shown in Fig. 5-1.

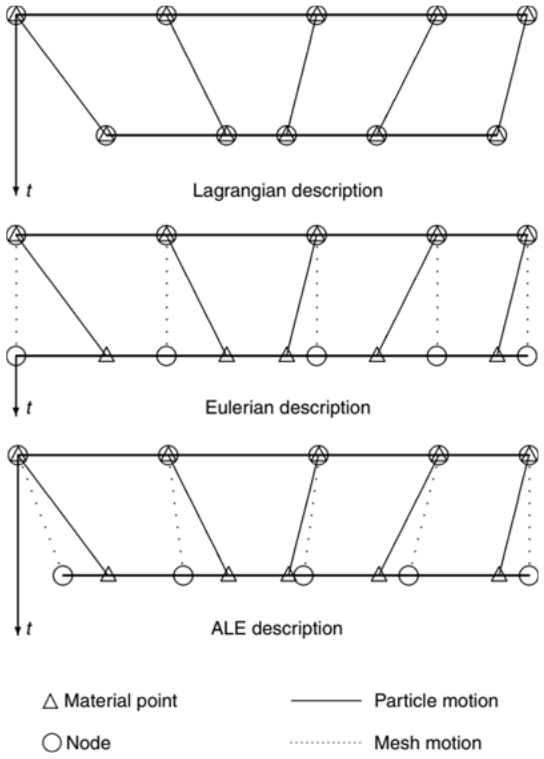

Fig. 5-1 Schematic of Lagrangian, Eulerian, and ALE mesh motion [168]

In this study, the ALE method is used due to its superior capabilities and features that are not available in fixed-grid methods. The ALE method is implemented in ANSYS Fluent through the "Dynamic Mesh Model" feature, which is designed to handle simulations with moving boundaries where the shape of the computational domain changes over time due to the movement of these boundaries. The dynamic mesh model utilizes three primary techniques: smoothing, layering, and remeshing [169]. These techniques can be combined to address complex moving mesh challenges, accommodating both rigid and deformable boundary motions. Mesh update methods are used to adjust the computational nodes at each time step according to the new boundary positions, making the mesh solutions inherently transient. To facilitate this process, several user-defined functions (UDFs) have been developed in this work to accurately describe the motion of the moving zones.

5.3. Problem Description

The two-dimensional domain utilized to investigate the migration of a neutrally buoyant melting particle in pressure-driven flow is depicted in Fig. 5-2. This domain features a single cylindrical particle with an initial diameter D, positioned between two infinitely wide horizontal parallel plates. The channel has a wall spacing of $W = 4D$ in the y-direction and a length of $L = 20D$ in the x-direction. The center of mass of the particle is fixed at the horizontal center of the computational domain along the x-axis, while various values are considered for the initial lateral location of the center of mass, y_0. A periodic boundary condition is applied at both the inlet and outlet of the channel, with a constant pressure gradient ($\partial p/\partial x = (p_i - p_o)/L$) in the x-direction, where p_i is the inlet pressure and p_o is the outlet pressure. The pressure gradient was maintained below a certain value to ensure the laminar flow within the channel. The condition corresponding to the laminar flow will be detailed in the following sections. The mathematical formulation of the periodic boundary condition is as follows:

$$\mathbf{V}|_{x=0} = \mathbf{V}|_{x=L} \tag{5-1}$$

$$T|_{x=0} = T|_{x=L} \tag{5-2}$$

where $\mathbf{V}$ is the velocity vector, $x = 0$ denotes the channel inlet and $x = L$ denotes the channel, and T is the fluid temperature. The particle's surface is maintained at a constant melting temperature, T_m, while the walls are kept at constant temperatures T_h, which are higher than T_m. No-slip boundary conditions are enforced at the walls and the interface between the particle and the fluid.

An initial velocity of zero is applied throughout the entire domain, which is filled with liquid at the initial temperature T_h. The temperature difference between the relatively hot fluid in the channel and the solid-liquid interface at the particle surface drives both heat transfer and the associated melting process. At the start of the simulation, the particle is at rest but begins to move due to its interaction with the flow. To reduce computational cost, the frame of reference is moved in the x-direction with a velocity equal to the axial velocity of the particle at each time step. The particle's motion in the y-direction is accommodated by deforming the computational grid. The particle's location within the domain is updated based on its relative translational velocity. Since the frame of reference moves at the same velocity as the particle in the x-direction, the relative velocity of the particle in the x-direction is always zero. Conversely, the relative velocity of the particle in the y-direction corresponds to its absolute velocity in the y-direction.

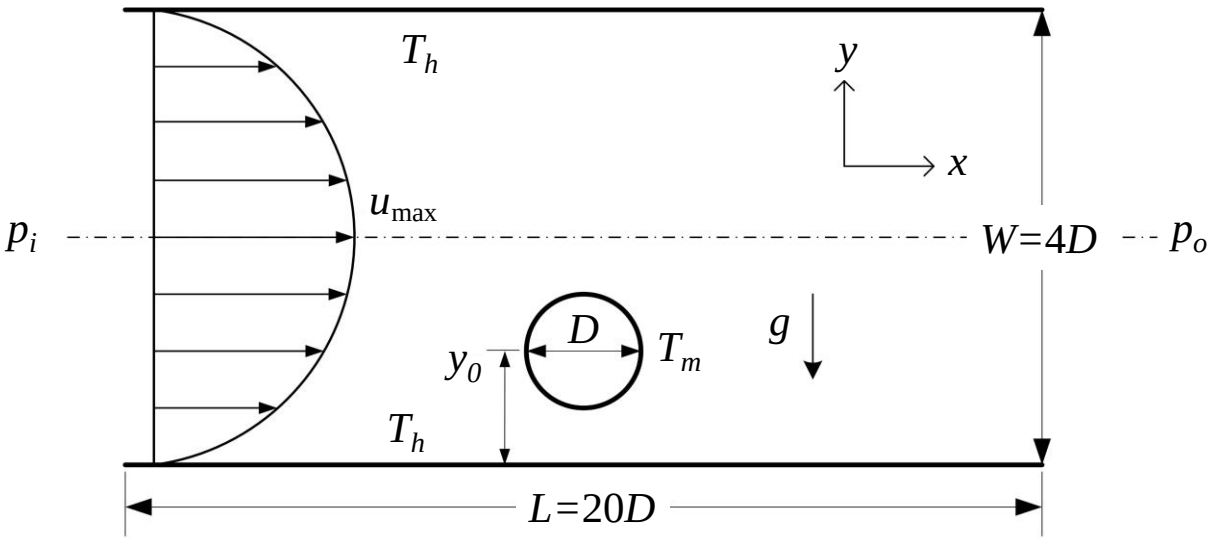

Fig. 5-2 Schematic representation of the domain for a neutrally buoyant melting particle migrating in a planar Poiseuille flow.

5.4. Mathematical Model

Within the ALE framework, the dynamics of fluid flow and heat transfer in the fluid phase are analyzed by solving the continuity, Navier-Stokes, and energy equations. Concurrently, the motion of the solid particle is predicted through the use of Newton's second law. The interactions between the fluid flow and the particle motion are coupled in a two-way manner: the fluid exerts pressure and viscous forces on the particle, and the particle influences the flow dynamics correspondingly [170]. Several key assumptions are employed for the development of this computational model: (*i*) the densities of the solid and liquid phases are identical at the melting temperature (T_m); (*ii*) the liquid is treated as an incompressible laminar Newtonian fluid, with constant thermophysical properties; and (*iii*) the melting of the particle occurs at a constant temperature T_m, which simplifies the modeling of phase change dynamics, (*iv*) the natural convection effect in the momentum equation is accounted for using the Boussinesq approximation, (*v*) the effect of viscous dissipation and radiation heat transfer are neglected. Given these assumptions, the equation for mass conservation is defined as follows:

$$\rho \boldsymbol{\nabla} \cdot \mathbf{V} + \dot{S}_{\text{mass}} = 0 \qquad \text{5-3}$$

In this equation, ρ represents the density of the liquid phase and $\dot{S}_{\text{mass}}$ is the volumetric mass source term, which accounts for the mass added to the continuous phase as a result of the particle melting and transitioning to the liquid phase. The momentum conservation equation, which governs the behavior of the fluid flow within the domain, can be expressed in its general form as follows:

$$\rho \frac{D\mathbf{V}}{Dt} = \rho \boldsymbol{f} + \boldsymbol{\nabla}.\sigma \tag{5-4}$$

In this formulation, $\boldsymbol{f}$ represents the body force per unit mass exerted on the fluid, and σ denotes the stress tensor. For Newtonian fluids, the stress tensor is particularly defined as follows:

$$\sigma = -p\mathbf{I} + \mu[\,\boldsymbol{\nabla}\mathbf{V} + (\boldsymbol{\nabla}\mathbf{V})^T] \tag{5-5}$$

where p represents the pressure and μ signifies the fluid's viscosity. The material derivative of the velocity, which captures both the temporal and spatial changes in velocity can be expressed as follows:

$$\frac{D\mathbf{V}}{Dt} = \frac{\partial \mathbf{V}}{\partial t} + (\mathbf{V}.\boldsymbol{\nabla})\mathbf{V} \tag{5-6}$$

In the ALE framework, the material time derivative of the velocity at a specific point $\mathbf{X}$ within the fluid domain and at a given time can be represented as [171]:

$$\frac{D}{Dt}\mathbf{V}(\mathbf{X}, t) = \frac{\delta \mathbf{V}}{\delta t} + [(\mathbf{V} - \mathbf{V}_{\text{mesh}}).\boldsymbol{\nabla}]\mathbf{V} \tag{5-7}$$

where $\mathbf{V}_{\text{mesh}}$ denotes the velocity of the mesh and $\delta\mathbf{V}/\delta t$ represents the referential time derivative. This derivative is defined as follows:

$$\frac{\delta}{\delta t}\mathbf{V}(\mathbf{X},t) = \left.\frac{\partial \mathbf{V}}{\partial t}\right|_{\text{ref}} \quad \text{5-8}$$

If the referential domain aligns with the spatial domain at the current time, such that the mesh velocity $\mathbf{V}_{\text{mesh}}$ is zero, the referential time derivative simplifies to the Eulerian time derivative. This scenario implies that there is no movement of the mesh relative to the spatial coordinates. Conversely, if the mesh velocity equals the velocity of the material particle, $\mathbf{V}_{\text{mesh}} = \mathbf{V}$, the referential time derivative transforms into the Lagrangian time derivative, capturing the viewpoint of an observer moving with the particle. Generally, the mesh velocity is not uniformly specified across the entire domain but is typically constrained at its boundaries to accommodate the movements of both the particle and the surrounding flow geometry. Within the interior of the domain, however, the mesh velocity can be largely arbitrary, providing flexibility in how the mesh adapts to the flow and the evolving boundaries of the simulation.

To effectively model natural convection within the fluid, the density is treated as a linear function of temperature in the momentum equation, represented by $\rho[1-\beta(T-T_0)]$. Here, T_0 stands as the reference temperature, ρ denotes the density of the liquid at T_0, β is the thermal expansion coefficient of the fluid, and T signifies the variable temperature within the fluid. For this model, the initial fluid temperature is set as the reference temperature, $T_0 = T_h$. By employing the Boussinesq approximation, the model simplifies the treatment of density variations by considering them solely in the buoyancy term of the momentum equation. This approach effectively captures the impact of temperature-driven density changes on the fluid dynamics without complicating the entire fluid density profile. As a result, the body force term in the

momentum equation, which primarily accounts for the effects of buoyancy due to temperature differences, can be expressed as follows:

$$\boldsymbol{f} = [1 - \beta(T - T_0)]\mathbf{g} \tag{5-9}$$

where $\mathbf{g}$ represents the gravity vector. The final form of the momentum conservation equation within the ALE framework can be expressed as follows:

$$\rho\left[\left.\frac{\partial \mathbf{V}}{\partial t}\right|_{\text{ref}} + \left((\mathbf{V} - \mathbf{V}_{\text{mesh}}) \cdot \boldsymbol{\nabla}\right)\mathbf{V}\right] = -\boldsymbol{\nabla} p + \mu\, \nabla^2 \mathbf{V} + \rho[1 - \beta(T - T_0)]\mathbf{g} - \rho \frac{\partial \mathbf{V}_{\text{frame}}}{\partial t} \tag{5-10}$$

In Eq. 5-10, the term $\rho \partial \mathbf{V}_{\text{frame}}/\partial t$ represents the linear acceleration of the reference frame [172]. This term captures the acceleration due to the movement of the reference frame along with the particle in the x-direction.

To better understand the direction of each component in the momentum conservation equation, Eq. 5-10 is rewritten for the x and y directions. In the *x*-direction (axial direction), the gravity term is absent because gravity acts in the *y*-direction. Therefore, the momentum conservation equation in the *x*-direction is as follows:

$$\rho\left[\left.\frac{\partial u}{\partial t}\right|_{\text{ref}} + (u - u_{\text{mesh}})\frac{\partial u}{\partial x} + (v - v_{\text{mesh}})\frac{\partial u}{\partial y}\right] = -\frac{\partial p}{\partial x} + \mu\left(\frac{\partial^2 u}{\partial x^2} + \frac{\partial^2 u}{\partial y^2}\right) - \rho \frac{\partial u_{\text{frame}}}{\partial t} \tag{5-11}$$

where *u* and *v* are the velocity components in the *x* and *y* directions, respectively. In the y-direction (lateral direction), the frame velocity is zero since the frame moves axially at a velocity equal to

the particle velocity. Consequently, the momentum conservation equation in the *y*-direction is as follows:

$$\rho\left[\left.\frac{\partial v}{\partial t}\right|_{\text{ref}}+(u-u_{\text{mesh}})\frac{\partial v}{\partial x}+(v-v_{\text{mesh}})\frac{\partial v}{\partial y}\right]=-\frac{\partial p}{\partial y}+\mu\left(\frac{\partial^2 v}{\partial x^2}+\frac{\partial^2 v}{\partial y^2}\right)-\rho[1-\beta(T-T_0)]\text{g} \qquad 5\text{-}12$$

The conservation of energy within the liquid phase under the ALE framework can be described as follows:

$$\rho c\left[\frac{\partial T}{\partial t}+(u-u_{\text{mesh}})\frac{\partial T}{\partial x}+(v-v_{\text{mesh}})\frac{\partial T}{\partial y}\right]=k\left(\frac{\partial^2 T}{\partial x^2}+\frac{\partial^2 T}{\partial y^2}\right) \qquad 5\text{-}13$$

where and c and k are the fluid specific heat and thermal conductivity, respectively. In the energy conservation equation, the radiation heat transfer and viscous dissipation terms are neglected.

The movement and deformation of the particle induce corresponding deformations in the cells within the fluid domain. As a result, the fluid cells surrounding the particle must be relocated and reshaped to accommodate these changes. To facilitate this, ANSYS Fluent's dynamic mesh model is utilized to manage the mesh motion and deformation in the vicinity of the particle. This model automatically updates the cells at each time step, taking into account the new position of the particle surface (the solid-liquid interface). Furthermore, the conservation equations for a general scalar quantity, denoted as ϕ, within an arbitrary control volume V_{CV} that has a moving boundary, are formulated in integral form as follows [169]:

$$\frac{d}{dt}\int_{V_{\mathrm{CV}}} \rho\phi dV_{\mathrm{CV}} + \int_S \rho\phi(\mathbf{V}-\mathbf{V}_{\mathrm{mesh}})\cdot d\mathbf{S} = \int_S \Gamma\nabla\phi\cdot d\mathbf{S} + \int_{V_{\mathrm{CV}}} S_\phi dV_{\mathrm{CV}} \quad 5\text{-}14$$

where Γ is the diffusion coefficient and S_ϕ is the source term.

The motion of the solid particle is governed by two fundamental principles within the Lagrangian framework. Newton's second law governs the translational motion of the particle, and the rotational motion of the particle is described by the Euler equation.

$$\frac{d(m_p\mathbf{V}_p)}{dt} = m_p\frac{d\mathbf{V}_p}{dt} + \mathbf{V}_p\frac{dm_p}{dt} = \mathbf{F} \quad 5\text{-}15$$

$$\frac{d(I_p\boldsymbol{\omega}_p)}{dt} = I_p\frac{d\boldsymbol{\omega}_p}{dt} + \boldsymbol{\omega}_p\frac{dI_p}{dt} = \mathbf{M} \quad 5\text{-}16$$

In the described equations, m_p represents the mass of the particle, which varies with time, and I_p denotes the moment of inertia, which is also a time-dependent quantity. $\mathbf{V}_p$ and $\boldsymbol{\omega}_p$ indicate the particle's absolute translational and rotational velocities, respectively. For a neutrally buoyant solid particle, the total force **F** acting on the particle includes surface forces, which arise from interactions with the surrounding fluid. These surface forces consist primarily of pressure forces, which are distributed over the particle's surface depending on the fluid's pressure field, and friction forces, which result from the viscosity of the fluid opposing the particle's movement. The term **M** is the moment of the total force.

The melting process occurs relatively slowly as compared to the rate of change of the linear and angular velocities. As such, the melting process can be considered quasi steady-state and the

dm_p/dt and dI_p/dt terms in the above equations can be neglected. The simplified Newton's second law and Euler's equations are:

$$m_p \frac{d\mathbf{V}_p}{dt} = \mathbf{F} \tag{5-17}$$

$$I_p \frac{d\boldsymbol{\omega}_p}{dt} = \mathbf{M} \tag{5-18}$$

The sum of net forces acting on the particle is as follows:

$$\mathbf{F} = \oint_S [-p\mathbf{I} + \mu(\boldsymbol{\nabla}\mathbf{V} + \boldsymbol{\nabla}\mathbf{V}^T)] \cdot d\mathbf{S} \tag{5-19}$$

The integration is carried out over the entire surface area of the particle, denoted by S. Specifically, the integrand in Eq. 5-19 includes two distinct terms: the first term represents the thermodynamic pressure exerted on the particle by the surrounding fluid, while the second term accounts for the viscous stress, which arises from the fluid's viscosity resisting the particle's movement [173]. The unit tensor is denoted by **I**. Additionally, the moment of the surface forces about the particle's center of mass can be derived using the following expression.

$$\mathbf{M} = \oint_S \mathbf{r} \times \{[-p\mathbf{I} + \mu(\boldsymbol{\nabla}\mathbf{V} + \boldsymbol{\nabla}\mathbf{V}^T)] \cdot d\mathbf{S}\} \tag{5-20}$$

In the given equations, **r** represents the position vector of the solid-liquid interface relative to the particle's center of mass. The fields of pressure, velocity, and temperature within the liquid

domain are determined through the solutions of the flow and thermal fields, as specified in Eqs. 5-3, 5-10, and 5-13. Substituting the results from the flow and thermal fields into the force and moment equations (Eqs. 5-19 and 5-20) enables the calculation of the total forces and moments exerted on the surface of the melting particle. The translational and rotational velocities at each node on the particle surface are obtained by discretizing Eqs. 5-17 and 5-18. This is achieved using a second-order backward finite difference method, which offers a high level of accuracy in approximating the derivatives needed to predict the particle's behavior.

$$\mathbf{V}_p^n = \frac{2}{3}\left[\frac{\mathbf{F}}{m_p}\Delta t + 2\mathbf{V}_p^{n-1} - \frac{1}{2}\mathbf{V}_p^{n-2}\right] \quad 5\text{-}21$$

$$\boldsymbol{\omega}_p^n = \frac{2}{3}\left[\frac{\mathbf{M}}{m_p}\Delta t + 2\boldsymbol{\omega}_p^{n-1} - \frac{1}{2}\boldsymbol{\omega}_p^{n-2}\right] \quad 5\text{-}22$$

where n denotes the index of the time step and Δt represents the time step. The translational displacement of each node on the particle surface for every time step is determined by the instantaneous translational velocity of the node ($\mathbf{V}_p^n$).

$$\Delta\mathbf{R}_t^n = \mathbf{V}_p^n \Delta t \quad 5\text{-}23$$

In this formulation, $\mathbf{R}^n$ represents the instantaneous position vector of nodes on the particle surface relative to the referential frame, while $\Delta\mathbf{R}_t^n$ denotes the translational displacement of each node. This displacement results from the forces exerted on the particle surface during each time step. Further, the rotational displacement of each node is converted into translational displacement through the application of a rotation matrix.

$$\Delta\mathbf{R}_r^n = \begin{bmatrix} \cos(\Delta\theta^n) & -\sin(\Delta\theta^n) \\ \sin(\Delta\theta^n) & \cos(\Delta\theta^n) \end{bmatrix} (\mathbf{r}^n) \quad \text{5-24}$$

where $\Delta\theta^n = \boldsymbol{\omega}_p^n \Delta t$ represents the instantaneous rotational displacement of the particle, where $\boldsymbol{\omega}_p^n$ is the particle angular velocity at time step n. It's important to note that rotational displacement is generally a vector quantity; however, in the framework of a two-dimensional simulation, the rotational displacement is designated as positive if the rotation occurs counterclockwise and negative if clockwise.

The deformation of the particle surface due to melting is modeled by solving the conservation of energy equation at the particle surface:

$$\rho h_{sl} \frac{d\mathbf{R}_d}{dt} = -k(\boldsymbol{\nabla} T \cdot \mathbf{n})\mathbf{n} \quad \text{5-25}$$

In this formulation, h_{sl} represents the latent heat of fusion of the solid particle, the term $d\mathbf{R}_d$ refers to the deformation displacement caused by melting, $\mathbf{n}$ denotes the unit normal vector at the particle surface, oriented outward, and $\boldsymbol{\nabla} T \cdot \mathbf{n}$ represents the local temperature gradient normal to the particle boundary. It is important to note that the solid particle is assumed to be at its melting temperature throughout this process, meaning the internal temperature gradient within the particle is zero. The deformation displacement resulting from melting is calculated using a discretization of Eq. 5-25, with a first-order finite difference scheme.

$$\Delta\mathbf{R}_d^n = -\frac{k\Delta t}{\rho h_{sl}}(\boldsymbol{\nabla}T \cdot \mathbf{n})\mathbf{n} \quad 5\text{-}26$$

The total displacement of each node ($\Delta\mathbf{R}^n$) on the surface of the melting particle at each time step is determined by the sum of the translational, rotational, and deformational displacements, as follows:

$$\Delta\mathbf{R}^n = \Delta\mathbf{R}_t^n + \Delta\mathbf{R}_r^n + \Delta\mathbf{R}_d^n \quad 5\text{-}27$$

The mass source term $\dot{S}_{\text{mass}}$ in Eq. 5-3 is zero throughout the domain except in the control volumes adjacent to the solid particle surface. Within these control volumes, $\dot{S}_{\text{mass}}$ is calculated based on the local melting rate of the particle. The formula for this term is given by $\dot{S}_{\text{mass}} = [\rho Z(d\mathbf{r}/dt) \cdot d\mathbf{S}]/\, V_{\text{CV}}$, where Z represents the unit depth of the particle in the direction perpendicular to the simulation plane and V_{CV} denotes the volume of the control volume.

The governing equations for the liquid domain (Eqs. 5-3, 5-10, and 5-13) along with the equations describing the motion of the melting particle (Eqs. 5-17, 5-18, and 5-25) are non-dimensionalized to enhance their generality and applicability. This is achieved using a set of dimensionless variables defined as follows: $x^* = x/D$, $\boldsymbol{\nabla}^* = \boldsymbol{\nabla}D$, $t^* = t\nu/D^2$, $\mathbf{V}^* = \mathbf{V}/u_{\max}$, $\boldsymbol{\omega}_p^* = \left(\boldsymbol{\omega}_p D\right)/u_{\max}$, $p^* = (p + \rho g y)/(\nu\rho u_{\max}/D)$, $T^* = (T - T_m)/(T_h - T_m)$, $\mathbf{F}^* = \mathbf{F}/(\nu\rho Z u_{\max})$, and $\mathbf{M}^* = \mathbf{M}/(\nu\rho Z D u_{\max})$. This non-dimensionalization scales the variables relative to their characteristic values, simplifying the equations and making them independent of specific units. The non-dimensional form of the governing equations is presented as follows:

$$\mathrm{Re}_D(\boldsymbol{\nabla}^* \cdot \mathbf{V}^*) + \dot{S}^* = 0 \tag{5-28}$$

$$\left.\frac{\partial \mathbf{V}^*}{\partial t^*}\right|_{\mathrm{ref}} + \mathrm{Re}_D\left((\mathbf{V}^* - \mathbf{V}^*_{\mathrm{mesh}}) \cdot \boldsymbol{\nabla}^*\right)\mathbf{V}^* = -\boldsymbol{\nabla}^* p^* + {\nabla^*}^2 \mathbf{V}^* - \frac{\mathrm{Gr}}{\mathrm{Re}_D} T^* \mathbf{j} - \frac{\partial \mathbf{V}^*_{\mathrm{frame}}}{\partial t^*} \tag{5-29}$$

$$\frac{\partial T^*}{\partial t^*} + \mathrm{Re}_D(\mathbf{V}^* - \mathbf{V}^*_{\mathrm{mesh}}) \cdot \boldsymbol{\nabla}^* T^* = \frac{1}{\mathrm{Pr}} {\nabla^*}^2 T^* \tag{5-30}$$

$$\frac{\pi}{4} m^* \frac{d\mathbf{V}_p^*}{dt^*} = \mathbf{F}^* \tag{5-31}$$

$$\frac{\pi}{32}\left(\frac{I_p}{I_{p,0}}\right)\frac{d\boldsymbol{\omega}_p^*}{dt^*} = \mathbf{M}^* \tag{5-32}$$

$$\frac{1}{\mathrm{Ste}} \frac{d\mathbf{R}_d^*}{dt^*} = -\frac{1}{\mathrm{Pr}} (\boldsymbol{\nabla}^* T^* \cdot \mathbf{n})\mathbf{n} \tag{5-33}$$

The dimensionless numbers used to characterize the fluid dynamics and heat transfer in this model include the Prandtl number (Pr), Reynolds number based on particle diameter (Re_D), Grashof number (Gr), and Stefan number (Ste). The Prandtl number is defined as $\mathrm{Pr} = \nu/\alpha$, which represents the ratio of momentum diffusivity to thermal diffusivity of the fluid. The Reynolds number is defined as $\mathrm{Re}_D = u_{\max} D/\nu$, indicates the ratio of inertial forces to viscous forces. It is characterized by the maximum flow velocity and the particle's initial diameter. Given that the initial particle diameter and liquid kinematic viscosity are constants, Re_D serves as an indicator of the inlet flow velocity, highlighting the flow's inertial characteristics. Grashof number expressed as $\mathrm{Gr} = g\beta D^3(T_h - T_m)/\nu^2$, quantifies the ratio of buoyancy forces to viscous forces in the fluid.

It reflects the strength of the buoyancy forces acting on the particle due to natural convection, influenced by the temperature difference between the particle surface (T_m) and the walls (T_h). The Stefan number defined by $\mathrm{Ste} = c(T_h - T_m)/h_{\mathrm{sl}}$, is the ratio of sensible heat to latent heat of fusion. It is based on the temperature difference between the particle (T_m) and the walls (T_h). A higher Stefan number suggests a dominance of sensible heat over latent heat, leading to a greater rate of melting. It determines the characteristic melting time. In the calculations of these dimensionless numbers, ν represents the kinematic viscosity, α denotes the thermal diffusivity, and $u_{\max} = \Delta p W^2/(8L\mu)$ is the maximum velocity of the undisturbed flow.

5.4.1. Measurement Approach

The dimensionless parameters employed in the simulations, along with the values explored, are outlined in Table 1. This table includes Y_0^*, which is the dimensionless initial lateral position of the particle, calculated as $Y_0^* = y_0/W$. The channel Re number is also detailed in Table 5-1, defined as $\mathrm{Re} = u_{\max} W/\nu$, is based on the channel width.

Table 5-1 The dimensionless parameters employed in the numerical simulation.

Dimensionless parameter	Value
Y_0^*	0.25, 0.5, 0.75
Pr	0.7
Re	0, 100, 500, 1000
Gr	0, 100, 1000, 10000
Ste	0, 0.01, 0.1, 0.5

To explore the behavior of fluids in the laminar flow regime, the Re is maintained below 1,000. This ensures that the flow conditions remain within the laminar range. A broad spectrum of values is considered for the Gr number, ranging from 0 to 10,000. This extensive range allows for the examination of varying degrees of buoyancy effects on the particle, from negligible to substantial. The Ste number is deliberately kept below 0.5 to avoid rapid melting of the particle. Higher values of Ste lead to quicker phase changes, which might not be ideal for detailed observational studies of the melting process over time. Lastly, the Pr number is held constant throughout all simulations. This decision is based on preliminary findings that variations in Pr show minimal impact on both the rate of melting and the migration paths of the particle. For the melting of an ice particle with a presumed diameter of 2 mm, 3 mm, and 4 mm in water, Gr number of 10,000 can be achieved with wall temperature of 64°C, 19°C, and 8°C, respectively.

5.4.2. Numerical Procedure

The governing equations were resolved using a pressure-based finite volume method, implemented in the commercial Computational Fluid Dynamics (CFD) software, ANSYS Fluent version 19.1. To couple the pressure and velocity fields within the simulation, the SIMPLE algorithm was utilized [174]. For the discretization of advective terms within the governing equations, the Quadratic Upstream Interpolation for Convective Kinematics (QUICK) scheme was employed. This second-order differencing method uses a parabolic curve to approximate the variable profile between two nodes. To construct the parabolic curve, a third point is selected on the upstream side of the flow to capture the influence of convection. The pressure gradient term was computed using the Standard method, wherein pressure values are interpolated at the cell faces using coefficients derived from the momentum equation [175]. Time discretization was handled using a first-order

implicit scheme. Several User Defined Functions (UDFs) were developed in C++ and integrated into the solver. These functions were employed for: (i) calculating the net force and moment exerted on the particle, as well as the heat transfer rate at the solid-liquid interface, and the consequent translational, rotational, and deformational motions; (ii) updating the positions of computational nodes on the particle surface; and (iii) determining the mass source term added to the fluid control volumes adjacent to the particle boundary due to melting. To ensure the stability of the solution and convergence in each time step, under-relaxation factors of 0.2, 0.5, and 0.7 were applied to the pressure, momentum, and energy equations, respectively. The convergence criterion was set such that the solution was considered converged when the scaled residuals decreased to 10^{-4} for the continuity and momentum equations, and 10^{-7} for the energy equation.

The governing equations were solved on a multi-block hybrid grid, incorporating triangular and quadrilateral elements as illustrated in Fig. 5-3. Specifically, the rectangular region surrounding the particle, which is centrally located within the domain, was meshed with triangular elements. This choice facilitates grid deformation and remeshing, necessary for modeling the dynamic interactions and transformations occurring around the melting particle. Additionally, the displacement of the particle surface nodes is depicted. Outside this central area, the remainder of the domain was structured using a fixed grid composed of quadrilateral elements. This structured region is less affected by direct interactions with the particle. Moreover, a boundary layer mesh was implemented along the channel walls. This enhancement is critical for capturing the velocity and temperature gradients near the walls with greater precision.

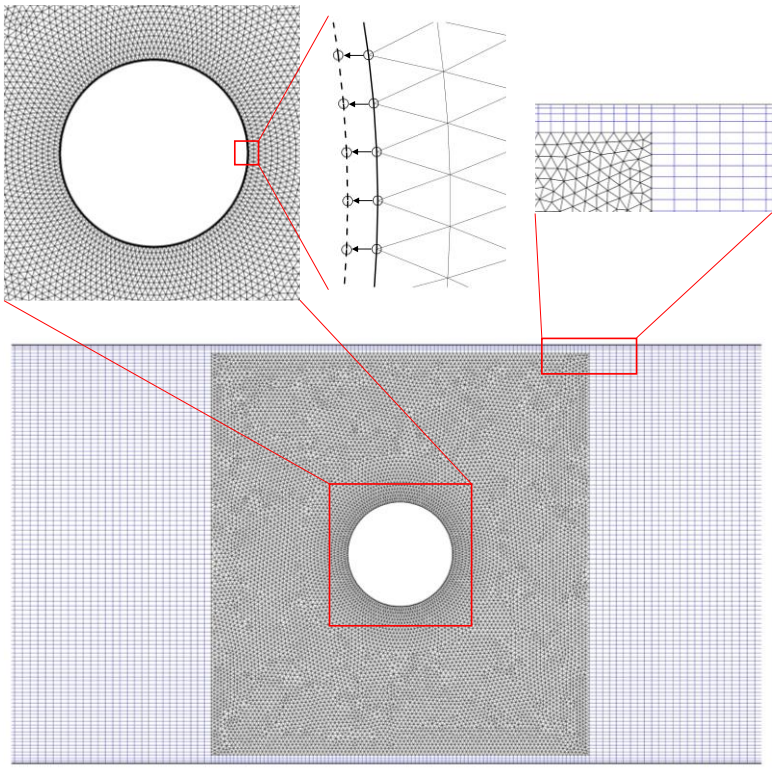

Fig. 5-3 Snapshot of the initial grid configuration, featuring a close-up of the finely meshed area around the particle, the displacement of the particle surface nodes, and the boundary layer mesh near the channel walls.

5.4.3. Grid & Time Step Size Independence

To ensure the reliability of the simulation results, a grid independence test was conducted to evaluate the impact of grid size on the predicted lateral position and the melting rate of the melting particle. Figure 5-4 illustrates the influence of grid refinement on these predictions. Increasing the number of control volumes from N = 47,000 to N = 75,000 does not significantly alter the outcomes. This observation suggests that the finer grid does not provide substantial additional accuracy for these specific simulation parameters. Consequently, a grid with 47,000 control

volumes, which includes 75 control surfaces on the particle surface, has been considered sufficient for the numerical simulations.

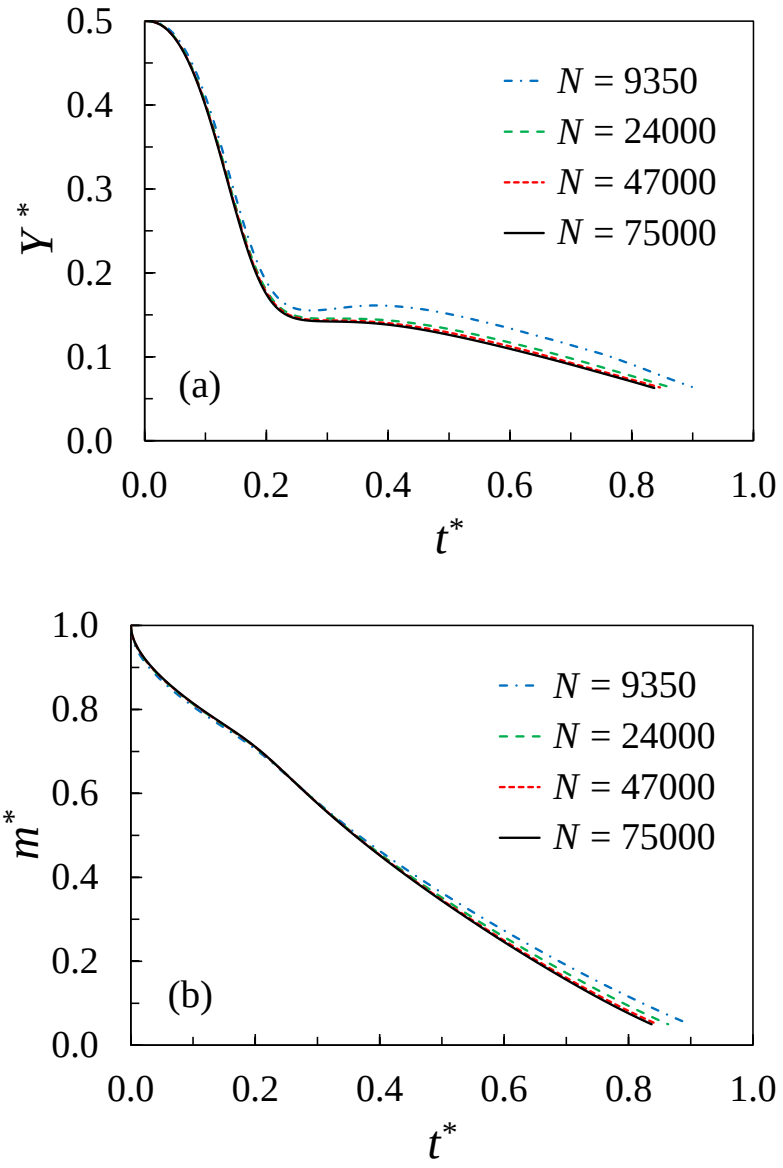

Fig. 5-4 Grid size impact on (a) lateral position, and (b) mass of the particle over dimensionless time, for Re = 100, Gr =1,000, Ste = 0.1, Y_0^* = 0.5, and Δt = 0.01 s.

The independence of simulation results from the time step size was conducted using varying time steps: Δt = 0.005 s, 0.010 s, and 0.050 s. Figure 5-5 illustrates the influence of these different time step sizes on the lateral position of the particle and its mass throughout the

simulation. The analysis indicates that the results are consistent across the range of time steps tested, showing no significant dependency on the time step size. Based on these findings, a time step size of Δt = 0.010 s has been selected for use in the numerical simulations.

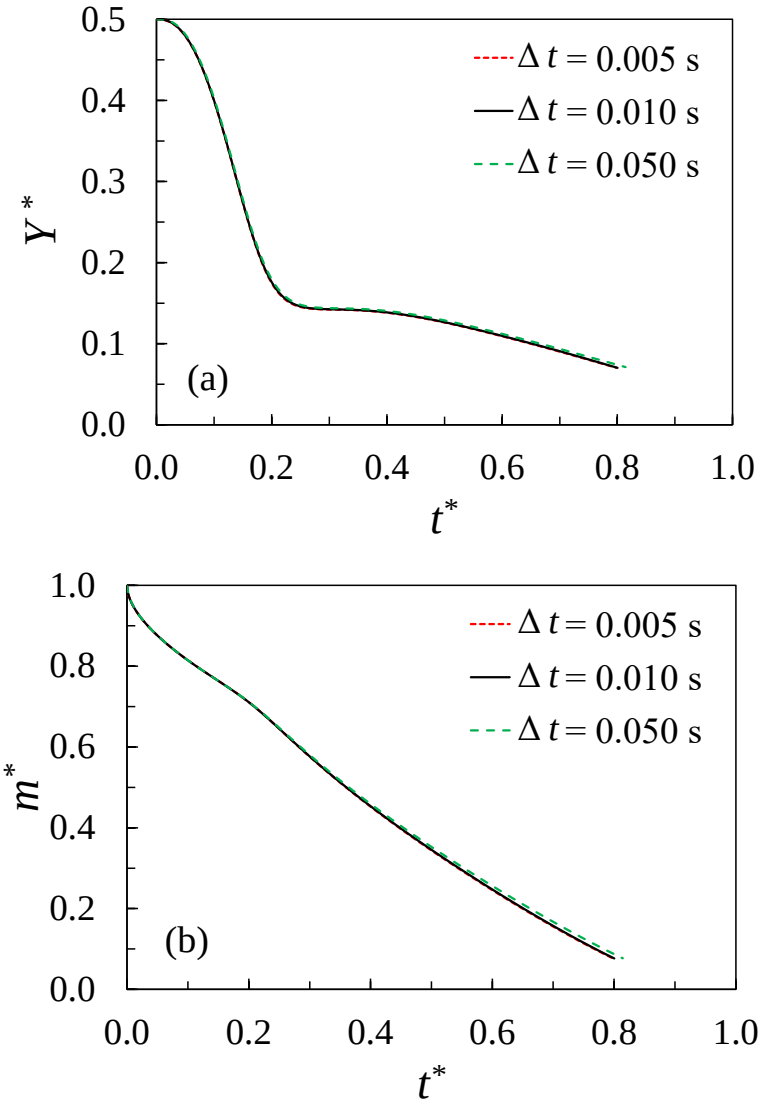

Fig. 5-5 The time step size influence on the numerically predicted (a) lateral position, and (b) mass of the particle (for Re = 100, Gr = 1,000, Ste = 0.1, Y_0^* = 0.5, and N = 47,000).

5.4.4. Model Validation

The model was validated by comparing the simulation results with established findings from the literature across three distinct scenarios: (i) the migration of a neutrally buoyant particle in a horizontal channel under Poiseuille flow with thermal convection, (ii) the sedimentation of a cylindrical particle in a vertical channel with natural convection, and (iii) the sedimentation and melting of an initially cylindrical particle in a vertical channel. For the first two cases, comparisons were made regarding the lateral migration of the particle against the results documented in multiple studies. For the third scenario, the sedimentation velocity and melting rate were benchmarked against the findings reported by Gan et al. [176].

Neutrally Buoyant Particle Migration in Horizontal Poiseuille Flow

The schematic for this case study is similar to Fig. 5-1 and presents a scenario where the particle is initially centered in the x-direction within the channel and varying initial lateral positions are explored. The simulation parameters used for comparison include a Pr number of 0.7, a Re number of 96.12, and a Gr number of 1,000, with dimensionless initial lateral positions W_0^* = 0.25, 0.50, and 0.75. A pressure gradient of $\Delta p^*/L^*$ = 0.5 was applied to achieve the specified Re. An equilibrium position $W_{\mathrm{eq}}^*= y_{\mathrm{eq}}/W$ = 0.2244 was calculated and found consistent across different initial lateral positions, indicating stability in the particle's lateral migration. This predicted equilibrium position closely aligns with the findings of Hu et al. [177] (W_{eq}^* = 0.2146), demonstrating a discrepancy of less than 5%.

Cylindrical Particle Sedimentation in Vertical Channel

In the second validation scenario, the process of sedimentation of a cold particle in a vertical channel with thermal convection was modeled. The results focusing on the equilibrium lateral position of the particle were then compared with existing data in the literature to assess accuracy. As depicted in Fig. 5-6, the simulation involves a cylindrical particle with a diameter D and a slight density differential, expressed as ρ_s/ρ_l = 1.00232, being released in a vertical channel. Initially, the particle is positioned at half its diameter (x_0/D = 1.5) away from the central line of the channel and $10D$ above the bottom. The channel dimensions are specified as $W = 4D$ wide and $L = 32D$ long in the x- and y-directions, respectively.

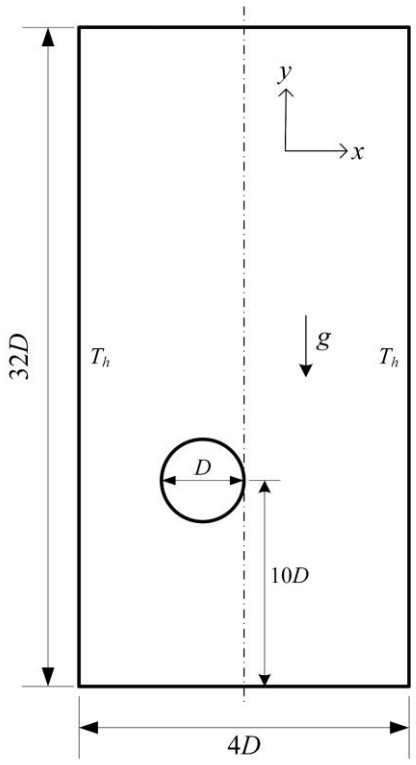

Fig. 5-6 Schematic of a cold particle settling in a vertical channel.

The particle Re number is calculated using a characteristic velocity defined as $u_c = \sqrt{\pi(D/2)(\rho_s/\rho_l - 1)g}$, and set at Re_D = 40.5. Figure 5-7 illustrates the temporal progression of the particle's position ($x^* = x/D$) across different Gr numbers. Additionally, Table 5-2 presents the equilibrium lateral positions of the particle as determined by the current model for Gr numbers of 1,000 and 2,000. These positions are also compared with corresponding numerical values reported in previous studies. The data outlined in Table 5-2 indicates that the predictions from the current study align remarkably well with the outcomes of other numerical models under the same flow conditions.

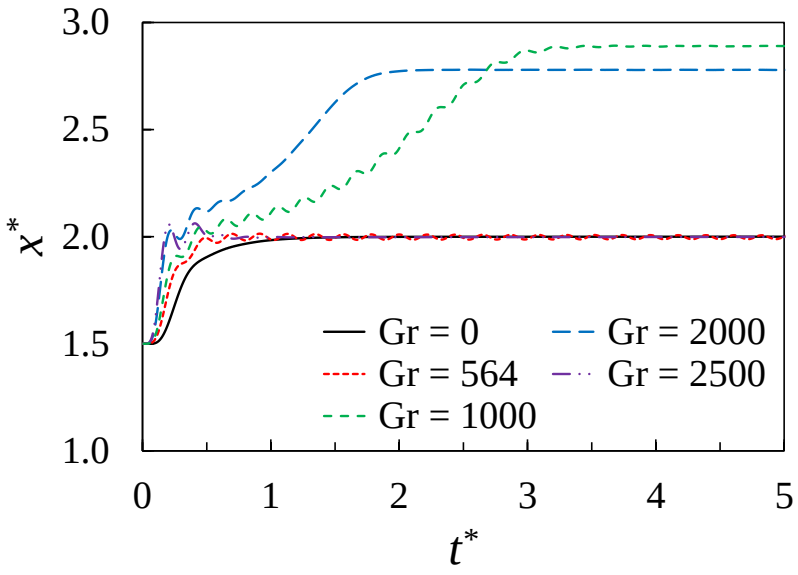

Fig. 5-7 Lateral positioning of a cold particle during descent in a channel across different Gr numbers.

Table 5-2 Comparison of equilibrium lateral position obtained from the current model with available data from the literature for Gr = 1,000 and 2,000.

Gr	Present work	Hu et al. [177]	Liu et al. [178]	Yu et al. [179]	Feng et al. [180]	Kang et al. [181]	Yang et al. [182]
1,000	2.89	2.91	2.92	2.89	2.90	2.89	2.89
2,000	2.78	2.76	2.76	2.74	2.73	2.74	2.79

Cylindrical Particle Sedimentation & Melting in a Vertical Channel

In this study, the focus is on analyzing the sedimentation velocity and melting rate of a single particle as it settles in its own melt. The particle is released at the channel's centerline, positioned $10D$ above the bottom boundary of the computational domain, where D represents the initial diameter of the particle. Initially, the melt is in thermal equilibrium with the channel walls. No-slip boundary conditions and a constant wall temperature T_h are maintained at the side walls, while the particle's temperature is held at its melting point. The parameters controlling the simulation—Pr = 0.7, Re = 21.1, Gr = 100, ρ_s/ρ_l = 1.00232, and Ste = 0.0251—are set to match those used in the study by Gan et al. [162]. Notably, the Re number is calculated based on the maximum sedimentation velocity of the particle, which remains undetermined until the simulation progresses. Figure 5-8 provides a visual representation of the particle's dimensionless mass and Re number as it undergoes the processes of settling and melting.

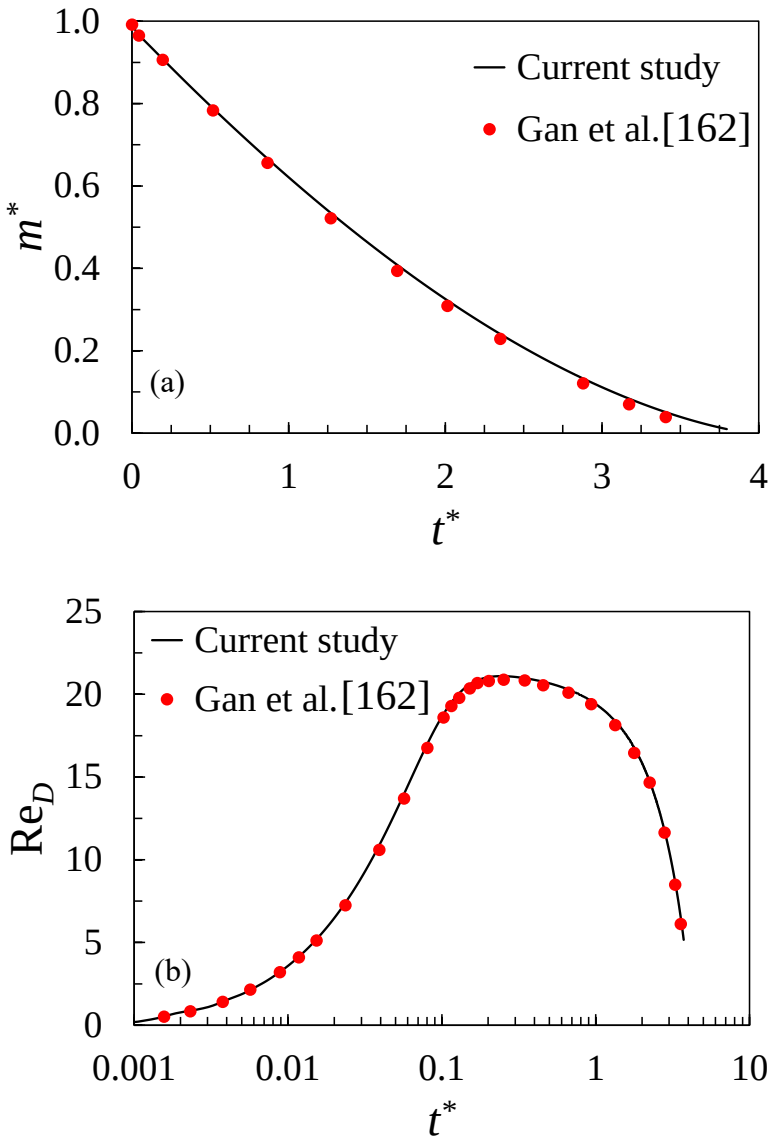

Fig. 5-8 Comparison of (a) dimensionless particle mass, and (b) instantaneous Re number, for the settling and melting particle in a vertical channel with numerical results of Gan et al. [162].

As shown in Fig. 5-8, the computational results align closely with those reported by Gan et al. [162]. The deviations observed are minimal, with a maximum of 2% for the Re number and 7% for the particle mass. Based on the results of these three validation cases, the simulation model is effectively validated, demonstrating its accuracy and reliability for predicting the fluid dynamics and thermal processes.

6. Particle Migration and Melting Simulation Results[5]

The dynamics and thermal behavior of the moving and deforming melting particle are studied in this chapter. Initially, the time evolution of the particle morphology alongside the streamlines are analyzed, focusing on the changes observed during the particle migration and melting process. Following this, a detailed examination of different parameter effects including Reynolds number, Grashof number, Stefan number, and the dimensionless initial lateral position (Y_0^*) on the hydrodynamic and heat transfer characteristics of the particle is studied.

6.1. Melting Particle Morphology

Figure 6-1 illustrates the morphological changes of a melting particle and the evolution of the surrounding temperature field at various times under these conditions: Gr = 1,000, Ste = 0.1, and Y_0^*= 0.5, at two different Re numbers of 100 and 1,000. Figure 6-1(a) highlights how the morphology of the solid particle is altered during the melting process due to the non-uniform heat distribution from the adjacent heated wall. As the particle descends towards the bottom wall, the lower side encounters higher heat fluxes, leading to a faster melting rate compared to the upper side. This different melting rate transforms the initially circular particle into an increasingly oval shape over time. The figure also shows that the thermal gradients are more pronounced laterally than along the flow direction, a direct result of the proximity to the heated walls. When the Re number is increased from 100 to 1,000, there is a noticeable increase in the particle's rotational velocity, which promotes a more uniform distribution of heat around the particle's surface. As

[5] The content of this chapter is an extension of a published paper by the author. The paper contains results of research which was solely conducted as partial fulfillment for the PhD requirement. Materials presented in the paper have not been submitted for a course or extra credit.

depicted in Fig. 6-1(b), this uniformity helps to maintain the particle's circular shape throughout the melting process. It should be noted that the densities of the solid and liquid phases are identical; therefore, there is no settling movement due to density differences. Instead, the downward motion of the particle is driven solely by the buoyancy effects of the natural convection flow, which occurs around the relatively cold particle as it interacts with the warmer fluid environment.

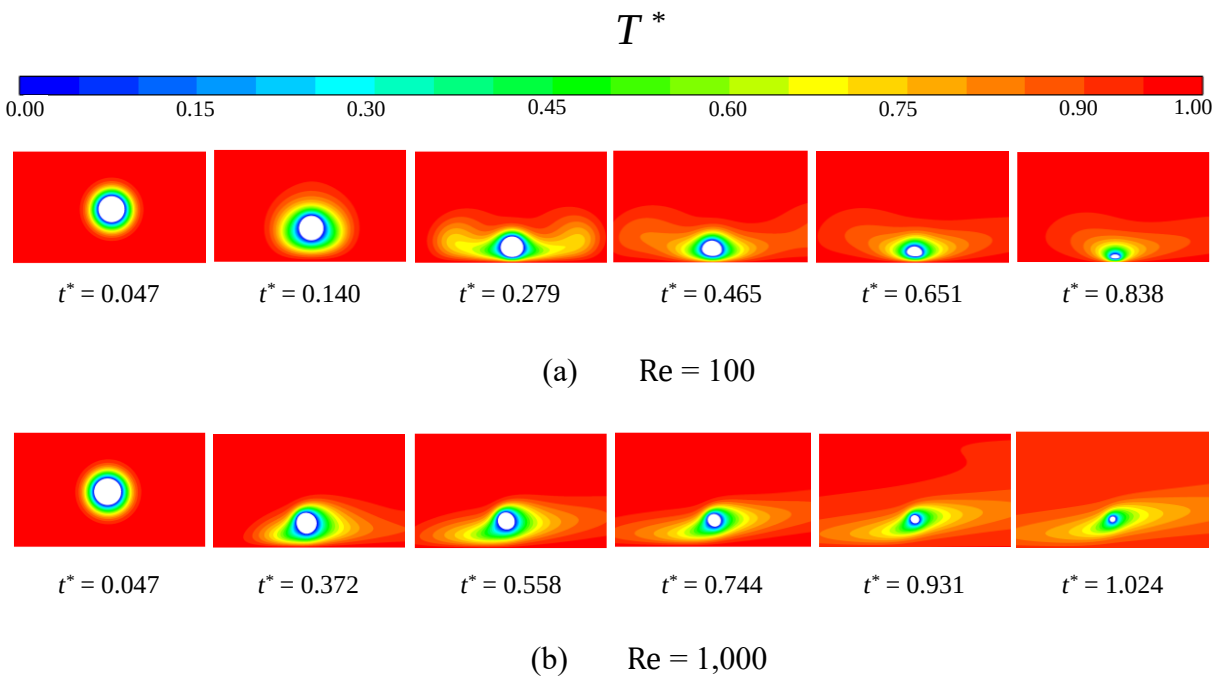

Fig. 6-1 Evolution of the temperature field surrounding the melting particle over time for Gr = 1,000, Ste = 0.1, Y_0^* = 0.5, with comparisons between (a) Re = 100 and (b) Re = 1,000. The final observation point is when the particle mass has reduced to 5% of its initial mass.

6.2. Streamlines

Figure 6-2 depicts the streamlines within the domain. The cooler liquid surrounding the particle descends due to its higher density, while the warmer liquid near the relatively hot bottom wall rises, creating a circulation pattern. This thermal-driven movement results in the formation of two

asymmetric vortex structures around the particle. Over time, as the velocity profile evolves, the upstream vortex remains closely associated with the particle, maintaining its position near or attached to it. In contrast, the downstream vortex becomes detached and moves further away from the particle. This interaction between the particle and the surrounding fluid's flow dynamics influences the slip velocity—the relative velocity of the particle compared to the fluid—and the particle's angular velocity, which will be studied in the subsequent sections.

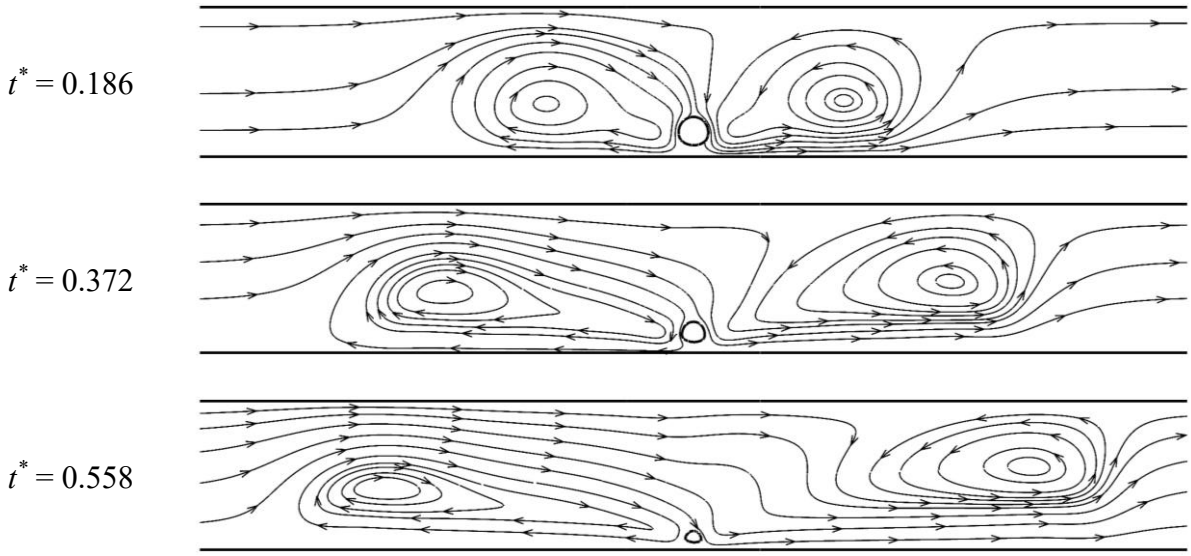

Fig. 6-2 Streamlines surrounding the particle at various dimensionless times for Gr = 10,000, Re = 100, Ste = 0.1, and Y_0^* = 0.5.

6.3. Parametric Studies on the Effect of Re, Gr, Ste, & Y_0^*

The dimensionless parameters Re, Gr, and Ste numbers, and the dimensionless initial lateral position (Y_0^*) were systematically varied to explore their effects on the lateral position, melting rate, and heat transfer characteristics of the particle. To quantitatively assess the heat transfer rate on the particle surface, an average Nusselt number (Nu) was calculated over the particle's surface.

This Nu number serves as a dimensionless indicator that characterizes the rate of convective heat transfer at the surface relative to the rate of conductive heat transfer through the fluid.

$$\mathrm{Nu} = \frac{1}{\pi(T_h - T_m)k} \oint\!\!\int_S \mathbf{q}'' \cdot d\mathbf{S} = \frac{hd_c}{k} \tag{6-1}$$

where $\mathbf{q}''$ represents the local heat flux at the particle surface, capturing the rate at which heat is being transferred per unit area. The average convective heat transfer coefficient is denoted by h, and d_c is defined as the instantaneous characteristic particle diameter. This diameter is calculated to be equivalent to that of a circle which has the same perimeter as the particle, mathematically expressed as $d_c = \frac{1}{\pi}\int_S dS$.

The fluid begins the simulation at rest and gradually accelerates due to a constant pressure gradient applied along the channel. Figure 6-3 illustrates the transient evolution of the inlet flow velocity over time. The condition of fully developed flow is considered achieved when the normalized velocity ($u/u_{\max}$) nears unity at the center of the channel ($Y_0^* = 0.5$). However, even at the largest dimensionless time depicted in Fig. 6-3, the flow remains in a developing state and has not yet reached a fully developed condition. As will be discussed later, in most cases examined in this study, the particle undergoes complete melting before the flow can achieve this fully developed state.

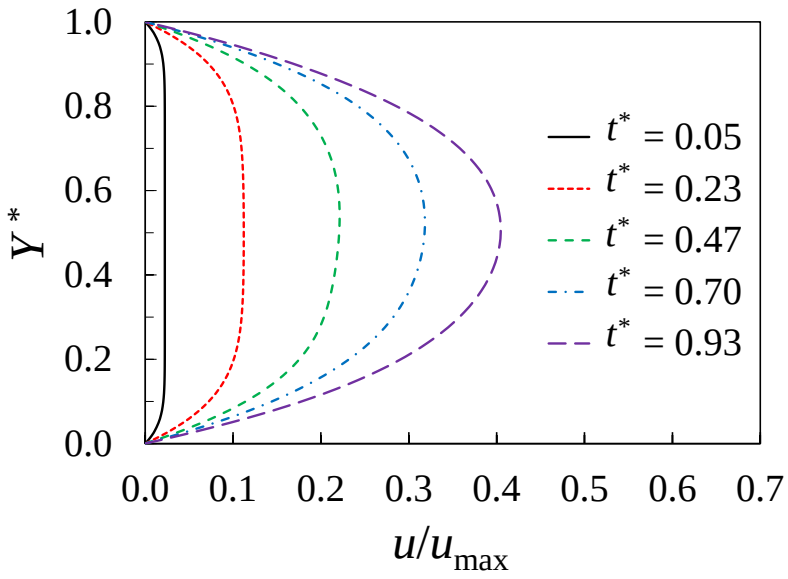

Fig. 6-3 Temporal progression of inlet flow velocity subject to a constant pressure gradient.

Figure 6-4 illustrates how changes in the Re number impact the transient lateral position of the particle, its mass, and the Nu number under the conditions of Gr = 1,000, Ste = 0.1, and Y_0^* = 0.5. It is observed that a moderate increase in Re, from 0 to 100, has a minimal effect on the particle's trajectory. However, further elevating Re to 500 and then to 1,000 induces significant alterations in the particle trajectory. This phenomenon occurs because as Re increases, the dominance of advective forces begins to surpass the effects of natural convection, leading to substantial changes in both the flow dynamics and thermal fields surrounding the particle.

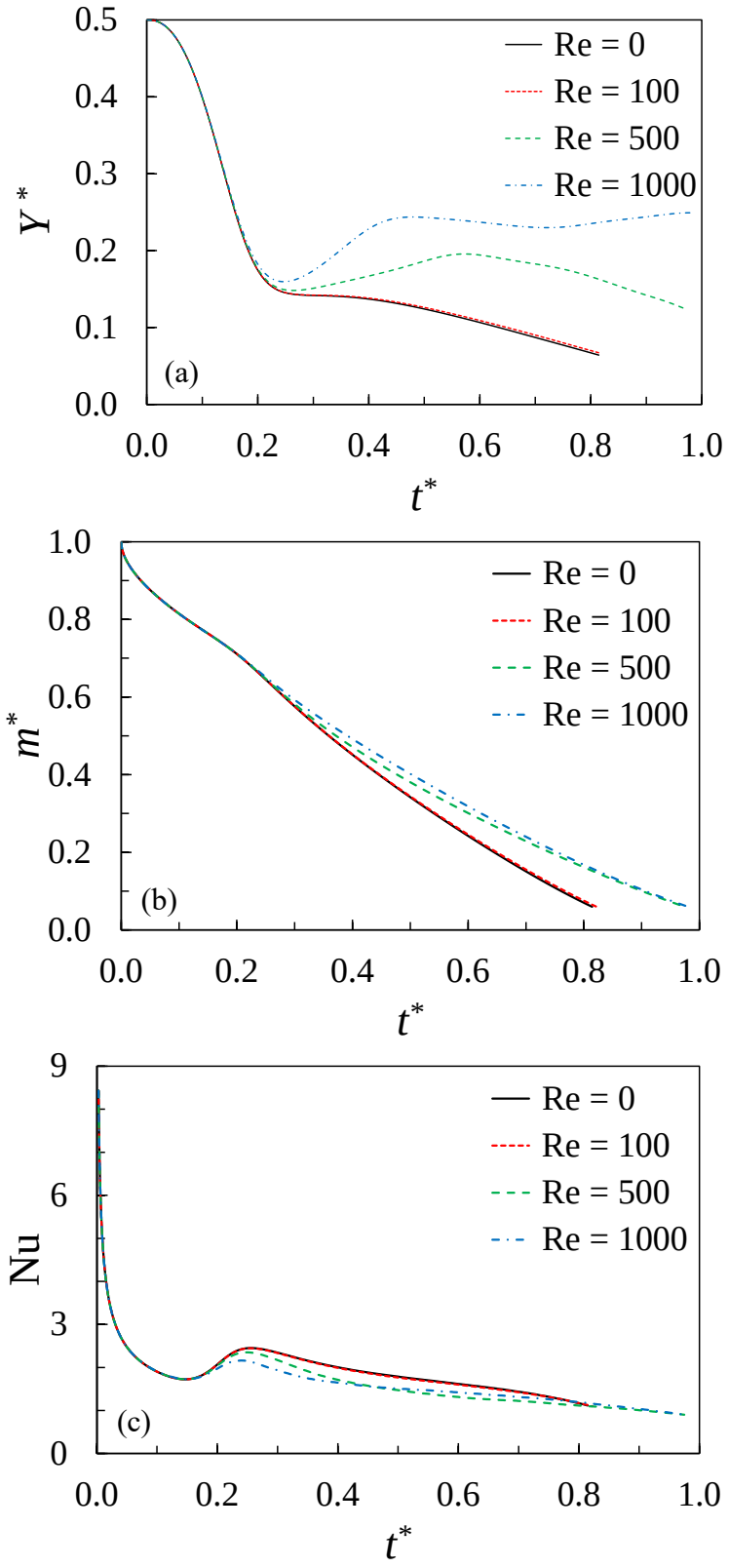

Fig. 6-4 The impact of Re number on the computationally determined transient (a) lateral position, (b) particle mass, and (c) Nu number. Results for Gr = 1000, Ste = 0.1, and $Y_0^* = 0.5$.

Figure 6-4 reveals that the particle lateral position, particle mass, and Nu number on the particle surface are similar across all considered Re number values until a dimensionless time of approximately $t^* \approx 0.2$. This initial uniformity can be attributed to the fluid's starting condition of being at rest, with the flow only beginning to accelerate due to the applied pressure gradient as the simulation begins. In these early stages, the average flow velocity remains relatively low, and the fluid's velocity profile has not yet developed fully. Consequently, the particle's motion is predominantly influenced by the natural convection around it, causing it to migrate downward along with the downward movement of the natural convection flow. As the particle descends and moves away from the channel's centerline, the increasing velocity difference between the upper and lower sides of the particle, driven by the parabolic nature of the developing velocity profile, leads to a clockwise (negative) rotation of the particle. This rotation generates increased pressure on the particle's lower side—a phenomenon known as the Magnus effect [183]—which exerts an upward force on the particle. The magnitude of this upward force, along with the velocity difference and angular velocity, escalates with higher Re values. For Re values of 500 and 1,000, these dynamics cause the particle to shift slightly closer to the centerline, thereby reducing its exposure to the heated wall. This reduced proximity results in a lower melting rate, as depicted in Fig. 6-4(b).

Figure 6-4(c) illustrates the impact of Re number on the Nu number, as defined in Eq. 6-1. Across all Re values, Nu starts high and then drops significantly in the early stages of the simulation. This initial surge in Nu can be attributed to the large temperature difference between the particle, which maintains a constant temperature at T_m, and the surrounding fluid, initially at T_h but cooling over time due to thermal diffusion from the particle surface. Consequently, the temperature gradient at the particle surface is most pronounced at the start of the simulation,

leading to a higher initial heat transfer rate which diminishes as the temperature difference decreases. Simultaneously, the particle, initially released from the centerline, moves closer to the heated bottom wall due to downward natural convection-induced flow. This movement affects the thermal dynamics: while the decreasing temperature gradients at the particle surface leads to a reduction in the heat transfer rate, the proximity to the heated bottom increases it. In the initial phase ($t^* \lesssim 0.15$), the reduction in temperature gradient is the dominant factor, resulting in a decrease in Nu. For $0.15 \lesssim t^* \lesssim 0.25$, the influence of the heated wall becomes slightly more pronounced, causing an increase in Nu. In later stages, as the particle's lateral movement stabilizes and continuous diffusion along with particle shrinkage persists, the overall heat transfer rate gradually declines. Moreover, as shown in Fig. 6-4(c), increasing Re tends to result in a marginally lower Nu. This trend is linked to the particle's relatively greater distance from the heated bottom wall at higher Re values, as depicted in Fig. 6-4(a).

Figure 6-5 shows how Re number influences the predicted transient slip and rotational velocities of the particle. The slip velocity is calculated as the difference between the particle's axial velocity and the corresponding undisturbed flow velocity at the same lateral position as the particle's center. As depicted in Fig. 6-5(a), across all considered Re values, the particle consistently lags behind the flow. Notably, this lag tends to increase with higher Re values, indicating a more pronounced relative motion. However, at Re = 1,000, the magnitude of this lag decreases after $t^* \approx 0.3$. This reduction is associated with the particle's migration towards the channel centerline, as observed in Fig. 6-4(a). Furthermore, Fig. 6-5(b) illustrates that the rotational velocity of the particle generally increases with higher Re. This trend is due to the growing velocity difference between the top and bottom of the particle as Re increases, raising the rotational velocity. For Re = 500 and 1,000, an oscillatory pattern is noted in the rotational velocity.

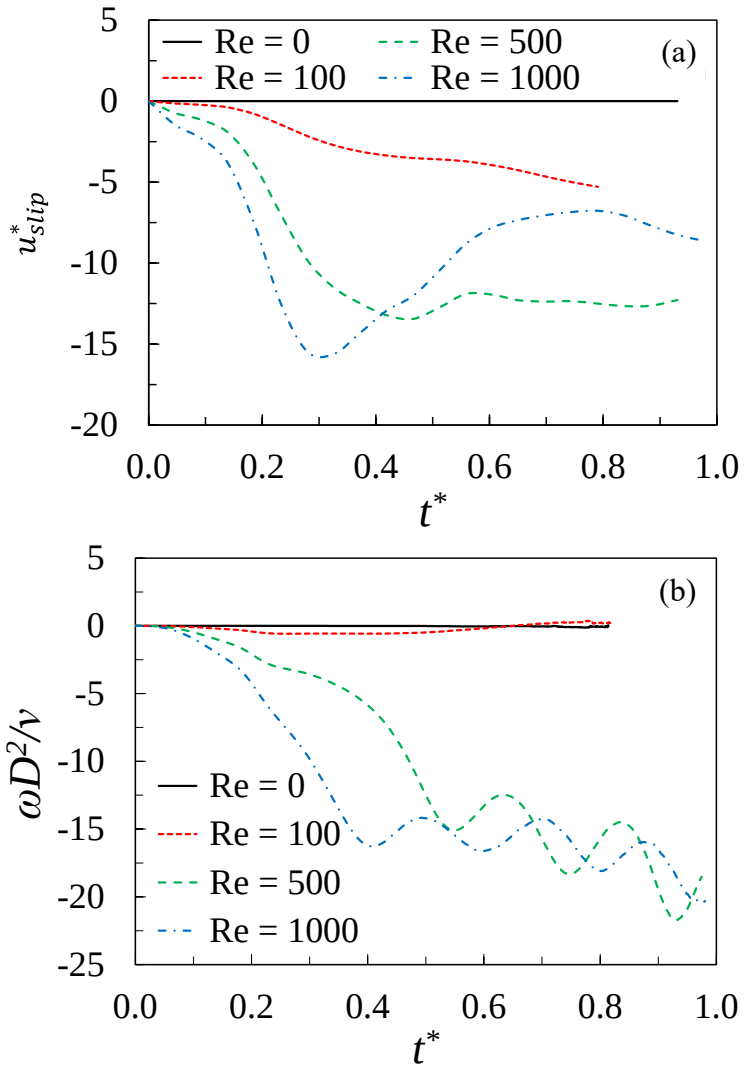

Fig. 6-5 The impact of Re number on the predicted transient (a) slip velocity and (b) rotational velocity. Results are obtained for Gr = 1000, Ste = 0.1, and Y_0^* = 0.5.

Figure 6-6 illustrates the effect of the Gr number on the transient lateral position, particle mass, and Nu number. As shown in Fig. 6-6(a), under conditions where natural convection is present (Gr > 0), a particle initially positioned at the channel centerline descends. This downward movement is primarily due to the cooling of the liquid surrounding the melting particle, which increases the density of the nearby fluid, causing it to sink and consequently pull the particle downward along with it. This process develops in two distinct phases observable in Fig. 6-6(a) as the particle approaches the bottom wall.

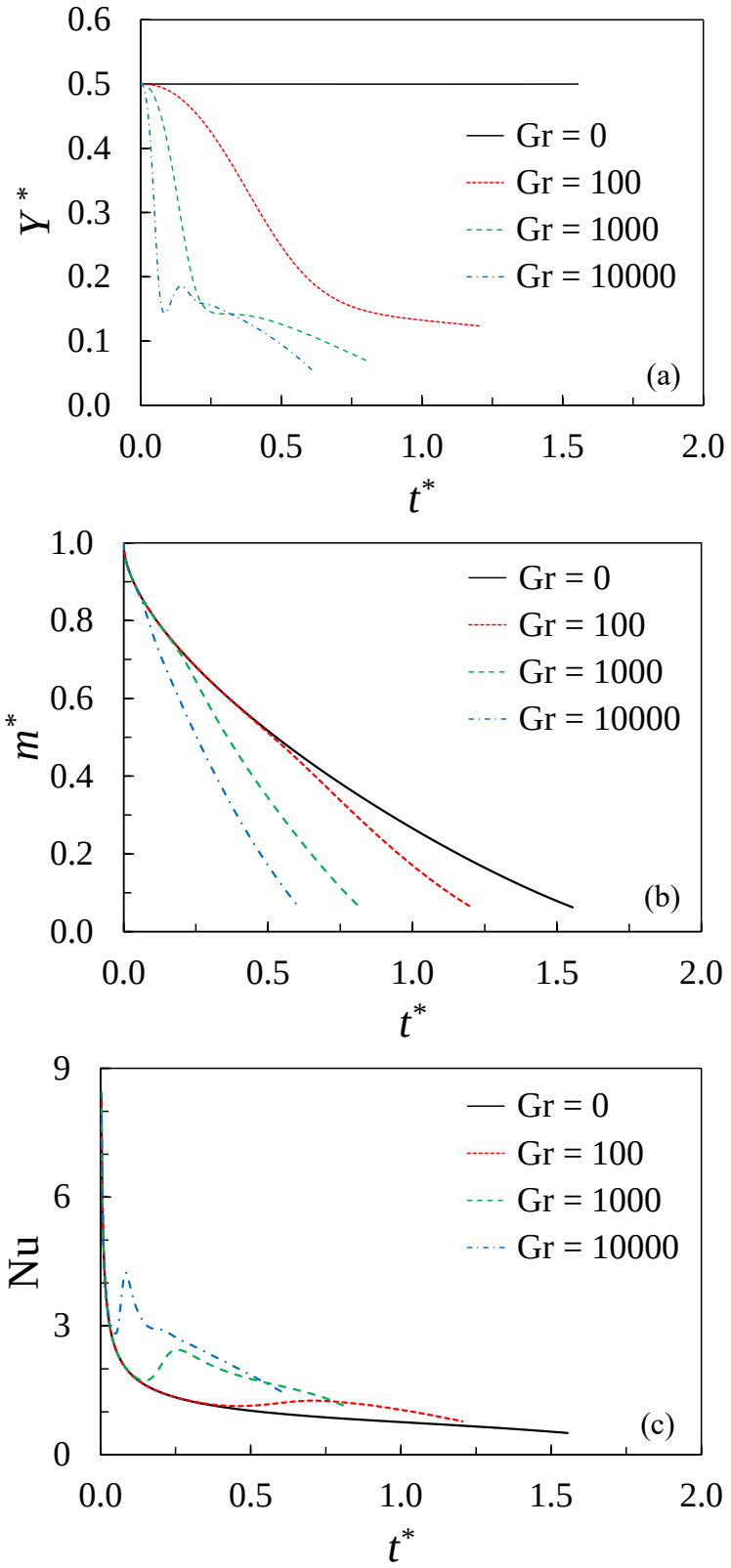

Fig. 6-6 The impact of Gr number on (a) the lateral position, (b) the mass of the particle, and (c) the Nu number for Re = 100, Ste = 0.1, and Y_0^* = 0.5.

Initially, during the first stage, the particle experiences relatively rapid downward motion. At this point, the average flow velocity in the channel is still low, and the velocity profile is in the process of developing. The dominant force acting on the particle is the downward natural convection flow, which is stronger than the advective motion along the channel, resulting in the particle's rapid descent. In the subsequent second stage, as the particle gets closer to the bottom wall, the pressure underneath it gradually increases. This increasing pressure acts to decelerate the particle's movement toward the bottom wall. Figure 6-7 illustrates the pressure field around the particle at various dimensionless times for Re = 100, Gr = 1,000, and Y_0^* = 0.5. Over time, the rising pressure effectively balances out the downward buoyancy-induced force, causing the lateral position of the particle to stabilize and eventually reach a plateau. At higher Gr numbers, such as 1,000 and 10,000, the downward movement of the particle is still noticeable at the latter stages of the melting process. As shown in Fig. 6-7, from t^* = 0.466 to t^* = 0.745 the bottom boundary of the particle maintains a nearly constant distance from the bottom wall, even as the particle continues to shrink due to melting. This shrinkage shifts the particle's center of mass downward, corresponding to the gradual descent observed in Fig. 6-6(a).

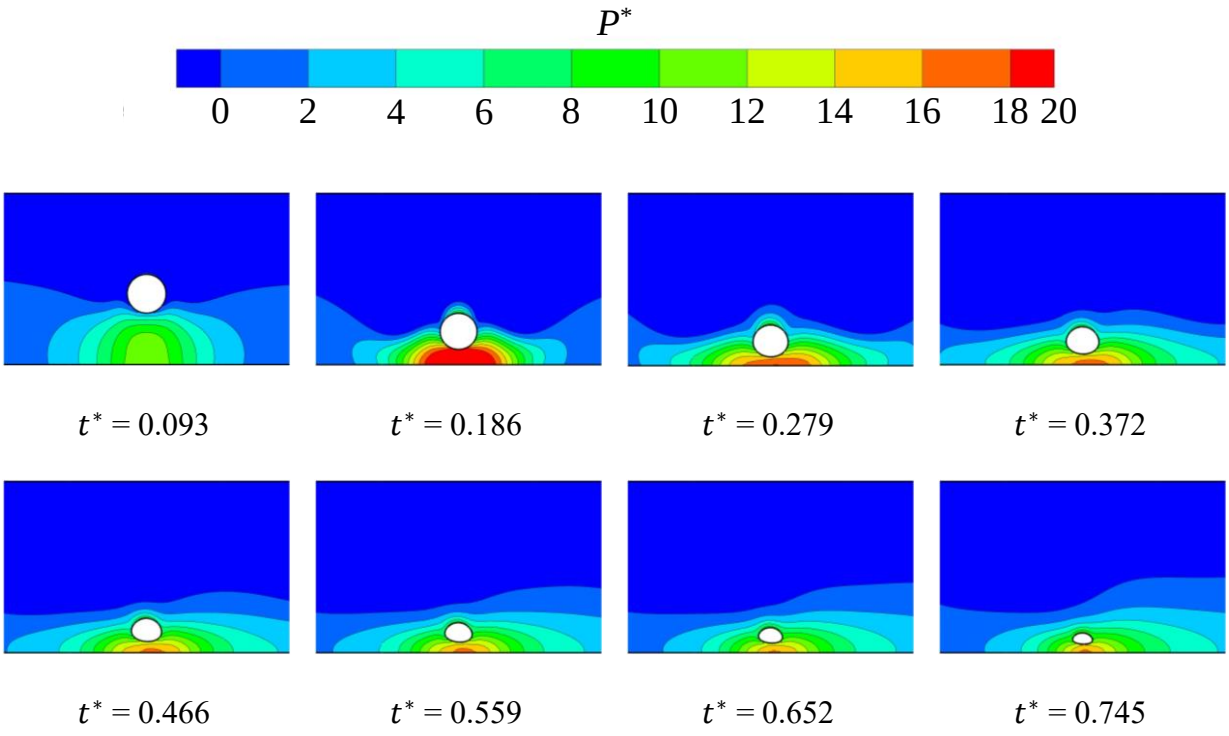

Fig. 6-7 The pressure distribution around the particle for Re = 100, Gr = 1,000, and $Y_0^* = 0.5$ and multiple dimensionless times.

Figure 6-6(b) demonstrates that as the Gr number increases, the melting rate of the particle also increases. This correlation can be attributed to a more pronounced natural convection heat transfer and a stronger downward drag force that pushes the particle closer to the heated wall. With an increase in Gr, the particle not only migrates more rapidly towards the relatively hot bottom wall but also remains in close proximity to it for a longer period. This exposure results in enhanced heat transfer rates, as evidenced by the increased Nu number values illustrated in Fig. 6-6(c).

The Ste number is a critical parameter that predominantly governs the melting rate of the particle. An increase in the Ste results in a quicker melting process, primarily due to a relatively lower latent heat of fusion required for the phase change. Figure 6-8 illustrates the impact of different Ste values on the computationally determined transient lateral position of the particle, its

mass, and the Nu number for these conditions: Re = 100, Gr = 1,000, and Y_0^* = 0.5. Initially, as shown in Fig. 6-8(a), the particle rapidly moves towards the bottom wall across all the Ste values being studied. Notably, Ste = 0 corresponds to a scenario where the particle does not melt. In comparison to the melting cases, the non-melting particle retains a larger time-averaged diameter, which creates a more significant velocity differential between its top and bottom, resulting in a higher clockwise angular velocity. This, in turn, generates a stronger upward Magnus force, propelling the particle closer to the channel's centerline. When Ste = 0.01, the melting progresses slowly, allowing the particle to maintain a trajectory similar to that of the non-melting particle until $t^* \approx 3$. For $t^* \gtrsim 3$, the trajectory begins to diverge noticeably from that of the non-melting case. This divergence suggests that as the particle reduces in size, the influence of natural convection becomes more pronounced compared to the Magnus effect, resulting in the particle being drawn downwards. For higher Ste numbers, such as 0.1 and 0.5, melting occurs so rapidly that the particle nearly completes its phase change by the time the initial descent is finished, as depicted in Fig. 6-8(b).

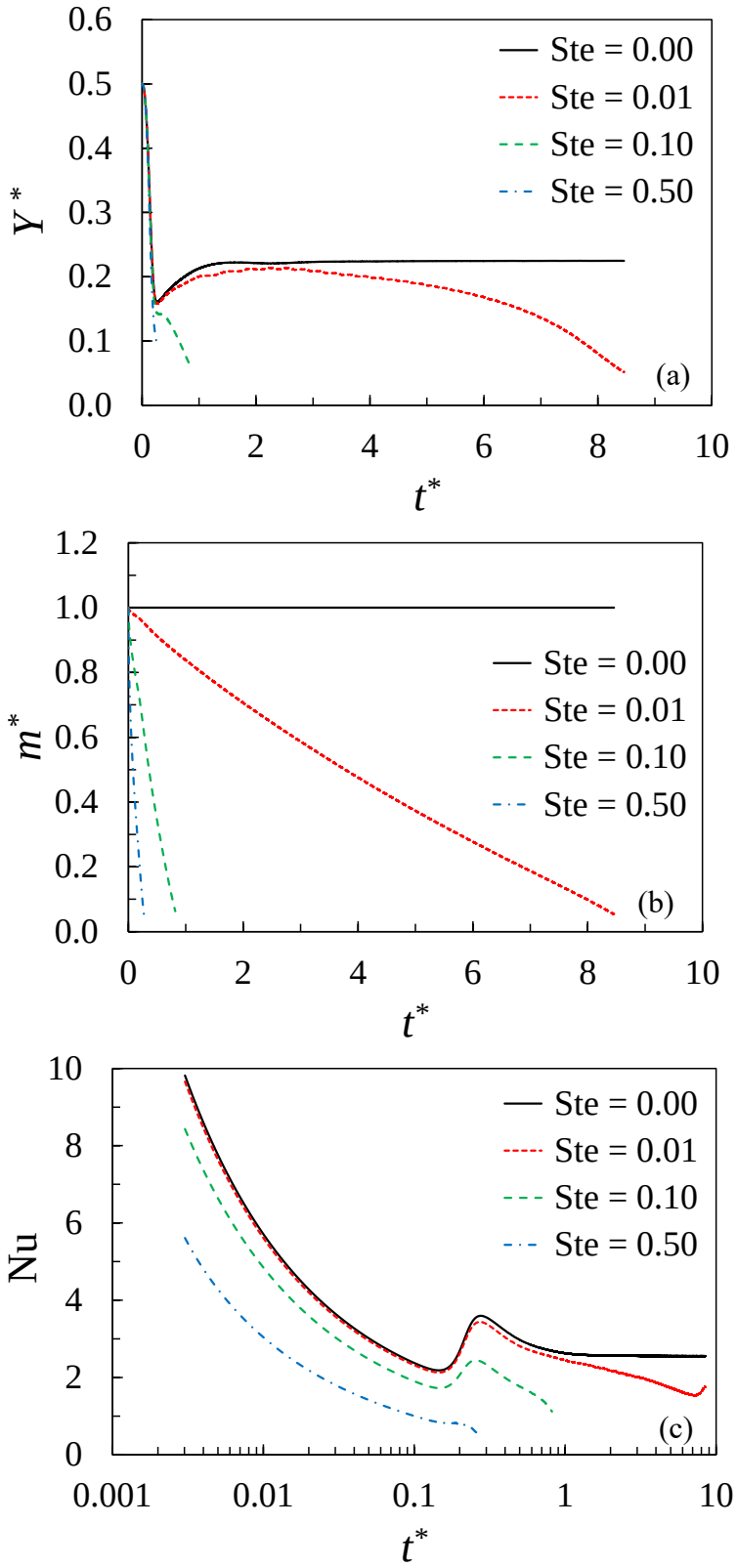

Fig. 6-8 The impact of the St number on the computationally determined transient (a) lateral position, (b) particle mass, and (c) Nu number for Re = 100, Gr = 1,000, and Y_0^* = 0.5.

Figure 6-8(c) illustrates the variations in the average Nu number at the particle surface across different Ste number values. In the case of Ste = 0, where the particle does not melt and reaches a steady state, the Nu number also stabilizes, reaching a consistent value of approximately 2.55 by $t^* \approx 1$. For Ste = 0.01, both the thermal diffusion rate and the particle surface area decrease over time due to the gradual melting of the particle. This reduction in surface area leads to a diminished heat transfer rate, resulting in a lower Nu compared to the non-melting scenario. At higher Ste numbers, Ste = 0.1 and 0.5, the melting process accelerates markedly due to the reduced latent heat requirement. This rapid phase change leads to a rapid decrease in the particle's characteristic diameter d_c, which in turn results in a smaller Nu. The fast shrinkage of the particle decreases the surface area available for heat transfer, thereby reducing the Nu number more significantly than in cases with lower Ste values, as depicted in Fig. 6-8(c).

Figure 6-9 demonstrates the effect of the initial lateral position on the transient lateral movement of the particle, under conditions of Re = 100, Ste = 0.1, and various Gr numbers. For a scenario where Gr = 0, indicating an absence of natural convection, the migration of the particle is solely influenced by drag and pressure forces. These forces result from the interactions between the pressure-driven flow and the particle's movement and rotation. This interaction not only propels the particle along the flow direction but also causes it to rotate, enhancing the Magnus force that pushes the particle toward the channel's centerline. As shown in Fig. 6-9, when $Y_0^* = 0.50$, the particle maintains its initial lateral position, indicating a balance of forces at the center of the channel. However, for particles starting from positions other than the center, the net forces direct them towards the centerline. In scenarios where natural convection is present (Gr > 0), the particle tends to move towards a unique lateral position, irrespective of its initial starting point. As

the particle melts and shifts downward toward the bottom wall, its downward velocity decreases by increasing pressure between the particle and the bottom wall, a dynamic previously discussed.

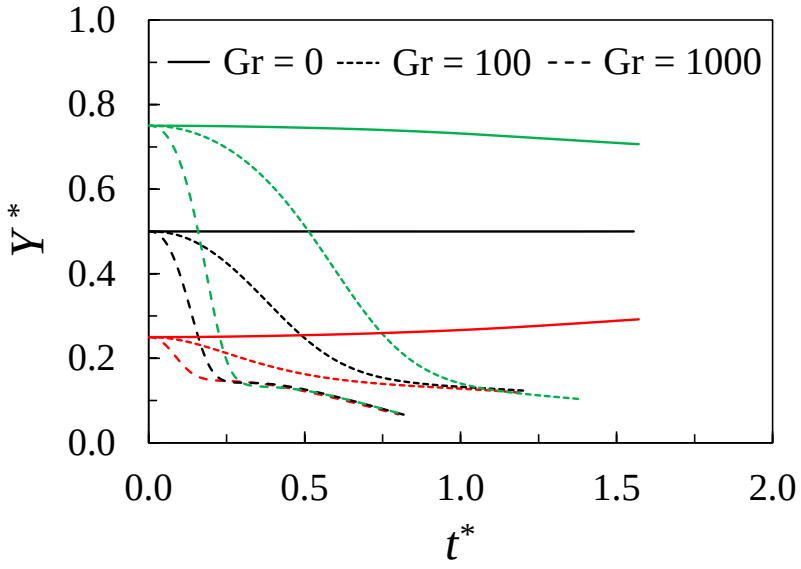

Fig. 6-9 The initial lateral position (Y_0^*) impact on the particle transient lateral movement, for Y_0^* = 0.25 (red), Y_0^* = 0.50 (black), and Y_0^* = 0.75 (green) for Re = 100, and Ste = 0.1.

6.4. Concluding Remarks

In the simulation part of this study, an ALE approach is employed to simulate the migration and heat transfer dynamics of a melting cylindrical particle in a plane Poiseuille flow between horizontal parallel plates. The model utilized a dynamic mesh technique to directly account for the local deformation of the particle due to melting and to monitor its migration without the need for implicit interface tracking schemes. An extensive parametric analysis was conducted to explore the impacts of Reynolds number, Grashof number, Stefan number, and the initial lateral position of the particle on its lateral migration, mass, and Nusselt number. The key findings from this study are summarized as follows:

- Increasing the Re number causes the melting particle to migrate further from the wall due to a stronger Magnus force. This greater distance from the heated wall leads to a decrease in both the melting rate and the Nu number.
- With a higher Gr number, the particle's migration toward the bottom wall is accelerated by the more intense downward flow driven by natural convection adjacent to the particle. Being closer to the heated wall enhances both the melting rate and Nu number.
- An increase in the Ste number significantly enhances the melting rate as a result of the diminished latent heat effect.
- For a constant Gr number, a melting particle will migrate toward the same final lateral position, regardless of its initial placement in the flow.

Generally, it is observed that higher (lower) flow velocities and reduced (increased) natural convection effects correspond to decreased (increased) melting rates. This study validates the ALE method as a robust approach for directly simulating scenarios that involve suspended particles undergoing phase changes.

Nomenclature

c	Specific heat of the liquid (J/kg·K)
D	Initial particle diameter (m)
d_c	Instantaneous characteristic particle diameter (m), $d_c = \frac{1}{\pi}\int_S dS$
$\mathbf{F}$	Force vector (N)
$\mathbf{f}$	Body force per unit mass (N/kg)
$\mathbf{F}^*$	Dimensionless force vector, $\mathbf{F}^* = \mathbf{F}/(\nu\rho Z u_{\max})$
g	Gravitational acceleration (m/s^2)
$\mathbf{g}$	Gravity vector (m/s^2)
Gr	Grashof number, $\mathrm{Gr} = \frac{g\beta D^3(T_h - T_m)}{\nu^2}$
h	Convective heat transfer coefficient (W/m^2·K)
h_{sl}	Particle heat of fusion (J/kg)
$\mathbf{I}$	Unit tensor
I	Particle moment of inertia around the center of mass (kg·m^2)
k	Thermal conductivity (W/m·K)
L	Length of the computational domain (m)
L^*	Dimensionless length of the computational domain, $L^* = \frac{L}{D}$
$\mathbf{M}$	Moment vector around the particle center of mass (N·m)

$\mathbf{M}^*$ Dimensionless moment vector, $\mathbf{M}^* = \mathbf{M}/(\nu\rho DZu_{\max})$

m Instantaneous particle mass (kg)

m_0 Initial particle mass (kg)

m^* Dimensionless particle mass, $m^* = \frac{m}{m_0}$

N Total number of control volumes

Nu Nusselt number, $\mathrm{Nu} = \frac{hd_c}{k}$

n Surface unit normal vector pointing out of the solid particle

n Time step index

p Pressure (Pa)

p^* Dimensionless pressure, $p^* = (p + \rho gy)/(\nu\rho u_{\max}/D)$

Pr Prandtl number, $\mathrm{Pr} = \frac{\nu}{\alpha}$

q'' Local heat flux at particle surface (W/m^2)

R Solid-liquid interface coordinate vector in relation to referential coordinates (m)

r Solid-liquid interface coordinate vector in relation to particle center of mass (m)

Re Channel Reynolds number, $\mathrm{Re} = \frac{u_{\max}W}{\nu}$

Re_D Particle Re number based on maximum flow velocity and initial particle diameter, $\mathrm{Re}_D = \frac{u_{\max}D}{\nu}$

S Particle surface area (m^2)

$\dot{S}_{\text{mass}}$ Volumetric mass source term (kg/m^3·s)

$\dot{S}^*$ Dimensionless mass source term, $\dot{S}^* = \frac{\dot{S}_{\text{mass}} D^2}{\mu}$

Ste Stefan number, $\text{Ste} = \frac{c(T_h - T_m)}{h_{\text{sl}}}$

T Temperature (K)

T^* Dimensionless temperature, $T^* = (T - T_m)/(T_h - T_m)$

T_h Hot wall temperature (K)

T_m Melting temperature of the particle (K)

t Time (s)

t^* Dimensionless time, $t^* = \frac{t\nu}{D^2}$

u Velocity in *x*-direction

u_{max} Maximum velocity of the fully developed undisturbed flow (m/s)

u_{slip} The slip velocity between the flow and the particle in the *x*-direction (m/s)

u^*_{slip} Dimensionless slip velocity, $u^*_{\text{slip}} = u_{\text{slip}} D/\nu$

$\mathbf{V}$ Velocity vector (m/s)

$\mathbf{V}^*$ Dimensionless velocity vector, $\mathbf{V}^* = \mathbf{V}/u_{\text{max}}$

$\mathbf{V}_{\text{frame}}$ Moving velocity vector of the reference frame (m/s)

$\mathbf{V}_{\text{mesh}}$ Mesh velocity vector (m/s)

v Velocity in *y*-direction

V_{CV} Volume of the control volume, (m^3)

W Width of the computational domain (m)

$\boldsymbol{X}$ Coordinates of a particular point

x x-coordinate (m)

x^* Dimensionless position in the x-direction, $x^* = x/D$

Y^* Dimensionless lateral position of the particle, $Y^* = y/W$

y y-coordinate (m)

y^* Dimensionless position in the y-direction, $y^* = y/D$

Z Unit depth of the particle in the direction normal to the plane

Γ Diffusion coefficient

α Thermal diffusivity of the fluid (m^2/s)

β Coefficient of thermal expansion (1/K)

μ Dynamic viscosity (kg/m·s)

ν Kinematic viscosity (m^2/s)

ρ Density (kg/m^3)

σ Stress tensor (Pa)

ϕ General scalar quantity

$\boldsymbol{\omega}$ Rotational velocity vector (1/s)

$\boldsymbol{\omega}^*$ Dimensionless rotational velocity vector, $\boldsymbol{\omega}^* = \boldsymbol{\omega} D/u_{\max}$

Subscripts

0	Initial
Eq	Equilibrium
i	Inlet
l	Liquid
o	Outlet
p	Particle
ref	Referential domain (moving with the dynamic mesh)
s	Solid

7. Future Work

In this dissertation, a freeze desalination setup is fabricated and evaluated under a variety of operational conditions. The experimental study demonstrated promising results, showing the efficacy and feasibility of a novel freeze desalination system compared to existing direct and indirect contact freezing methods. This novel setup not only simplifies the operational process but also achieves high desalination rates and maintains satisfactory recovery ratios, making it an effective solution for desalinating high-salinity brine. Despite these advantages, several aspects of the current configuration require further modifications or enhancements to optimize performance. Future improvements should focus on refining these areas to fully leverage the potential of this innovative desalination approach.

- One enhancement that could be implemented in the current study involves control over the temperature and duration of the freezing process. The study indicates that quicker crystallization correlates with higher salinity levels in the produced ice. By modulating the temperature within the freezing chamber—starting with a higher ICL temperature when the brine is first introduced, then gradually reducing this temperature—it's possible to refine the quality of the ice produced. This controlled approach helps manage the crystallization rate, potentially leading to ice with lower salinity. Additionally, regulating the duration of the freezing process could also yield benefits. By ensuring that the freezing process reaches a steady state, where the temperature of the outlet mixture is uniform across all exiting components, the consistency and efficiency of the freeze desalination process can be significantly improved.

- One of the primary challenges identified in this study is the separation process—specifically, the efficient extraction of ice from the slurry and the removal of unfrozen concentrated brine from the ICL-brine stream. Enhancements in ice-slurry separation could be achieved by utilizing the rotary solid-liquid separator equipped with a suitably sized mesh for the inner cylinder. Additionally, maintaining a sealed environment during the separation process can prevent ice from melting, which is essential for improving the ice recovery ratio. As for separating the concentrated brine from the ICL-brine stream, while the current use of dual filter separators effectively reduces the volume of concentrated brine, a small amount still manages to reach the ICL tank and subsequently the heat exchanger. Implementing a high-efficiency liquid separator could address this residual issue by ensuring a more complete and effective separation, thus avoiding brine accumulation in the heat exchanger.
- Addressing the efficiency of brine rejection from the collected ice presents another significant challenge in this study. While the current use of a centrifugal separator together with intermittent ice crushing has demonstrated remarkable desalination rates, it fails to produce potable water. To improve the efficacy of brine rejection, one promising strategy could be to implement continuous ice crushing throughout the centrifugal separation process. This approach helps because once the collected ice dries out shortly after being collected, removing any remaining brine becomes increasingly difficult. Continuously crushing the ice can help keep it in a state that more readily releases trapped brine. Additionally, another method to enhance brine rejection could involve washing the collected ice during the centrifugation process. This washing could be performed using

either cold potable water or a cold brine solution with low salinity, which would help flush out the brine entrapped in the ice.

The energy enhancement of the proposed freeze desalination setup was another objectibe of this dissertation. A notable method for enhancing the energy efficiency in the proposed system involves recovering the cold energy of the produced ice to cool the refrigeration unit's condenser. This goal can be accomplished by circulating an ice-water slurry through a heat exchanger, allowing it to absorb heat from the condensing refrigerant. To deepen the understanding of heat transfer in ice-water slurry, a computational model was developed that simulates the melting process of a solid particle suspended in its own melt. This study explores a particle melting within a two-dimensional domain under Poiseuille flow condition. The model is designed for scalability to three dimensions with minimal adjustments needed in the User-Defined Functions (UDFs) and the setup configurations in the CFD package. Transitioning to a three-dimensional framework will allow for a broader range of studies, enabling more simulations that can better mirror complex real-life applications.

- One potential study is the simulation of particle migration within circular tubes and square ducts. Previous studies have identified the phenomenon of dual equilibrium locations in the neutrally buoyant migration of particles within tube Poiseuille flow. These dual equilibrium points are influenced by several factors, including the diameters of the particle and tube, the particle's initial position, the tube's length, and the Re number. Although these phenomena have been studied numerically, most existing research has focused on determining the particle's equilibrium position by calculating the lift force on a laterally fixed positioned particle, with only a few studies addressing the transient movement of

particles. Moreover, the ALE method, which offers a more precise direct interface tracking technique, has not been applied in these studies.

- Another possible extension of the current study involves exploring the melting behavior of a spherical particle within circular tubes or square ducts. While employing the ALE method for these configurations might increase computational demands, the enhanced accuracy provided by this approach could significantly outweigh these challenges.

8. References

[1] K. Elsaid, M. Kamil, E.T. Sayed, M.A. Abdelkareem, T. Wilberforce, A. Olabi, Environmental impact of desalination technologies: A review, Sci. Total Environ. 748 (2020) 141528. https://doi.org/10.1016/j.scitotenv.2020.141528.

[2] V.G. Gude, N. Nirmalakhandan, Desalination at low temperatures and low pressures, Desalination. 244 (2009) 239–247. https://doi.org/10.1016/j.desal.2008.06.005.

[3] P. Gleick, R.W. Miller, The World's Water: The biennial report on freshwater resources 2002-2003, Island Press, 2003. https://doi.org/10.5070/g311810517.

[4] M.C. Mickley, Membrane Concentrate Disposal: Practices and Regulation, US Department of the Interior, Bureau of Reclamation, 2006. https://www.usbr.gov/research/dwpr/reportpdfs/report123.pdf.

[5] H. Djuma, A. Bruggeman, M. Eliades, M.A. Lange, Non-conventional water resources research in semi-arid countries of the Middle East, Desalin. Water Treat. 57 (2016) 2290–2303. https://doi.org/10.1080/19443994.2014.984930.

[6] B.D. Richter, D. Abell, E. Bacha, K. Brauman, S. Calos, A. Cohn, C. Disla, S.F. O'Brien, D. Hodges, S. Kaiser, M. Loughran, C. Mestre, M. Reardon, E. Siegfried, Tapped out: How can cities secure their water future?, Water Policy. 15 (2013) 335–363. https://doi.org/10.2166/wp.2013.105.

[7] V.G. Gude, Desalination and water reuse to address global water scarcity, Rev. Environ. Sci. Biotechnol. 16 (2017) 591–609. https://doi.org/10.1007/s11157-017-9449-7.

[8] J. Schewe, J. Heinke, D. Gerten, I. Haddeland, N.W. Arnell, D.B. Clark, R. Dankers, S. Eisner, B.M. Fekete, F.J. Colón-González, S.N. Gosling, H. Kim, X. Liu, Y. Masaki, F.T. Portmann, Y. Satoh, T. Stacke, Q. Tang, Y. Wada, D. Wisser, T. Albrecht, K. Frieler, F. Piontek, L. Warszawski, P. Kabat, Multimodel assessment of water scarcity under climate change, Proc. Natl. Acad. Sci. U. S. A. 111 (2014) 3245–3250. https://doi.org/10.1073/pnas.1222460110.

[9] F. Macedonio, E. Drioli, A.A. Gusev, A. Bardow, R. Semiat, M. Kurihara, Efficient technologies for worldwide clean water supply, Chem. Eng. Process. Process Intensif. 51 (2012) 2–17. https://doi.org/10.1016/j.cep.2011.09.011.

[10] M.M. Mekonnen, A.Y. Hoekstra, Four billion people facing severe water scarcity, Sci. Adv. 2 (2016) e1500323. https://doi.org/10.1126/sciadv.1500323.

[11] M. Qadir, Policy Note: Addressing Trade-offs to Promote Safely Managed Wastewater in Developing Countries, Water Econ. Policy. 4 (2018) 1871002. https://doi.org/10.1142/S2382624X18710029.

[12] M.T.H. Van Vliet, M. Florke, Y. Wada, Quality matters for water scarcity, Nat. Geosci. 10 (2017) 800–802. https://doi.org/10.1038/NGEO3047.

[13] E. Jones, M.T.H. van Vliet, Drought impacts on river salinity in the southern US: Implications for water scarcity, Sci. Total Environ. 644 (2018) 844–853. https://doi.org/10.1016/j.scitotenv.2018.06.373.

[14] N.C. Darre, G.S. Toor, Desalination of Water: a Review, Curr. Pollut. Reports. 4 (2018) 104–111. https://doi.org/10.1007/s40726-018-0085-9.

[15] N. Ghaffour, T.M. Missimer, G.L. Amy, Technical review and evaluation of the economics of water desalination: Current and future challenges for better water supply sustainability, Desalination. 309 (2013) 197–207. https://doi.org/10.1016/j.desal.2012.10.015.

[16] M.W. Shahzad, M. Burhan, L. Ang, K.C. Ng, Energy-water-environment nexus underpinning future desalination sustainability, Desalination. 413 (2017) 52–64. https://doi.org/10.1016/j.desal.2017.03.009.

[17] E. Jones, M. Qadir, M.T.H. van Vliet, V. Smakhtin, S. mu Kang, The state of desalination and brine production: A global outlook, Sci. Total Environ. 657 (2019) 1343–1356. https://doi.org/10.1016/j.scitotenv.2018.12.076.

[18] S. Lattemann, M.D. Kennedy, J.C. Schippers, G. Amy, Chapter 2 Global Desalination Situation, Sustain. Sci. Eng. 2 (2010) 7–39. https://doi.org/10.1016/S1871-2711(09)00202-5.

[19] S.K. Natarajan, S.K. Suraparaju, R.M. Elavarasan, A review on low-temperature thermal desalination approach, Environ. Sci. Pollut. Res. 29 (2022) 32443–32466. https://doi.org/10.1007/s11356-022-19147-5.

[20] WHO, Guidelines for Drinking-water Quality, World Heal. Organ. 1 (2008) 1–668.

[21] L.F. Greenlee, D.F. Lawler, B.D. Freeman, B. Marrot, P. Moulin, Reverse osmosis desalination: Water sources, technology, and today's challenges, Water Res. 43 (2009) 2317–2348. https://doi.org/10.1016/j.watres.2009.03.010.

[22] M. Cheryan, Ultrafiltration and Microfiltration Handbook, CRC press, 1998. https://doi.org/10.1201/9781482278743.

[23] A. Campione, L. Gurreri, M. Ciofalo, G. Micale, A. Tamburini, A. Cipollina, Electrodialysis for water desalination: A critical assessment of recent developments on process fundamentals, models and applications, Desalination. 434 (2018) 121–160. https://doi.org/10.1016/j.desal.2017.12.044.

[24] B. Van der Bruggen, C. Vandecasteele, Distillation vs. membrane filtration: Overview of process evolutions in seawater desalination, Desalination. 143 (2002) 207–218. https://doi.org/10.1016/S0011-9164(02)00259-X.

[25] I.C. Watson, O.J. Morin, L. Henthorne, Desalting Handbook for Planners, Desalin. Water Purif. Res. Dev. Progr. Rep. No. 72. (2003) 1–310. http://www.ncbi.nlm.nih.gov/pubmed/22126638.

[26] M. Qasim, M. Badrelzaman, N.N. Darwish, N.A. Darwish, N. Hilal, Reverse osmosis desalination: A state-of-the-art review, Desalination. 459 (2019) 59–104. https://doi.org/10.1016/j.desal.2019.02.008.

[27] K.P. Lee, T.C. Arnot, D. Mattia, A review of reverse osmosis membrane materials for desalination-Development to date and future potential, J. Memb. Sci. 370 (2011) 1–22. https://doi.org/10.1016/j.memsci.2010.12.036.

[28] C. Fritzmann, J. Löwenberg, T. Wintgens, T. Melin, State-of-the-art of reverse osmosis desalination, Desalination. 216 (2007) 1–76. https://doi.org/10.1016/j.desal.2006.12.009.

[29] L. Malaeb, G.M. Ayoub, Reverse osmosis technology for water treatment: State of the art review, Desalination. 267 (2011) 1–8. https://doi.org/10.1016/j.desal.2010.09.001.

[30] H. Rabiee, K.R. Khalilpour, J.M. Betts, N. Tapper, Energy-water nexus: Renewable-integrated hybridized desalination systems, Polygeneration with Polystorage Chem. Energy Hubs. (2018) 409–458. https://doi.org/10.1016/B978-0-12-813306-4.00013-6.

[31] H.C. Flemming, G. Schaule, T. Griebe, J. Schmitt, A. Tamachkiarowa, Biofouling - The Achilles heel of membrane processes, Desalination. 113 (1997) 215–225. https://doi.org/10.1016/S0011-9164(97)00132-X.

[32] M. Kamal, Optimal scheduling, design, operation and control of reverse osmosis desalination. Prediction of RO membrane performance under different design and operating conditions, synthesis of RO networks using MINLP optimization framework involving fouling, boron, University of Bradford, 2021.

[33] M. Ahmed, R. Kumar, B. Garudachari, J.P. Thomas, Performance evaluation of a thermoresponsive polyelectrolyte draw solution in a pilot scale forward osmosis seawater desalination system, Desalination. 452 (2019) 132–140. https://doi.org/10.1016/j.desal.2018.11.013.

[34] M. Amjad, J. Gardy, A. Hassanpour, D. Wen, Novel draw solution for forward osmosis based solar desalination, Appl. Energy. 230 (2018) 220–231. https://doi.org/10.1016/j.apenergy.2018.08.021.

[35] N. Abdullah, M.H. Tajuddin, N. Yusof, Forward Osmosis (FO) for Removal of Heavy Metals, Nanotechnol. Water Wastewater Treat. Theory Appl. (2019) 177–204.

https://doi.org/10.1016/B978-0-12-813902-8.00010-1.

[36] W. Tang, H.Y. Ng, Concentration of brine by forward osmosis: Performance and influence of membrane structure, Desalination. 224 (2008) 143–153. https://doi.org/10.1016/j.desal.2007.04.085.

[37] E.A. Bell, T.E. Poynor, K.B. Newhart, J. Regnery, B.D. Coday, T.Y. Cath, Produced water treatment using forward osmosis membranes: Evaluation of extended-time performance and fouling, J. Memb. Sci. 525 (2017) 77–88. https://doi.org/10.1016/j.memsci.2016.10.032.

[38] D.J. Johnson, W.A. Suwaileh, A.W. Mohammed, N. Hilal, Osmotic's potential: An overview of draw solutes for forward osmosis, Desalination. 434 (2018) 100–120. https://doi.org/10.1016/j.desal.2017.09.017.

[39] D. Zhao, S. Chen, C.X. Guo, Q. Zhao, X. Lu, Multi-functional forward osmosis draw solutes for seawater desalination, Chinese J. Chem. Eng. 24 (2016) 23–30. https://doi.org/10.1016/j.cjche.2015.06.018.

[40] A. Panagopoulos, K.J. Haralambous, M. Loizidou, Desalination brine disposal methods and treatment technologies - A review, Sci. Total Environ. 693 (2019) 133545. https://doi.org/10.1016/j.scitotenv.2019.07.351.

[41] P.G. Youssef, R.K. Al-Dadah, S.M. Mahmoud, Comparative analysis of desalination technologies, Energy Procedia. 61 (2014) 2604–2607. https://doi.org/10.1016/j.egypro.2014.12.258.

[42] H.T. El-Dessouky, H.M. Ettouney, Fundamentals of Salt Water Desalination, Elsevier, 2002. https://doi.org/10.1016/b978-0-444-50810-2.x5000-3.

[43] H. Ettouney, Conventional Thermal Process, Seawater Desalin. Conv. Renew. Energy Process. (2009) 306. https://doi.org/10.1007/978-3-642-01150-4.

[44] I.M. Mujtaba, M.T. Sowgath, Desalination Technologies: Design and Operation, Elsevier, 2022. https://doi.org/10.1016/C2016-0-05222-1.

[45] O.K. Buros, The ABCs of Desalting, International Desalination Association Topsfield, MA, 2000. http://www.water.ca.gov/pubs/surfacewater/abcs_of_desalting/abcs_of_desalting.pdf.

[46] A. Al-Karaghouli, L.L. Kazmerski, Energy consumption and water production cost of conventional and renewable-energy-powered desalination processes, Renew. Sustain. Energy Rev. 24 (2013) 343–356. https://doi.org/10.1016/j.rser.2012.12.064.

[47] X. Wang, A. Christ, K. Regenauer-Lieb, K. Hooman, H.T. Chua, Low grade heat driven multi-effect distillation technology, Int. J. Heat Mass Transf. 54 (2011) 5497–5503. https://doi.org/doi.org/10.1016/j.ijheatmasstransfer.2011.07.041.

[48] H. Sharon, K.S. Reddy, A review of solar energy driven desalination technologies, Renew. Sustain. Energy Rev. 41 (2015) 1080–1118. https://doi.org/10.1016/j.rser.2014.09.002.

[49] A. Cipollina, G. Micale, L. Rizzuti, A critical assessment of desalination operations in Sicily, Desalination. 182 (2005) 1–12. https://doi.org/10.1016/j.desal.2005.03.004.

[50] I. Ullah, M.G. Rasul, Recent developments in solar thermal desalination technologies: A review, Energies. 12 (2019). https://doi.org/10.3390/en12010119.

[51] C. Sommariva, V.S.N. Syambabu, Increase in water production in UAE, Desalination. 138 (2001) 173–179. https://doi.org/10.1016/S0011-9164(01)00261-2.

[52] T. Mezher, H. Fath, Z. Abbas, A. Khaled, Techno-economic assessment and environmental impacts of desalination technologies, Desalination. 266 (2011) 263–273. https://doi.org/10.1016/j.desal.2010.08.035.

[53] G. Cipolletta, N. Lancioni, Ç. Akyol, A.L. Eusebi, F. Fatone, Brine treatment technologies towards minimum/zero liquid discharge and resource recovery: State of the art and techno-economic assessment, J. Environ. Manage. 300 (2021). https://doi.org/10.1016/j.jenvman.2021.113681.

[54] G.A. Tsalidis, J.J.E. Gallart, J.B. Corberá, F.C. Blanco, S. Harris, G. Korevaar, Social life cycle assessment of brine treatment and recovery technology: A social hotspot and site-specific evaluation, Sustain. Prod. Consum. 22 (2020) 77–87. https://doi.org/10.1016/j.spc.2020.02.003.

[55] A. Panagopoulos, K.J. Haralambous, Minimal Liquid Discharge (MLD) and Zero Liquid Discharge (ZLD) strategies for wastewater management and resource recovery-Analysis, challenges and prospects, J. Environ. Chem. Eng. 8 (2020) 104418. https://doi.org/10.1016/j.jece.2020.104418.

[56] Michael Mickley, Updated and extended survey of US municipal desalination plants, Desalination and Water Purification Research and Development Program Report No. 207,

Desalin. Water Purif. Res. Dev. Progr. Rep. 27 (2018).

[57] A. Giwa, V. Dufour, F. Al Marzooqi, M. Al Kaabi, S.W. Hasan, Brine management methods: Recent innovations and current status, Desalination. 407 (2017) 1–23. https://doi.org/10.1016/j.desal.2016.12.008.

[58] D. Zhao, L.Y. Lee, S.L. Ong, P. Chowdhury, K.B. Siah, H.Y. Ng, Electrodialysis reversal for industrial reverse osmosis brine treatment, Sep. Purif. Technol. 213 (2019) 339–347. https://doi.org/10.1016/j.seppur.2018.12.056.

[59] F. Mansour, S.Y. Alnouri, M. Al-Hindi, F. Azizi, P. Linke, Screening and cost assessment strategies for end-of-Pipe Zero Liquid Discharge systems, J. Clean. Prod. 179 (2018) 460–477. https://doi.org/10.1016/j.jclepro.2018.01.064.

[60] T. Tong, M. Elimelech, The Global Rise of Zero Liquid Discharge for Wastewater Management: Drivers, Technologies, and Future Directions, Environ. Sci. Technol. 50 (2016) 6846–6855. https://doi.org/10.1021/acs.est.6b01000.

[61] G.U. Semblante, J.Z. Lee, L.Y. Lee, S.L. Ong, H.Y. Ng, Brine pre-treatment technologies for zero liquid discharge systems, Desalination. 441 (2018) 96–111. https://doi.org/10.1016/j.desal.2018.04.006.

[62] S. Eslamian, Urban Water Reuse, Taylor & Francis Group, 2016.

[63] T. Younos, Environmental Issues of Desalination, J. Contemp. Water Res. Educ. 132 (2009) 11–18. https://doi.org/10.1111/j.1936-704x.2005.mp132001003.x.

[64] J.R. Ziolkowska, Is Desalination Affordable?—Regional Cost and Price Analysis, Water

Resour. Manag. 29 (2015) 1385–1397. https://doi.org/10.1007/s11269-014-0901-y.

[65] H. Arafat, Desalination sustainability: a technical, socioeconomic, and environmental approach, Elsevier, 2017.

[66] S. Lattemann, T. Höpner, Environmental impact and impact assessment of seawater desalination, Desalination. 220 (2008) 1–15. https://doi.org/10.1016/j.desal.2007.03.009.

[67] J.R. Ziolkowska, R. Reyes, Prospects for Desalination in the United States-Experiences From California, Florida, and Texas, in: Compet. Water Resour. Exp. Manag. Approaches US Eur., Elsevier, 2017: pp. 298–316. https://doi.org/10.1016/B978-0-12-803237-4.00017-3.

[68] J.S. Chang, Understanding the role of ecological indicator use in assessing the effects of desalination plants, Desalination. 365 (2015) 416–433. https://doi.org/10.1016/j.desal.2015.03.013.

[69] A. Valipour, N. Hamnabard, K.S. Woo, Y.H. Ahn, Performance of high-rate constructed phytoremediation process with attached growth for domestic wastewater treatment: Effect of high TDS and Cu, J. Environ. Manage. 145 (2014) 1–8. https://doi.org/10.1016/j.jenvman.2014.06.009.

[70] D.C. Thomas, S.M. Benson, Carbon dioxide capture for storage in deep geologic formations-results from the CO2 Capture Project: Vol 2-Geologic Storage of Carbon Dioxide with Monitoring and Verification, Elsevier, 2015.

[71] R.G. Maliva, T.M. Missimer, R. Fontaine, Injection Well Options for Sustainable

Disposal of Desalination Concentrate, IDA J. Desalin. Water Reuse. 3 (2011) 17–23. https://doi.org/10.1179/ida.2011.3.3.17.

[72] J.B. Gálvez, S.M. Rodríguez, E. Delyannis, V.G. Belessiotis, S.C. Bhattacharya, S. Kumar, Solar Energy Conversion and Photoenergy Systems: Thermal Systems and Desalination Plants, EOLSS Publications, 2010.

[73] P.M.G. Olabarria, Constructive Engineering of Large Reverse Osmosis Desalination Plants, Chemical Publishing Company, Chemical Publishing Company, 2015.

[74] R. Bergman, Reverse osmosis and nanofiltration, American Water Works Association, 2007.

[75] S.M. Badawy, Laboratory freezing desalination of seawater, Desalin. Water Treat. 57 (2016) 11040–11047. https://doi.org/10.1080/19443994.2015.1041163.

[76] M.S. Rahman, M. Ahmed, X.D. Chen, Freezing-melting process and desalination: I. review of the state-of-the-art, Sep. Purif. Rev. 35 (2006) 59–96. https://doi.org/10.1080/15422110600671734.

[77] A. Brunetti, F. Macedonio, G. Barbieri, E. Drioli, Membrane engineering for environmental protection and sustainable industrial growth: Options for water and gas treatment, Environ. Eng. Res. 20 (2015) 307–328. https://doi.org/10.4491/eer.2015.074.

[78] P.M. Williams, M. Ahmad, B.S. Connolly, Freeze desalination: An assessment of an ice maker machine for desalting brines, Desalination. 308 (2013) 219–224. https://doi.org/10.1016/j.desal.2012.07.037.

[79] K. El Kadi, I. Janajreh, Desalination by Freeze Crystallization: An Overview, Int. J. Therm. Environ. Eng. 15 (2019) 103–110. https://doi.org/10.5383/ijtee.15.02.004.

[80] D.G. Randall, J. Nathoo, A succinct review of the treatment of Reverse Osmosis brines using Freeze Crystallization, J. Water Process Eng. 8 (2015) 186–194. https://doi.org/10.1016/j.jwpe.2015.10.005.

[81] P.M. Williams, M. Ahmad, B.S. Connolly, D.L. Oatley-Radcliffe, Technology for freeze concentration in the desalination industry, Desalination. 356 (2015) 314–327. https://doi.org/10.1016/j.desal.2014.10.023.

[82] M.S. Rahman, M. Ahmed, X.D. Chen, Freezing-melting process and desalination: Review of present status and future prospects, Int. J. Nucl. Desalin. 2 (2007) 253–264. https://doi.org/10.1504/IJND.2007.013549.

[83] J. Kucera, Desalination: Water from Water, John Wiley & Sons, 2014. https://doi.org/10.1002/9781118904855.

[84] A.J. Barduhn, A. Manudhane, Temperatures required for eutectic freezing of natural waters, Desalination. 28 (1979) 233–241. https://doi.org/10.1016/S0011-9164(00)82232-8.

[85] L.C. Dickey, Evaporation of water from agitated freezing slurries at low pressure, Desalination. 104 (1996) 155–163. https://doi.org/10.1016/0011-9164(96)00038-0.

[86] B. Kalista, H. Shin, J. Cho, A. Jang, Current development and future prospect review of freeze desalination, Desalination. 447 (2018) 167–181.

https://doi.org/10.1016/j.desal.2018.09.009.

[87] C. Xie, L. Zhang, Y. Liu, Q. Lv, G. Ruan, S.S. Hosseini, A direct contact type ice generator for seawater freezing desalination using LNG cold energy, Desalination. 435 (2018) 293–300. https://doi.org/10.1016/j.desal.2017.04.002.

[88] H. Yuan, P. Sun, J. Zhang, K. Sun, N. Mei, P. Zhou, Theoretical and experimental investigation of an absorption refrigeration and pre-desalination system for marine engine exhaust gas heat recovery, Appl. Therm. Eng. 150 (2019) 224–236. https://doi.org/10.1016/j.applthermaleng.2018.12.153.

[89] J. Chang, J. Zuo, K.J. Lu, T.S. Chung, Freeze desalination of seawater using LNG cold energy, Water Res. 102 (2016) 282–293. https://doi.org/10.1016/j.watres.2016.06.046.

[90] I. Janajreh, H. Zhang, K. El Kadi, N. Ghaffour, Freeze desalination: Current research development and future prospects, Water Res. 229 (2023) 119389. https://doi.org/10.1016/j.watres.2022.119389.

[91] S. Hirakawa, K. Kosugi, Utilization of LNG cold, Int. J. Refrig. 4 (1981) 17–21. https://doi.org/10.1016/0140-7007(81)90076-1.

[92] A.J. Barduhn, The freezing process for water conversion in the United States, 1968.

[93] G.L. Stepakoff, A.P. Modica, The hydrolysis of halocarbon refrigerants in freeze desalination processes Part 1. Solubility and hydrolysis rates of Freon 114 (CClF2CClF2), Desalination. 12 (1973) 85–105. https://doi.org/10.1016/S0011-9164(00)80177-0.

[94] P. Wang, T.S. Chung, A conceptual demonstration of freeze desalination-membrane

distillation (FD-MD) hybrid desalination process utilizing liquefied natural gas (LNG) cold energy, Water Res. 46 (2012) 4037–4052. https://doi.org/10.1016/j.watres.2012.04.042.

[95] W. Lin, M. Huang, A. Gu, A seawater freeze desalination prototype system utilizing LNG cold energy, Int. J. Hydrogen Energy. 42 (2017) 18691–18698. https://doi.org/10.1016/j.ijhydene.2017.04.176.

[96] K.R. Morison, R.W. Hartel, Evaporation and freeze concentration, in: Handb. Food Eng. Second Ed., CRC Press, 2006: pp. 495–552. https://doi.org/10.1201/9780429449734-9.

[97] H.F. Wiegandt, A. Madani, P. Harriott, Ice crystallization developments for the butane direct-contact process, Desalination. 67 (1987) 107–126. https://doi.org/10.1016/0011-9164(87)90237-2.

[98] A.J. Barduhn, The state of the crystallization processes for desalting saline waters, Desalination. 5 (1968) 173–184. https://doi.org/10.1016/S0011-9164(00)80212-X.

[99] H. Thijssen, Current developments in freeze concentration of liquid foods, Free. Dry. Adv. Food Technol. (1975) 481–501.

[100] Josef Shwartz, Ronald F. Probstein, Experimental Study of Slurry Separators for Use in Desalination, M, I.T.-Dept Mech Eng-Fluid Mech. Lab. Publ 69-1. 6 (1969) 239–266. https://doi.org/10.1016/0011-9164(69)80007-X.

[101] G.T. Arulampalam, C. Bates, L.F. Khaw, L. McGrath, Investigation of purification mechanism in a column crystalliser operating under total reflux and continuous

conditions, Desalination. 36 (1981) 87–97. https://doi.org/10.1016/S0011-9164(00)88633-6.

[102] S.S. Deshpande, M. Cheryan, S.K. Sathe, D.K. Salunkhe, Freeze concentration of fruit juices, C R C Crit. Rev. Food Sci. Nutr. 20 (1984) 173–248. https://doi.org/10.1080/10408398409527389.

[103] A. Najim, A review of advances in freeze desalination and future prospects, Npj Clean Water. 5 (2022). https://doi.org/10.1038/s41545-022-00158-1.

[104] S. Moharramzadeh, S.K. Ong, J. Alleman, K.S. Cetin, Parametric study of the progressive freeze concentration for desalination, Desalination. 510 (2021) 115077. https://doi.org/10.1016/j.desal.2021.115077.

[105] E.T. Igunnu, G.Z. Chen, Produced water treatment technologies, Int. J. Low-Carbon Technol. 9 (2014) 157–177. https://doi.org/10.1093/ijlct/cts049.

[106] Z. Ding, F.G.F. Qin, J. Yuan, S. Huang, R. Jiang, Y. Shao, Concentration of apple juice with an intelligent freeze concentrator, J. Food Eng. 256 (2019) 61–72. https://doi.org/10.1016/j.jfoodeng.2019.03.018.

[107] S. Samsuri, N.A. Amran, M. Jusoh, Spiral finned crystallizer for progressive freezeconcentration process, Chem. Eng. Res. Des. 104 (2015) 280–286. https://doi.org/10.1016/j.cherd.2015.06.040.

[108] H. Jaster, G.D. Arend, K. Rezzadori, V.C. Chaves, F.H. Reginatto, J.C.C. Petrus, Enhancement of antioxidant activity and physicochemical properties of yogurt enriched

with concentrated strawberry pulp obtained by block freeze concentration, Food Res. Int. 104 (2018) 119–125. https://doi.org/10.1016/j.foodres.2017.10.006.

[109] D. Weber, J. Hubbuch, Raman spectroscopy as a process analytical technology to investigate biopharmaceutical freeze concentration processes, Biotechnol. Bioeng. 118 (2021) 4708–4719. https://doi.org/10.1002/bit.27936.

[110] S. Samsuri, N.A.N. Rizan, S.H. Hung, N.A. Amran, N.S. Sambudi, Progressive Freeze Concentration for Volume Reduction of Produced Water and Biodiesel Wastewater, Chem. Eng. Technol. 42 (2019) 1764–1770. https://doi.org/10.1002/ceat.201800505.

[111] K.S. Spiegler, A.D.K. Laird, eds., Principles of Desalination, Elsevier, 1966. https://doi.org/10.1016/b978-0-12-395660-6.x5001-0.

[112] I. Janajreh, H. Zhang, K. El Kadi, N. Ghaffour, Freeze desalination : Current research development and future prospects, Water Res. 229 (2023) 119389. https://doi.org/10.1016/j.watres.2022.119389.

[113] C.W. Ong, C.L. Chen, Technical and economic evaluation of seawater freezing desalination using liquefied natural gas, Energy. 181 (2019) 429–439. https://doi.org/10.1016/j.energy.2019.05.193.

[114] Y. Liu, T. Ming, Y. Wu, R. de Richter, Y. Fang, N. Zhou, Desalination of seawater by spray freezing in a natural draft tower, Desalination. 496 (2020) 114700. https://doi.org/10.1016/j.desal.2020.114700.

[115] H. Jayakody, R. Al-Dadah, S. Mahmoud, Numerical investigation of indirect freeze

desalination using an ice maker machine, Energy Convers. Manag. 168 (2018) 407–420. https://doi.org/10.1016/j.enconman.2018.05.010.

[116] A. Eghtesad, M. Salakhi, H. Afshin, S.K. Hannani, Numerical investigation and optimization of indirect freeze desalination, Desalination. 481 (2020) 114378. https://doi.org/10.1016/j.desal.2020.114378.

[117] P. Sahu, S. Krishnaswamy, N.K. Pande, Process intensification using a novel continuous U-shaped crystallizer for freeze desalination, Chem. Eng. Process. - Process Intensif. 153 (2020) 107970. https://doi.org/10.1016/j.cep.2020.107970.

[118] D. Chen, C. Zhang, H. Rong, C. Wei, S. Gou, Experimental study on seawater desalination through supercooled water dynamic ice making, Desalination. 476 (2020) 114233. https://doi.org/10.1016/j.desal.2019.114233.

[119] A. Elhefny, H. Shabgard, J. Cai, R. Kaviani, R.N. Parthasarathy, Thermochemical modeling and performance evaluation of freeze desalination systems, Desalination. (2024) 117423.

[120] L. Erlbeck, D. Wössner, K. Schlachter, T. Kunz, F.J. Methner, M. Rädle, Investigation of a novel scraped surface crystallizer with included ice-pressing section as new purification technology, Sep. Purif. Technol. 228 (2019) 115748. https://doi.org/10.1016/j.seppur.2019.115748.

[121] L. Erlbeck, M. Rädle, R. Nessel, F. Illner, W. Müller, K. Rudolph, T. Kunz, F.J. Methner, Investigation of the depletion of ions through freeze desalination, Desalination. 407 (2017) 93–102. https://doi.org/10.1016/j.desal.2016.12.009.

[122] Y. Mandri, A. Rich, D. Mangin, S. Abderafi, C. Bebon, N. Semlali, J.P. Klein, T. Bounahmidi, A. Bouhaouss, Parametric study of the sweating step in the seawater desalination process by indirect freezing, Desalination. 269 (2011) 142–147. https://doi.org/10.1016/j.desal.2010.10.053.

[123] H. Yang, M. Fu, Z. Zhan, R. Wang, Y. Jiang, Study on combined freezing-based desalination processes with microwave treatment, Desalination. 475 (2020) 114201. https://doi.org/10.1016/j.desal.2019.114201.

[124] M. Hasan, N. Rotich, M. John, M. Louhi-Kultanen, Salt recovery from wastewater by air-cooled eutectic freeze crystallization, Chem. Eng. J. 326 (2017) 192–200. https://doi.org/10.1016/j.cej.2017.05.136.

[125] A. Alkhalidi, S. Kiwan, A. Al-Hayajneh, Experimental investigation of water desalination using freezing technology, Case Stud. Therm. Eng. 28 (2021) 101685. https://doi.org/10.1016/j.csite.2021.101685.

[126] M. Landau, A. Martindale, Assessment of crystalliser designs for a butane freeze desalination process, Desalination. 3 (1967) 318–329. https://doi.org/10.1016/S0011-9164(00)80161-7.

[127] W. Gibson, D. Emmermann, G. Grossman, R. Johnson, A. Modica, A. Pallone, Spray freezer and pressurized counterwasher for freeze desalination, Desalination. 14 (1974) 249–262. https://doi.org/10.1016/S0011-9164(00)80258-1.

[128] Heat Transfer Applications using 3M ™ Novec ™ Engineered Fluids, 2013. https://multimedia.3m.com/mws/media/1091997O/3m-novec-engineered-fluids-for-heat-

transfer-line-card.pdf.

[129] Silmid, (2023) https://www.silmid.com/us/specialties/specialty-ch.

[130] M.S. Rahman, M. Al-Khusaibi, Freezing-Melting Desalination Process, in: Wiley Blackwell 6, 2014: pp. 473–501. https://doi.org/10.1002/9781118904855.ch10.

[131] PSF - 1.5 cSt silicone heat transfer fluid product information, 2023. https://doi.org/https://www.clearcoproducts.com/pdf/volatile/NP-PSF-1_5cSt.pdf.

[132] Gelest, (2023) https://www.gelest.com/product/DMS-T01.5/.

[133] R. Kaviani, H. Shabgard, An experimental study on a novel direct contact freeze-desalination unit, in: ASTFE Digit. Libr., 2023.

[134] R. Kaviani, H. Shabgard, A. Elhefny, J. Cai, R. Parthasarathy, Experimental and theoretical study of a novel freeze desalination system with an intermediate cooling liquid, Desalination. 576 (2024) 117381. https://doi.org/10.1016/j.desal.2024.117381.

[135] P. Gorbounov, M. Battistin, E. Thomas, Comparison of liquid coolants suitable for single-phase detector cooling, (2016) 1–17.

[136] Copeland, Copelametic ® Two-Stage Compressors Application and Service Instructions, (2010) 1–11.

[137] Westermeyer Industries Inc., Product Catalog: Components for the refrigeration and air conditioning industry, (2018) 114.

[138] H. Shabgard, R. Parthasarathy, J. Cai, R. Kaviani, A. Elhefny, Apparatus and method for

continuous separation of solid particles from solid-liquid slurries, (2022). https://patents.google.com/patent/US20220371918A1/en.

[139] B. Verbeek, Eutectic Freeze Crystallization on Sodium Chloride: Analysis of a full experimental cycle, Technical University of Delf, 2011. http://resolver.tudelft.nl/uuid:2d3bca49-1f4f-41f1-a2aa-b821712d82ec.

[140] F.E. Genceli, Scaling-Up Eutectic Freeze Crystallization, Technical University of Delf, 2008. http://resolver.tudelft.nl/uuid:c64d84d8-6552-4d3c-9c02-1d511c689c43.

[141] M.M. Conde, M. Rovere, P. Gallo, Molecular dynamics simulations of freezing-point depression of TIP4P/2005 water in solution with NaCl, J. Mol. Liq. 261 (2018) 513–519. https://doi.org/10.1016/j.molliq.2018.03.126.

[142] H. Kumano, T. Asaoka, A. Saito, S. Okawa, Formulation of the latent heat of fusion of ice in aqueous solution, Int. J. Refrig. 32 (2009) 175–182. https://doi.org/10.1016/j.ijrefrig.2008.07.010.

[143] H. Zhang, I. Janajreh, M.I. Hassan Ali, K. Askar, Freezing desalination: Heat and mass validated modeling and experimental parametric analyses, Case Stud. Therm. Eng. 26 (2021) 101189. https://doi.org/10.1016/j.csite.2021.101189.

[144] A. Zambrano, Y. Ruiz, E. Hernández, M. Raventós, F.L. Moreno, Freeze desalination by the integration of falling film and block freeze-concentration techniques, Desalination. 436 (2018) 56–62. https://doi.org/10.1016/j.desal.2018.02.015.

[145] C.S. Luo, W.W. Chen, W.F. Han, Experimental study on factors affecting the quality of

ice crystal during the freezing concentration for the brackish water, Desalination. 260 (2010) 231–238. https://doi.org/10.1016/j.desal.2010.04.018.

[146] H.M. Abdelmoaty, A.U. Mahgoub, A.W. Abdeldayem, Performance analysis of salt reduction levels in indirect freeze desalination system with and without magnetic field exposure, Desalination. 508 (2021) 115021. https://doi.org/10.1016/j.desal.2021.115021.

[147] F. Dierich, P.A. Nikrityuk, S. Ananiev, 2D modeling of moving particles with phase-change effect, Chem. Eng. Sci. 66 (2011) 5459–5473. https://doi.org/10.1016/j.ces.2011.06.075.

[148] W. Guo, Y. Zhang, Z. Meng, P. Zhang, S. Poncet, Non-uniform melting of a spherical ice particle in free ascending, Int. J. Heat Mass Transf. 148 (2020). https://doi.org/10.1016/j.ijheatmasstransfer.2019.119097.

[149] K. Suzuki, T. Kawasaki, T. Asaoka, M. Yoshino, Numerical simulations of solid–liquid and solid–solid interactions in ice slurry flows by the thermal immersed boundary–lattice Boltzmann method, Int. J. Heat Mass Transf. 157 (2020) 119944. https://doi.org/10.1016/j.ijheatmasstransfer.2020.119944.

[150] K. Suzuki, T. Kuroiwa, T. Asaoka, M. Yoshino, Particle-resolved simulations of ice slurry flows in a square duct by the thermal immersed boundary–lattice Boltzmann method, Comput. Fluids. 228 (2021) 105064. https://doi.org/10.1016/j.compfluid.2021.105064.

[151] I. Sarbu, A. Dorca, Review on heat transfer analysis in thermal energy storage using latent heat storage systems and phase change materials, Int. J. Energy Res. 43 (2019) 29–64. https://doi.org/10.1002/er.4196.

[152] P.K.S. Rathore, S.K. Shukla, Potential of macroencapsulated pcm for thermal energy storage in buildings: A comprehensive review, Constr. Build. Mater. 225 (2019) 723–744. https://doi.org/10.1016/j.conbuildmat.2019.07.221.

[153] H.M. Ali, Recent advancements in PV cooling and efficiency enhancement integrating phase change materials based systems – A comprehensive review, Sol. Energy. 197 (2020) 163–198. https://doi.org/10.1016/j.solener.2019.11.075.

[154] J. Luo, D. Zou, Y. Wang, S. Wang, L. Huang, Battery thermal management systems (BTMs) based on phase change material (PCM): A comprehensive review, Chem. Eng. J. 430 (2022) 132741. https://doi.org/10.1016/j.cej.2021.132741.

[155] J.J. Zhang, C.H. Yang, Z.G. Jin, S.X. Ma, J.S. Zhang, X.M. Pang, Experimental study of jet impingement heat transfer with microencapsulated phase change material slurry, Appl. Therm. Eng. 188 (2021). https://doi.org/10.1016/j.applthermaleng.2021.116588.

[156] C.J. Ho, S.T. Hsu, T.F. Yang, B.L. Chen, S. Rashidi, W.M. Yan, Cooling performance of mini-channel heat sink with water-based nano-PCM emulsion-An experimental study, Int. J. Therm. Sci. 164 (2021). https://doi.org/10.1016/j.ijthermalsci.2021.106903.

[157] R. Pakrouh, M.J. Hosseini, R. Bahrampoury, A.A. Ranjbar, S.M. Borhani, Cylindrical battery thermal management based on microencapsulated phase change slurry, J. Energy Storage. 40 (2021) 102602. https://doi.org/10.1016/j.est.2021.102602.

[158] A. Chananipoor, Z. Azizi, B. Raei, N. Tahmasebi, Optimization of the thermal performance of nano-encapsulated phase change material slurry in double pipe heat exchanger: Design of experiments using response surface methodology (RSM), J. Build.

Eng. 34 (2021) 101929. https://doi.org/10.1016/j.jobe.2020.101929.

[159] Z. Wang, J. Qu, R. Zhang, X. Han, J. Wu, Photo-thermal performance evaluation on MWCNTs-dispersed microencapsulated PCM slurries for direct absorption solar collectors, J. Energy Storage. 26 (2019) 100793. https://doi.org/10.1016/j.est.2019.100793.

[160] Q. Lin, S. Wang, Z. Ma, J. Wang, T. Zhang, Simulation of the Melting Process of Ice Slurry for Energy Storage Using a Two-Fluid Lattice Boltzmann Method, Energy Procedia. 121 (2017) 110–117. https://doi.org/10.1016/j.egypro.2017.08.007.

[161] A. Kumar, S. Roy, Heat transfer characteristics during melting of a metal spherical particle in its own liquid, Int. J. Therm. Sci. 49 (2010) 397–408. https://doi.org/10.1016/j.ijthermalsci.2009.07.011.

[162] H. Gan, J.J. Feng, H.H. Hu, Simulation of the sedimentation of melting solid particles, Int. J. Multiph. Flow. 29 (2003) 751–769. https://doi.org/10.1016/S0301-9322(03)00035-1.

[163] H. Shabgard, H. Hu, P.A. Boettcher, M. McCarthy, Y. Sun, Heat transfer analysis of PCM slurry flow between parallel plates, Int. J. Heat Mass Transf. 99 (2016) 895–903. https://doi.org/10.1016/j.ijheatmasstransfer.2016.04.020.

[164] R. Kaviani, M. Naghashnejad, H. Shabgard, Lateral Migration of a Melting Particle in a Vertical Poiseuille Flow, in: Proc. Therm. Fluids Eng. Summer Conf., 7th Thermal and Fluids Engineering Conference (TFEC), 2022: pp. 691–699. https://doi.org/10.1615/tfec2022.mpp.040972.

[165] A. Prosperetti, G. Tryggvason, Computational methods for multiphase flow, Cambridge university press, 2007. https://doi.org/10.1017/CBO9780511607486.

[166] C.W. Hirt, B.D. Nichols, Volume of fluid (VOF) method for the dynamics of free boundaries, J. Comput. Phys. 39 (1981) 201–225. https://doi.org/10.1016/0021-9991(81)90145-5.

[167] S. Osher, R. Fedkiw,, K. Piechor, Level Set Methods and Dynamic Implicit Surfaces, Appl. Mech. Rev. 57 (2004) B15–B15. https://doi.org/10.1115/1.1760520.

[168] J. Donea, A. Huerta, J. -Ph. Ponthot, A. Rodríguez-Ferran, Arbitrary Lagrangian– Eulerian Methods, in: Encycl. Comput. Mech., 1st ed., Wiley, 2004: pp. 413–437. https://doi.org/10.1002/0470091355.ecm009.

[169] ANSYS Fluent Theory Guide, ANSYS Inc., USA. 15317 (2013) 814. http://www.afs.enea.it/project/neptunius/docs/fluent/html/th/main_pre.htm.

[170] R. Kaviani, M. Naghashnejad, H. Shabgard, Migration and heat transfer modeling of a neutrally buoyant melting particle in Poiseuille flow, Phys. Fluids. 35 (2023). https://doi.org/10.1063/5.0145904.

[171] H.H. Hu, N.A. Patankar, M.Y. Zhu, Direct Numerical Simulations of Fluid-Solid Systems Using the Arbitrary Lagrangian-Eulerian Technique, J. Comput. Phys. 169 (2001) 427–462. https://doi.org/10.1006/jcph.2000.6592.

[172] L. Li, S.J. Sherwin, P.W. Bearman, A moving frame of reference algorithm for fluid/structure interaction of rotating and translating bodies, Int. J. Numer. Methods

Fluids. 38 (2002) 187–206. https://doi.org/10.1002/fld.216.

[173] A. Faghri, Y. Zhang, Transport Phenomena in Multiphase Systems, 1st ed., Elsevier, 2006.

[174] S. V. Patankar, Numerical heat transfer and fluid flow., 1st ed., CRC Press, 1980. https://doi.org/10.13182/nse81-a20112.

[175] J.H. Ferziger, M. Perić, R.L. Street, Computational Methods for Fluid Dynamics, 4th ed., Springer Berlin Heidelberg, 2019. https://doi.org/10.1007/978-3-319-99693-6.

[176] H. Gan, J. Chang, J.J. Feng, H.H. Hu, Direct numerical simulation of the sedimentation of solid particles with thermal convection, J. Fluid Mech. 481 (2003) 385–411. https://doi.org/10.1017/S0022112003003938.

[177] J. Hu, Z. Guo, A numerical study on the migration of a neutrally buoyant particle in a Poiseuille flow with thermal convection, Int. J. Heat Mass Transf. 108 (2017) 2158–2168. https://doi.org/10.1016/j.ijheatmasstransfer.2017.01.077.

[178] W. Liu, C.Y. Wu, Inertial migration of a neutrally buoyant circular particle in a planar Poiseuille flow with thermal fluids, Phys. Fluids. 33 (2021). https://doi.org/10.1063/5.0051024.

[179] Z. Yu, X. Shao, A. Wachs, A fictitious domain method for particulate flows with heat transfer, J. Comput. Phys. 217 (2006) 424–452. https://doi.org/10.1016/j.jcp.2006.01.016.

[180] Z.G. Feng, E.E. Michaelides, Heat transfer in particulate flows with Direct Numerical Simulation (DNS), Int. J. Heat Mass Transf. 52 (2009) 777–786.

https://doi.org/10.1016/j.ijheatmasstransfer.2008.07.023.

[181] S.K. Kang, Y.A. Hassan, A direct-forcing immersed boundary method for the thermal lattice Boltzmann method, Comput. Fluids. 49 (2011) 36–45. https://doi.org/10.1016/j.compfluid.2011.04.016.

[182] B. Yang, S. Chen, C. Cao, Z. Liu, C. Zheng, Lattice Boltzmann simulation of two cold particles settling in Newtonian fluid with thermal convection, Int. J. Heat Mass Transf. 93 (2016) 477–490. https://doi.org/10.1016/j.ijheatmasstransfer.2015.10.030.

[183] D.R. Oliver, Influence of particle rotation on radial migration in the Poiseuille flow of suspensions, Nature. 194 (1962) 1269–1271. https://doi.org/10.1038/1941269b0.